NORTHWESTERN UNIVERSITY

# The Nature of the Excimer and Exciton States in Self-Assembled Organic Chromophore Systems

A DISSERTATION

SUBMITTED TO THE GRADUATE SCHOOL

IN PARTIAL FULFILLMENT OF THE REQUIREMENTS

for the degree

DOCTOR OF PHILOSOPHY

Field of Chemistry

By

Michele Soon Myong

EVANSTON, ILLINOIS

December 2021

## ABSTRACT

The Nature of the Excimer and Exciton States in Self-Assembled Organic Chromophore Systems

Michele S. Myong

Creating sustainable and clean sources of energy is an outstanding problem of importance for the current generation of scientists to solve. Organic photovoltaics (OPVs) are a promising renewable energy source but require improvements to their architectures and better fundamental understanding of the effects of organic chromophore morphology on the resulting photophysical properties. To address these questions, we constructed chromophore assemblies and probed their photophysics with optical spectroscopies.

Self-assembly is an effective tool to create ordered systems through simple synthetic methods. Using anodic aluminum oxide (AAO) membranes, we built ordered assemblies of various organic chromophores that are relevant to light harvesting. These nanoscale architectures represent the mesoscale region between the solution and solid-state phases, providing an exciting opportunity to elucidate the behavior of the exciton and excimer states in these systems. We extended our studies of the exciton to the solid-state, using cocrystallization strategies to investigate the differential exciton diffusion processes between electronically similar cocrystals.

In PDI assemblies on AAO with different degrees of disorder, we demonstrate that the solvent environment can still modulate the excimer dynamics, even when the molecules are very strongly coupled to another through π-stacking interactions. The kinetics of excimer formation, relaxation, and decay are also influenced by the degree of disorder in the self-assembled chromophore system. BPEAs can be ordered in assemblies on AAO as well, and pump power dependent transient absorption studies reveal that the excimer state is diffusive. This challenges the assumption that the excimer is immobile because of its lower energy as a trap state and extends

the examples of a diffusive excimer exciton to supramolecular systems. The nature of the charge transfer exciton is probed in two electronically similar cocrystals composed of PDI and pyrene that have markedly different packing structures. In the final study, we outline the challenges and possibilities associated with probing exciton coherence lengths in a series of AAO assemblies with well characterized photophysical behavior.

These studies further our understanding of the exciton and excimer in ordered organic chromophore systems and offer future pathways to create organic materials with desirable energetics for energy conversion.

# Acknowledgments

My time in graduate school has been a period of incredible growth—intellectually, emotionally, spiritually—and I have so many people to thank for bringing me through the ups and downs of this path over the past five years.

First, thank you to Professor Michael Wasielewski for serving as my PhD adviser and guiding me through the process of becoming a scientist. I learned how to design and lead a project to completion, and I was given the intellectual freedom in your group to pursue any question I wanted. The structure and resources you provided grew my interest in scientific discovery and encouraged me to continue pursuing science.

Next, thank you to the professors who have served on my committee throughout graduate school. Professor Richard Schaller provided many useful insights during my qualifying exam as well as career advice. Professor Emily Weiss encouraged me to examine my research ideas more rigorously and served as my faculty mentor for the Teaching Certificate Program. Thank you to Professor Julia Kalow for stepping in on such short notice to serve on my defense committee.

I am fortunate to have been a member of the Wasielewski group because of how collaborative the group culture is, which is essential to doing great science. The creation of the Waz group Slack channel was an excellent idea to help the lab run smoothly and I loved how many threads we had for topics like random internet memes. Of course, we had important threads where we helped each other find chemicals, resolved lab safety issues, and shared noteworthy papers. In my earlier years, Dr. Jose Martinez and Dr. Joseph Christensen answered my many questions about organic synthesis and supported me as fellow members of B-lab. Prof. Nathan LaPorte shared his expertise in electrochemistry and FT-IR with me. I first learned about transient absorption

spectroscopy from Dr. Brian Phelan, who was excellent at explaining the complexities of time-resolved spectroscopy. Prof. Matthew Krzyaniak explained fundamentals of EPR and helped troubleshoot my TA fits. Prof. Yi-Lin Wu helped me get started on the AAO membrane research path and gave me silatrane compounds to jumpstart my work. Thank you to Dr. Natalia Powers-Riggs, Dr. Jenna Logsdon, and Su Chen for welcoming me into the self-assembly subgroup so I could pursue a new, exciting research path. And I am lucky to have shared an office with Jeremy Fisher, Jillian Bradley, and Malik Williams who are supportive and creative chemists.

I am so grateful for the exceedingly thorough and kind mentorship I have received from Prof. Ryan Young. Your extensive knowledge of spectroscopy and the vast field of photophysical chemistry is inspiring because you helped me easily understand numerous physical chemistry concepts and appreciate their elegance. Asking questions in graduate school can be intimidating, but when I had questions for you, I always came away with renewed interest in a project or clarity about the minutiae of a complex topic. Your rapid response to e-mails is admirable and your edits on my manuscripts were meticulous and helpful. Thank you so much, and I hope to be as good a mentor to younger scientists when I become a more experienced chemist.

The various experiments in my dissertation were run by my colleagues, who I would like to thank for their hard work. Prof. Ryan Young collected transient absorption data (Ch. 2 and 3). Dr. Michelle Chen also collected transient absorption data (Ch. 2). Dr. Jiawang Zhou collected time-resolved fluorescence data (Ch. 2). Yue Qi collected steady state and transient absorption microscopy data (Ch. 4). Su Chen collected steady state absorption and emission data (Ch. 5).

I have had great discussions and collaborations with numerous people in the Waz group, including Carolyn Ramirez about single crystal growth, Yue Qi and Dr. Itai Schlesinger about TAM and modeling, Laura Bancroft and Haochuan Mao about EPR, Dr. Natalia Powers-Riggs

about X-ray diffraction, Paige Brown about time-resolved fluorescence, Chenjian Lin about fluorescence, and Jonathan Schultz about setting up QChem and server issues. I would also like to thank Amanda Mahoney for being so skilled at her job and a warm presence in the main office.

I learned what it means to pursue justice, seek truth, and think critically about important issues from my friends Dr. Katie Fitzgerald, Yemi Ajisebutu, Sarah Lee, and Nathalia Justo. I cherish the last days I have with you in graduate school and hold our conversations about the church, politics, faith, and feminism close to my heart. I grew spiritually because of my time in the Graduate Christian Fellowship (GCF) at Northwestern, where I learned to integrate my faith and work. Thank you, Mickey Sanchez, for being such a thoughtful chaplain and showing me that the academic goal of knowledge production can work synergistically with my faith. I am forever changed by the grace and generosity that current and past GCF members have showed me, which has sustained me in graduate school. In my later years of grad school, I was lucky to have Prof. Leslie Hamachi join me at Northwestern after our time together at Columbia. Thank you, Leslie, for encouraging me in my scientific career and growing our friendship over board games and running. I am also blessed to have Eugenia Vasileiadou as my friend, who is an amazing solid-state chemist and motivates me to become a better mentor and scientist.

Mom, Dad, and Liz, thank you for your unconditional love and support during graduate school and my entire academic career. You instilled in me the curiosity and desire to learn, a strong work ethic, and the will to persist through difficult times. When I was consumed with pursuing my goals, you reminded me that I am loved and valued because of who I am and not what I have achieved. While examining my life in graduate school, I came to realize that I am foremost proud to be a daughter to my loving parents and a sister to my brilliant sibling. My identity is rooted in

my relationships with you and my friends, and I hope the culmination of my chemistry PhD journey magnifies that truth.

# Table of Contents

ABSTRACT ..... 2
Acknowledgments ..... 4
List of Figures ..... 11
List of Tables ..... 16
Chapter 1. Introduction ..... 17
1.1 MOTIVATION ..... 18
1.2 PHOTOPHYSICAL BEHAVIOR OF CHROMOPHORE ASSEMBLIES ..... 18
1.3 SELF-ASSEMBLY ..... 22
1.4 OUTLINE ..... 26
Chapter 2. Charge-Transfer Character in Excimers of Perylenediimides Self-Assembled on Anodic Aluminum Oxide Membranes ..... 29
2.1 INTRODUCTION ..... 30
2.2 RESULTS AND DISCUSSION ..... 32
2.2.1 Synthetic Rout ..... 32
2.2.1 Steady State Spectral Measurements ..... 33
2.2.2 Transient Absorption Spectroscopy ..... 35
2.3 CONCLUSIONS ..... 47
2.4 SUPPLEMENTARY INFORMATION ..... 48
2.4.1 Synthesis ..... 48
2.4.2 Assembly of PDIs on AAO Membranes ..... 48
2.4.3 Steady-State Spectral Measurements ..... 49
2.4.4 Femtosecond Transient Absorption (fsTA) Spectroscopy ..... 49
2.4.5 Time-Resolved Fluorescence (TRF) Spectroscopy. ..... 50
2.4.6 Kinetic Analysis of fsTA Data ..... 52
2.4.7 Fourier Transform Infrared Spectroscopy characterization of octadecyltriethoxysilane chains on the AAO surface. ..... 54
2.4.9 Additional Steady-State Absorption Spectroscopy ..... 55

Chapter 3. Excimer Diffusivity in 9,10- Bis(phenylethynyl)anthracene Assemblies on Anodic Aluminum Oxide Membranes....60
3.1 INTRODUCTION....61
3.2 EXPERIMENTAL....64
3.2.1 Synthesis....64
3.2.2 Preparation of AAO Assemblies....64
3.2.3 Transient Absorption Spectroscopy....65
3.3 RESULTS AND DISCUSSION....65
3.3.1 Properties of the BPEA-AAO membrane assemblies....65
3.3.2 Steady-State Optical Properties....66
3.3.3 Excited-State Dynamics....67
3.3.4 Excimer Mobility in One Dimension....70
3.4 CONCLUSIONS....73
3.5 SUPPLEMENTARY INFORMATION....74
3.5.1 Synthesis....74
3.5.2 Average Distance between BPEAs on Nanoporous AAO Membranes....77
3.5.3 Femtosecond Transient Absorption Spectroscopy....79
3.5.4 Calculation of Excitation Density....83
3.5.5 Calculation of Diffusion Coefficient....85
3.5.6 Annihilation Rate vs. Power....86
Chapter 4. Ultrafast Photo-driven Charge Transfer Exciton Dynamics in Mixed-Stack Pyrene-Perylenediimide Single Cocrystals....88
4.1 INTRODUCTION....89
4.2. EXPERIMENTAL....90
4.2.1 Steady state absorption and emission microscopy....90
4.2.2 Transient absorption microscopy....91
4.3 RESULTS....92
4.3.1 Donor-acceptor cocrystal structures....92
4.3.2 Steady state absorption and emission....94
4.3.3 Transient absorption microscopy....96
4.4 DISCUSSION....98

4.4.1 CT exciton diffusion and decay dynamics ..... 98
4.5 CONCLUSIONS ..... 102
4.6 SUPPLEMENTARY INFORMATION ..... 102
4.6.1 Crystal Growth and Structure Determination ..... 102
4.6.2 Single Crystal X-ray Diffraction ..... 103
4.6.3 Steady-state Absorption and Emission Microscopy ..... 107
4.6.4 Polarized Absorption Plots ..... 108
4.6.5 Femtosecond Transient Absorption Microscopy ..... 114
4.6.6 Pump and probe spot sizes ..... 115
4.6.7 Calculation of excitation density ..... 115
4.6.8 Calculation of diffusion coefficients ..... 116
Chapter 5. Exciton Coherence in Assemblies of Rylene Dyes on Anodic Aluminum Oxide Membranes ..... 118
5.1 INTRODUCTION ..... 119
5.2 EXPERIMENTAL ..... 121
5.2.1 Assembly of AAO membrane systems ..... 121
5.2.2 Steady state absorption and emission ..... 122
5.3 RESULTS ..... 123
5.3.1 Nature of chromophore aggregation (absorption) in different dielectric environments ..... 123
5.3.2 Comparing the exciton coherence length ..... 127
5.3.3 Excitation wavelength dependent emission in tpPDI-AAO ..... 131
5.4 CONCLUSIONS ..... 132
5.5 SUPPORTING INFORMATION ..... 133
5.5.1 Calculation of Huang-Rhys factors ..... 133
5.5.2 Gaussian fits of AAO steady state emission spectra ..... 135
References ..... 138

# List of Figures

Figure 1.1. *Left:* Energy level diagram depicting relative excimer energies of molecules 1-4. *Right*: Structure of PDI and PDI dimers studied using near-infrared transient absorption spectroscopy. Reprinted with permission from J. Phys. Chem. Lett. 2014, 15, 2588–2593. Copyright 2014, American Chemical Society. ..... 21

Figure 1.2. (a) Depiction of AAO membrane showing the nanoporous alumina and barrier layers on an aluminum substrate. (b) Scanning electron microscope image of the porous AAO surface. Adapted from InRedox website, 2021, retrieved from https://www.inredox.com/technology/anodic-aluminum-oxide. Copyright 2017, InRedox LLC.23

Figure 2.1. Synthesis for the PDI series investigated here. ..... 32

Figure 2.2. (a) UV-Vis spectra and (b) fluorescence spectra of PDI derivatives 1 and 2 in DCM solution. (c) UV-Vis spectra and (d) fluorescence spectra of 1 and 2 in AAO membranes. ..... 34

Figure 2.3. FsTA spectra at the indicated times of PDI 1 covalently bound to an AAO membrane with its pores containing a) $H_2O$, b) DCM, c) toluene, and d) air. The oscillations in the spectra of 1/AAO/$H_2O$ (a) result from interference effects from the regular array of AAO pores. ..... 36

Figure 2.4. FsTA spectra at 50 ps of (a) PDI silatrane 1 covalently attached to the AAO membrane, and (b) PDI 2 intercalated into the silylated AAO membrane. The AAO membrane pores contain the indicated solvents. The cation band at 610 nm is highlighted. ..... 37

Figure 2.5. FsTA spectra of 2 at the indicated times intercalated in the silylated AAO membrane with its pores containing a) water, b) DCM, c) toluene, and d) air. ..... 38

Figure 2.6. Decay-associated spectra for 1/AAO in (a) air, (b) toluene, (c) DCM, and (d) $H_2O$. 42

Figure 2.7. Decay-associated spectra for 2/AAO in (a) air, (b) toluene, (c) DCM, and (d) $H_2O$. Data between 550-570 nm for (a-c) and below 550 nm (d) are obscured by pump scatter and are omitted. ..... 44

Figure 2.8. Left: Depiction of 1/AAO with PDIs arranged as *H*-aggregates and of Right: 2/AAO with PDIs intercalated in lipid and aggregated in numerous orientations. ..... 46

Figure 2.9. Time-resolved fluorescence of 1 covalently attached to AAO. Kinetic fits at selected wavelengths for the a) 50 ns time window, and c) 5 ns time window. Decay-associated spectra for the b) 50 ns time window and d) 5 ns time window. IRF is ~2% of time window. ..... 50

Figure 2.10. Time-resolved fluorescence of 2 intercalated in AAO. Kinetic fits at selected wavelengths for the a) 10 ns time window, and c) 2 ns time window. Decay-associated spectra for the b) 10 ns time window and d) 2 ns time window. IRF is ~2% of time window. ..... 52
Figure 2.11. Left: FTIR spectrum of AAO coated in 0.1 mM of octadecyltriethoxysilane for 24 h. Middle: Concentration study of octadecyltriethoxysilane in carbon tetrachloride ($CCl_4$). Right: FTIR spectrum of uncoated AAO which exhibits no stretch at ~3000 $cm^{-1}$. ..... 54
Figure 2.12. Left: Scanning electron microscope (SEM) image of the edge of an AAO membrane. Right: SEM image of the top of an AAO membrane..... 54
Figure 2.13. Unnormalized UV-Vis spectra of 1/AAO/DCM and 2/AAO/DCM. ..... 55
Figure 2.14. TA spectra for a solution of 1 (left) and 2 (right) in DCM acquired with $\lambda_{ex}$ = 534 nm, ~110 fs pulses. ..... 55
Figure 2.15. TA spectra for 1/AAO and 2/AAO in MeCN and DMSO. ..... 56
Figure 2.16. Decay-associated spectra for 1/AAO and 2/AAO in MeCN and DMSO. ..... 57
Figure 2.17. Kinetic fits for 1/AAO. (DCM = $CH_2Cl_2$; MeCN = acetonitrile; DMSO = dimethylsulfoxide)..... 58
Figure 2.18. Kinetic fits for 2/AAO. (DCM = $CH_2Cl_2$; MeCN = acetonitrile; DMSO = dimethylsulfoxide)..... 59
Figure 3.1. Synthesis of silyl-BPEA (3) by Sonogashira coupling of 1 and 2. ..... 64
Figure 3.2. Steady-state absorption of emission spectra of silyl-BPEA (a) in solution and (b) on AAO membranes. ..... 66
Figure 3.3. (a) fsTA spectra of silyl-BPEA covalently bound to AAO; (b) The decay-associated spectra extracted from the decay-associated global fit. ..... 67
Figure 3.4. (a) Power dependence of ΔA signal at 600 nm where the excimer exciton photoinduced absorption band appears, taken as the average from 595-605 nm. (b) Fit of the TA data to the one-dimensional exciton annihilation model at different pump powers..... 71
Figure 3.5. Schematic of AAO membranes depicting the parameters used for calculation of the average BPEA spacing..... 77
Figure 3.6. fsTA spectra of monomeric silyl-BPEA in dichloromethane following 414 nm, ~100 fs excitation (1 μJ/pulse) at 500 Hz. ..... 79

Figure 3.7. fsTA spectra of BPEA-AAO at 0.25 mW pump power: a) spectra, b) kinetic fits at selected wavelengths, c) decay-associated spectra, d) species populations..... 79
Figure 3.8. fsTA spectra of BPEA-AAO at 0.5 mW pump power: a) spectra, b) kinetic fits at selected wavelengths, c) decay-associated spectra, d) species populations..... 80
Figure 3.9. fsTA spectra of BPEA-AAO at 0.75 mW pump power: a) spectra, b) kinetic fits at selected wavelengths, c) decay-associated spectra, d) species populations..... 81
Figure 3.10. fsTA spectra of BPEA-AAO at 1.0 mW pump power: a) spectra, b) kinetic fits at selected wavelengths, c) decay-associated spectra, d) species populations..... 82
Figure 3.11. fsTA spectra of BPEA-AAO at 1.25 mW pump power: a) spectra, b) kinetic fits at selected wavelengths, c) decay-associated spectra, d) species populations..... 83
Figure 3.12. The area of an annulus of BPEA molecules in the AAO pore is highlighted in green. ..... 84
Figure 3.13. Rate coefficient of annihilation (from fitting to a one-dimensional annihilation model) vs. pump power. Annihilation rate decreases as power increases. ..... 86
Figure 4.1. Pyr-diisoPDI cocrystal structure: (a) View down the *b*-*c* crystallographic plane with the interstack distance labeled, (b) View down the *a*-*c* crystallographic plane with the Pyr-diisoPDI and diisoPDI-diisoPDI distances labeled as well as the angle between the planes of the molecules and the crystallographic *c*-axis, and (c) View nearly in line with the crystallographic *b*-axis showing the edge-to-edge π-π distances of Pyr-Pyr, Pyr-diisoPDI, and diisoPDI-diisoPDI. Pyr-$C_5$PDI cocrystal structure: (d) View down the *a*-*c* crystallographic plane with intrastack and interstack distances labeled, (e) View down the *a*-*b* crystallographic plane, (f) View down the crystallographic *a*-axis with the Pyr- $C_5$PDI, $C_5$PDI- $C_5$PDI, and Pyr-Pyr distances labeled. ..... 93
Figure 4.2. Steady-state absorption spectra at various polarizations with respect to the macroscopic crystal long axis (crystallographic *a*-axis), and unpolarized PL of (a) Pyr-diisoPDI cocrystal and (b) Pyr-$C_5$PDI cocrystal. ..... 95
Figure 4.3. FsTAM spectra of the Pyr-diisoPDI cocrystal with probe polarized (a) perpendicular or (b) parallel to crystallographic *a*-axis and of the Pyr-$C_5$PDI cocrystal with probe polarized (c) perpendicular or (d) parallel to crystallographic *a*-axis. ..... 97
Figure 4.4. (a) Kinetic fits to a bimolecular, one-dimensional decay model at two different pump fluences for Pyr-diisoPDI with the indicated pump and probe polarizations. (b) Kinetic fits to a bimolecular, one-dimensional decay and first order decay model at two different pump fluences

for the Pyr-diisoPDI cocrystal with the indicated pump and probe polarizations. Oscillations in the data are due to acoustic phonons produced in the cocrystal at higher pump powers. (c) Kinetic fits to a bimolecular, one-dimensional decay and first order decay model in the Pyr-$C_5$PDI cocrystal with the indicated pump and probe polarizations. The pump energy is 2.3 μW for both polarizations. Oscillations in the data are due to acoustic phonons produced in the cocrystal at higher pump powers. ..... 99
Figure 4.5. BFDH calculations were completed in Mercury for Pyr-diisoPDI cocrystal. (a) View of the crystal along the (002) axis shows the molecules stack with their transition dipole moments perpendicular to the long axis of the crystal. (b) View of the crystal along the (100) axis shows a degree of interstack overlap, though the planes of the molecules are not perfectly cofacial with the axis of the crystal. (c) Manual face indexing of the mounted single crystal that was diffracted shows reasonable agreement with the BFDH calculated structures. ..... 105
Figure 4.6. BFDH calculations were completed in Mercury for Pyr-$C_5$PDI cocrystal. (a) View of the crystal along the (010) axis shows the molecules stack with their transition dipole moments perpendicular to the long axis of the crystal. (b) View of the crystal along the (100) axis shows cleanly segregated stacks, with the planes of the molecules perfectly cofacial with the axis of the crystal. (c) Manual face indexing of the mounted single crystal that was diffracted shows reasonable agreement with the BFDH calculated structures. ..... 106
Figure 4.7. Pyr-diisoPDI measured with probe at various polarizations. ..... 108
Figure 4.8. Pyr-diisoPDI measured with probe at various polarizations. ..... 109
Figure 4.9. Pyr-diisoPDI measured with probe at various polarizations. ..... 110
Figure 4.10. Pyr-$C_5$PDI measured with probe at various polarizations. ..... 111
Figure 4.11. Pyr-$C_5$PDI measured with probe at various polarizations. ..... 112
Figure 4.12. Pyr-$C_5$PDI measured with probe at various polarizations. ..... 113
Figure 4.13. Gaussian fits for (a) probe and (b) pump spot sizes. Objective lens: Nikon (Plan fluor, ELWD, 60X/0.7) ..... 115
Figure 5.1. Depiction of perylene excimer, excimer with CT character, SB-CT, and SB-CS states. Adapted with permission from J. Phys. Chem. C 2021, 27, 14843–14853. Copyright 2021, American Chemical Society. ..... 121
Figure 5.2. Chemical structures of (a) 3-(phenylethynyl)perylene (PEP), (b) Tetrakis(4-tert-butylphenoxy)PDI, (c) PDI silatrane, and (d) PDI with C23 tails. ..... 122

Figure 5.3. Absorption spectra of (a) 3-(phenylethynyl)perylene (PEP) on AAO, (b) Tetrakis(4-tert-butylphenoxy)PDI on AAO, (c) PDI silatrane on AAO, and (d) PDI intercalated on AAO in water, MeCN, THF, DCM, and toluene..... 123
Figure 5.4. Emission spectra of (a) 3-(phenylethynyl)perylene (PEP) on AAO, (b) Tetrakis(4-tert-butylphenoxy)PDI on AAO, (c) PDI silatrane on AAO, and (d) PDI intercalated on AAO in water, MeCN, THF, DCM, and toluene. ..... 127
Figure 5.5. Excitation wavelength-dependent emission spectra of tetrakis(4-tert-butylphenoxy)PDI on AAO in water. ..... 131
Figure 5.6. Gaussian fits to monomer steady state absorption spectra for AAO systems discussed. Huang-Rhys factor is calculated from the ratio of the areas under the Gaussian fits to the 0-1 and 0-0 vibronic bands..... 133
Figure 5.7. Gaussian fits to emission spectra of 3-(phenylethynyl)perylene on AAO in different solvents. ..... 135
Figure 5.8. Gaussian fits to emission spectra of tetrakis(4-tert-butylphenoxy)PDI on AAO in different solvents..... 136
Figure 5.9. Gaussian fits to emission spectra of PDI intercalated on AAO in different solvents. ..... 137

# List of Tables

**Table 2.1.** Steady-state spectral data in DCM at 298 K. ..... 35

**Table 2.2.** Comparison of fsTA time constants of kinetic species for 1/AAO and 2/AAO in air, toluene, DCM, and $H_2O$. ..... 46

**Table 3.1**: Excitation density at different powers ..... 84

**Table 3.2.** Parameters for calculating number of photons, $Np$ ..... 84

**Table 3.3.** Parameters for calculating excitation volume, $V$ ..... 85

**Table 4.1.** Rate constants and diffusion coefficients for Pyr-diisoPDI and Pyr-$C_5$PDI cocrystals at different pump polarizations. ..... 101

**Table 4.2.** Excitation density parameters. ..... 115

**Table 5.1**: Steady-state absorption spectral data in various solvents at 298 K. ..... 125

**Table 5.2**: Calculated 0-0 to 0-1 peak ratio from the steady state emission spectra. ..... 128

**Table 5.3**: Calculated coherence length, $N_{coh}$ ..... 129

**Table 5.4.** List of Huang-Rhys factors ..... 134

# Chapter 1.

# Introduction

## 1.1 MOTIVATION

A significant global development is the rising world energy consumption, which is projected to increase steadily from present day to 2040.[1] The development of renewable energy sources has the potential to meet these energy demands in an environmentally responsible manner and decrease the use of fossil fuels, which has led to unprecedented climate change. One renewable energy source is solar energy, which is captured and converted into chemical energy during photosynthesis. Efforts to understand the process of photosynthesis has led to the design of synthetic molecular systems that mimic the chromophore assemblies found in photosynthetic organisms and also convert light into chemical energy, part of the field of artificial photosynthesis.[2]

Organic photovoltaic (OPV) devices are a potential renewable energy source, which produce electrical energy through the absorption of a photon by a semiconductor material.[3] Compared to the widely used Si photovoltaic solar cells, OPVs offer several advantages since they are flexible, lightweight, and composed of earth-abundant materials. Despite these advantages, OPVs have a lower power conversion efficiency than their inorganic counterparts, due in part to nanoscale morphology of the organic chromophores. Therefore, understanding the effects of chromophore morphology on the photophysical properties is essential to improving OPV performance. In the sections below, we discuss concepts relevant to understanding light-matter interactions of organic chromophores in self-assembled nanostructures.

## 1.2 PHOTOPHYSICAL BEHAVIOR OF CHROMOPHORE ASSEMBLIES

The light harvesting complexes in photosynthetic organisms are composed of many chromophores that store and transfer energy in their excited electronic states until it is delivered to a reaction center.[4-7] These chromophore sites concentrate excitation energy, and this coherently delocalized excitation is known as an exciton, which has a distinct spectroscopic signature. Frenkel

excitons are strongly bound electron-hole pairs that are often found in organic materials and are formed when a photoactive material is excited, promoting an electron from the highest occupied molecular orbital (HOMO) to the lowest occupied molecular orbital (LUMO).

*Excitons in molecular aggregates*

The key light harvesting complex, LHCII, binds several chlorophylls that share a coherently delocalized excitation and the transfer of this energy occurs through resonant energy transfer.[8] The exciton in photosynthetic systems are fairly localized, with a delocalization length of two to four chromophores.[9] The exciton model was first used by Davydov to explain excitations in the solid state, particularly in molecular crystals.[10] Kasha expanded this model to molecular systems, which has also been applied to describing interchromophore interactions in photosynthetic systems.[11-12]

In multichromophore photosynthetic systems, the Frenkel exciton model assumes a weak coulombic interaction between chromophores compared to the forces that define the electronic structure of the individual molecules.[13] Therefore, the exciton eigenstate in a molecular system with an excitation delocalized over several molecules is well described by a linear combination of the individual chromophore eigenfunctions. This delocalization manifests as new bands in the absorption spectra and different photophysical response related to energy transfer.

Spano and coworkers laid out a theoretical framework to understanding the photophysical behavior of molecular aggregates that include rylene dyes, since this class of molecules can form both *H* and *J*-aggregates.[14] Kasha defined *H*-aggregates as molecular dimers that are cofacially stacked and whose absorption maximum is blue-shifted; *J*-aggregates are “head-to-tail” stacked with a red-shifted absorption maximum. Building on Kasha’s model that assumes only long-range Coulomb coupling, Spano et al. consider short-range coupling comparable to Coulomb coupling

in π-stacked systems where wavefunction overlap is significant. In certain systems, Frenkel/CT mixing can lead to *H* or *J*-aggregate behavior when Coulomb coupling is absent. On the other hand, Coulombic and CT interactions are both present in certain systems such as 7,8,15,16-tetraazaterrylene (TAT) nanopillars.[15]

Gregg and Kose observed a reversible transition from *H* to *J*-aggregates in a perylenediimide liquid crystal and associated the H-form with primarily Frenkel exciton contribution and the J-form with mixed Frenkel/CT excitons.[16-17] Frenkel/CT exciton mixing is also important in explaining the Davydov splitting in oligoacenes.[18] Therefore, controlling the degree of mixing between the CT and Frenkel excitons determines the excitonic coupling and transport.

*Excimer trap state*

When incorporated into a supramolecular assembly, conjugated aromatic molecules often exhibit strong electronic coupling to one another through intermolecular π-π interactions. This coupling can lead to trapping of localized Frenkel excitons in sites where the sum of the stabilization energies exceeds the repulsion energy of the (M + M*) state.[19] The excimer state is destabilized by repulsion energy $E_R$ and at the same time, is stabilized by delocalization of the excited state over the two molecules.[20] The energy level splits into two states due to the exciton interaction energy $E_S^{exc}$. The charge transfer interaction also stabilizes the excimer state in addition to the exciton interaction, and its stabilization energy $E_S^{CT}$ contributes to the binding energy $E_B$ of the excimer:

$$E_B = E_S^{exc} + E_S^{CT} - E_R \qquad \text{Eq. 1}$$

The excimer state has been studied by Brown et al. in a series of PDI dimers (Figure 1.1) to explore how interchromophore electronic coupling affects PDI excimer dynamics.[20] In the near-

infrared (NIR) femtosecond transient absorption spectra of the excimer-forming PDI dimers, an absorption band on the red edge of the NIR window is observed. Katoh et al. observed a similar feature, which they assigned to the transition from the Frenkel state $^1$*(MM) to a higher energy CT state ($M^+M^-$).[19, 21] Kinetics of the PDI dimer **4** in Figure 1.1 show that the excimer state decays in 2.5 ns, which is much shorter than that of dimers 2 and 3. Generally, short excimer decay times are associated with small π-stacking distances, likely due to large vibrational interactions between the bound PDI monomers.[22]

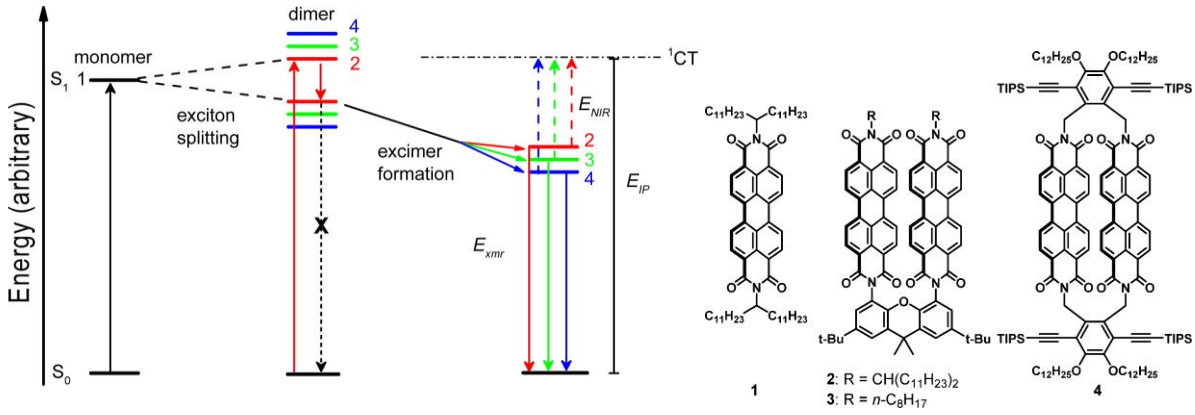


**Figure 1.1.** *Left:* Energy level diagram depicting relative excimer energies of molecules 1-4. *Right*: Structure of PDI and PDI dimers studied using near-infrared transient absorption spectroscopy. Reprinted with permission from J. Phys. Chem. Lett. 2014, 15, 2588–2593. Copyright 2014, American Chemical Society.

The excimer state is classically defined as a superposition of the wavefunctions of the Frenkel exciton states $|M_1^*M_2\rangle$ and $|M_1M_2^*\rangle$ of each molecule in the excimer, and charge transfer (resonance) states $|M_1^+M_2^-\rangle$ and $|M_1^-M_2^+\rangle$:

$$|Ex\rangle = \alpha(|M_1^*M_2\rangle + |M_1M_2^*\rangle) + \beta(|M_1^+M_2^-\rangle + |M_1^-M_2^+\rangle) \qquad \text{Eq. 2}$$

α and β are the relative contributions of the local excited state and charge transfer states. These coefficients can be modified by changes in dielectric environment or interchromophore distance.[23]

Additionally, the excimer is one of the products that results from dephasing of the coherent superposition of three diabatic states. The local excited singlet exciton $|^1(S_1S_0)>$, charge transfer |CT>, and triplet pair $|^1(T_1T_1)>$ states mix and represent an admixture that changes in composition over time.[24] Excimer-like states can mediate singlet fission (SF) as well as charge separation (CS) when it is coupled to a correlated triplet in singlet fission or loses its contribution from the local excited singlet exciton state. Therefore, the possibility of directing the conversion between excimers, singlet fission, and symmetry-breaking charge transfer for applications in OPVs is an exciting research target.

## 1.3 SELF-ASSEMBLY

The process of self-assembly transforms a disordered system into an ordered structure through local interactions of its components, offering an effective bottom-up approach to access a range of nanoscale architectures. Assemblies of organic chromophores have been formed by exploiting π-π interactions, hydrogen bonding,[25-27] incompatible solvent interactions,[28-29] and pH environment.[30] In this work, the interacting units are molecules that form organized patterns of molecules upon incorporation into nanostructures or through crystallization. This allows us to explore the light-matter interactions of nanoscale assemblies whose external environment can be modulated and has significant effects on its photophysical properties.

*Anodic aluminum oxide (AAO) membranes*

Supramolecular self-assembly can be facilitated by using nanotemplates with high porosity that are also used for nanofiltration, separation, and storage.[31] In particular, anodic aluminum oxide (AAO) membranes have been used to graft polymers,[32] build heterostructures of chiral nanoscale channels,[33] and constrain self-assembled monolayers of alkylphosphonates to molecular order in the films.[34] The pores in AAO membrane are formed through a simple electrochemical oxidation

process, resulting in self-organized cylindrical structures (Figure 1.1). AAO membranes with various pore lengths, diameters, and interpore distances can be fabricated by controlling the anodization process and this tunability makes the AAO membranes attractive candidates for building heterostructures with a variety of applications.

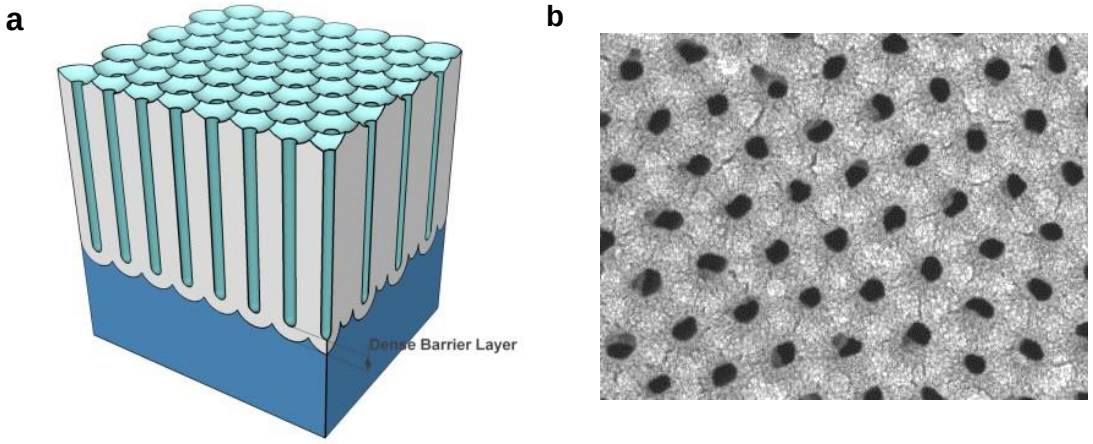


**Figure 1.2.** (a) Depiction of AAO membrane showing the nanoporous alumina and barrier layers on an aluminum substrate. (b) Scanning electron microscope image of the porous AAO surface. Adapted from InRedox website, 2021, retrieved from https://www.inredox.com/technology/anodic-aluminum-oxide. Copyright 2017, InRedox LLC.

The tunability of the AAO pore size has led to studies regarding the effects of nanoconfinement on the aggregation of organic semiconductors. A series of nanoconfined planar molecules exhibited size dependent H- or J-aggregation, which manifested as changes in the relative ratio of the $A^{0-0}$ and $A^{0-1}$ vibronic peaks.[35] This study demonstrates that the AAO nanostructure can impact the orientation of molecular aggregates and their optical properties. Previously, we controlled the orientation of spin-correlated radical pairs (SCRPs) by covalently linking the molecules to AAO pore walls.[36] The linear donor-chromophore-acceptor (D-C-A) molecule was photoexcited in a 343 mT magnetic field to yield a radical ion pair that undergoes intersystem crossing, resulting in spin-polarized time-resolved electron paramagnetic resonance

(EPR). The orientation of the SCRPs with respect to the AAO pore walls was determined through the dependence of the electron spin polarization phase of the spectra relative to the applied magnetic field.

Building on our previous work aligning SCRPs on AAO membranes, we applied the method of covalently attaching organic molecules to the native oxide surface of the AAO pore walls. Namely, by attaching a triethoxy silyl group or silatrane linker to an organic chromophore, we were able to react the hydroxyl groups on the AAO surface with the linker groups to create assemblies of organic chromophores on AAO. These organic-inorganic hybrid nanostructures represent the mesoscopic region between the solution phase and solid state, creating a synthetic route to explore light-matter interactions on the mesoscale.

*Donor-acceptor cocrystals*

The assembly of two components into an ordered supramolecular structure can be achieved through noncovalent interactions, including charge-transfer (CT) interactions between donor and acceptor molecules.[37] These donor-acceptor (D-A) cocrystals display properties that are greater than the sum of the physicochemical properties of its individual donor and acceptor components.[38-40] Strong CT interactions drive cocrystal self-assembly, often leading to one-dimensional (1D) supramolecular structures or 1D CT exciton migration.[41-42]

Changes in the cocrystal morphology results in markedly different luminescent properties, which demonstrates that the photophysical characteristics are determined by their molecular packing modes and supramolecular interactions.[43-46] Supramolecular interactions in D-A cocrystals can include π-π interactions, halogen bonding interactions, and charge transfer (CT) interactions. A family of three organic cocrystals composed of a cyanostilbene derivative (BPPa) donor and a diiodo-tetrafluorobenzene (2I), triiodo-trifluorobenzene (3I), or 1,2,4,5-

tetracyanobenzene (TCNB) acceptor were synthesized. Each of the three cocrystals exhibited a different degree of CT interaction strength based on the intermolecular packing, which impacted the fluorescence lifetimes and led to multicolor emission from the cocrystals. As the strength of the π-π interactions in the cocrystals increased, the strength of CT transitions in the steady state absorption spectra increased and the wavelength of emission red-shifted.[43] Therefore, the type and strength of supramolecular interactions in cocrystals with similar constituent donor and acceptor molecules directly impact their photophysical properties.

The optical properties of cocrystals can also directly be attributed to the different properties of the donor (D) and acceptor (A). Examination of the crystal structure of four D-A cocrystals, with a distyrylbenzene (DSB) type donor and dicyanodistyrylbenzene (DCS) type acceptor, showed they were isomorphic/quasi-isostructural crystals in the π-stack direction. Due to their quasi-isostructural nature, the complex effects of morphology on the photophysics were reduced and the differences in the CT emission could be attributed to electronic differences between the DSB donor and DCS acceptor derivatives. Some structural differences such as the decreased D-A distance in the cocrystal due to the increased CT strength remained, though the effect of the electronic structure on the photophysics was evident in that the lifetimes of the two decay components of the time-resolved emission spectra increased as the CT strength decreased in the cocrystals. The differences in the photoluminescence quantum yields (0.83, 0.69, 0.63, and 0.31 as the emission color goes from green to red) between the four cocrystals were attributed to the differences in the rates of non-radiative decay and the small but nonzero calculated oscillator strengths of the cocrystals.[47] This study highlights the importance of electronic structure on the physical properties of cocrystals as well as the difficulty of decoupling morphological from electronic effects.

Rylene dyes have been incorporated into a series of four, 1D mixed-stack D-A cocrystals, with pyrene and perylene donors and perylenediimide (PDI) derivative as the acceptor.[48] Perylene has also been incorporated into a family of perylene-TCNQ cocrystals with different stoichiometric ratios of the donor and acceptor.[49] Further exploration of the morphology of rylenes incorporated into D-A cocrystals could increase our understanding of how molecular orientation affects photophysics in the solid state.

**1.4 OUTLINE**

The following chapters document our work using anodic aluminum oxide (AAO) membranes and cocrystal self-assembly methods to create ordered assemblies of organic chromophores that undergo different photophysical processes upon interacting with light. The nature of the excimer and exciton states are probed using time-resolved and steady state optical spectroscopies.

In Chapter 2, two perylene-3,4:9,10-bis(dicarboximide) (PDI)-based electron acceptor derivatives are incorporated into AAO membranes, which results in the creation of two self-assembled organic chromophore systems with different degrees of disorder. In one system, the PDI molecule has an *n*-propyl silatrane attached to one of its imide nitrogens, while a 12-tricosanyl group is attached to the other imide nitrogen. The silatrane reacts with the AAO surface to covalently bind the PDI. The other PDI has 12-tricosanyl groups on both imide nitrogens, which intercalate with *n*-octadecylsilane chains covalently bound to an AAO membrane. Steady-state and time-resolved measurements reveal that the PDI molecules are strongly associated with one another, resulting in enhancement of the 0-1/0-0 vibronic band ratio in the absorption spectra and broadened, red-shifted emission. Both PDI derivatives form excimers within a few picoseconds upon photoexcitation with and without solvent in the AAO membrane pores, which display

increasing charge transfer character with increasing solvent polarity. The results presented here show how to tune the intermolecular interactions of PDI and related rylene dyes attached to walls of the AAO pores to understand the intermediate regime between solution and the solid state.

In Chapter 3, we model a photosynthetic light harvesting system and study the energy transfer within a supramolecular assembly of 9,10-bis(phenylethynyl)anthracene (BPEA) chromophores. Excimers usually serve as low energy trap sites in supramolecular chromophore assemblies; however, if the trap is not too deep, excimers may diffuse throughout the structure, making it possible to delivery excitation energy to distant sites. To investigate this phenomenon, an asymmetric BPEA molecule was synthesized using Sonogashira coupling, with one end of the molecule containing a triethoxysilyl group that can covalently bind to the pore walls of the AAO and form a supramolecular assembly of 9,10-bis(phenylethynyl)anthracene (BPEA) chromophores. The BPEA molecules self-associate and form excimers upon photoexcitation. Excimer formation in the BPEA assemblies on the AAO membranes is a multi-step process and involves intermolecular structural reorganization between the chromophores. Describing the system using exciton theory reveals that the BPEA excimer is mobile, despite its frequent role as a lower energy trap state, where excimer exciton mobility is confined to one-dimension. The BPEA on AAO system shows excimer exciton diffusivity is higher than that of other excimer excitons, approaching that of singlet exciton in efficient organic photovoltaic systems.

In Chapter 4, we use solution-phase molecular self-assembly to cocrystallize a pyrene (Pyr) electron donor with either *N*,*N*′-bis(2,6-diisopropylphenyl)- or *N*,*N*′-bis(3-pentyl)perylene-3,4:9,10-bis(dicarboximide) (diisoPDI or $C_5$PDI) electron acceptors. Cocrystal formation through vapor diffusion yields mixed π-stacked Pyr-diisoPDI or Pyr-$C_5$PDI donor-acceptor cocrystals. Solving the cocrystal structures shows that the morphology of Pyr-diisoPDI differs significantly

from that of Pyr-$C_5$PDI and that the Pyr-diisoPDI displays significant interstack wavefunction overlap and edge-to-edge interactions. The charge-transfer (CT) exciton diffusion dynamics in these single crystals was probed using femtosecond transient absorption microscopy. Fitting the data to a one-dimensional charge transfer (CT) exciton diffusion model reveals diffusion constants that are two orders of magnitude higher in the Pyr-diisoPDI cocrystal compared the Pyr-C5PDI cocrystal. By correlating the cocrystal structures to their distinct excited state dynamics, the effects of each mixed stacked structure on the exciton dynamics and the mechanisms of CT exciton diffusion were determined.

Lastly, in Chapter 5 we explore the exciton coherence (delocalization) length of a series of rylene dyes self-assembled on AAO in different solvents. The steady-state absorption showed similar $A^{0\text{-}1}/A^{0\text{-}0}$ vibronic transition ratios in each system regardless of dielectric environment. The $I^{0\text{-}0}/I^{0\text{-}1}$ vibronic transition ratios in the emission of the aggregated perylene derivatives on AAO varied slightly between certain solvent polarities. The Huang-Rhys factor for the monomers that were incorporated into the AAO systems were calculated. This analysis revealed coherence lengths ($N_{coh}$) of less than 1, indicating that coherence exists only in the ultrafast region (10-100 fs). Thus, the exciton is incoherent in these systems and the analysis is applicable for H- and J-aggregates only within the ultrafast window of time-resolved emission.

# Chapter 2.

# Charge-Transfer Character in Excimers of Perylenediimides Self-Assembled on Anodic Aluminum Oxide Membranes

## 2.1 INTRODUCTION

Mimicking natural supramolecular chromophore assemblies, such as light-harvesting chromophore assemblies in photosynthetic antenna proteins, is a prime target for solar energy conversion.[50] Varying the distance and geometry between chromophores within an assembly is well known to change the excitonic coupling between them.[51] For example, a study of merocyanine 540 (MC540) adsorbed on $TiO_2$ semiconductor nanoparticles shows a mix of aggregated and monomeric forms of the sensitizer, while MC540 modified with Aerosol-OT (OTA) is primarily monomeric.[52] When the MC540-sensitized $TiO_2$ electrode is combined with an electroactive polymer, the incident photon-to-photocurrent generation efficiency is significantly higher when the dye sensitizer is monomeric rather than aggregated. That study demonstrated that weakly coupled chromophores can promote higher charge injection efficiencies on semiconductor surfaces. On the other hand, *H*-aggregation increases quantum yields for electron injection and light-harvesting efficiencies of rhodamine derivatives on $TiO_2$ surfaces.[53] Both findings demonstrate the importance of the degree of dye aggregation on light-harvesting efficiencies. Organic small molecules have been studied as photoactive surfaces in both dye-sensitized solar cells (DSSCs) and organic photovoltaics (OPVs), and efforts to develop donor-acceptor sensitizers that can be concurrently used in both DSSCs and OPVs are ongoing.[54] A clearer understanding of the optical properties of chromophore aggregates in DSSCs will thus be applicable to improved efficiencies in OPVs.

The performance of OPVs using non-fullerene acceptors is often hindered by the trapping of excitons by excimer states. Two chromophores often adopt face-on conformations in which their electronic structure is a superposition of Frenkel exciton states and two charge transfer (CT) states having varying contributions.[55] It has been shown that solvent polarity can influence the

extent of the CT state contribution to the excimer electronic structure. CT states are stabilized by polar solvents, and this stabilization can reduce the energy needed for excimer formation. As CT states become more involved in excimer formation, the emission spectra of the system become more redshifted.[56] When the CT states are stabilized, they can make the structural rearrangement necessary for excimer formation easier to access.[57-58] Evidence of the involvement of CT states can be found in excimer emission spectra and the appearance of bands associated with radical ion-like absorption in transient absorption spectra.[23] Excimers have also been implicated as intermediates in singlet exciton fission[59-61] and their CT state energy is important in this process.[62]

Perylenediimide (PDI) supramolecular dye assemblies have been studied because of their applications to organic semiconductors, and the self-assembly of core-unsubstituted PDIs in solution and solid state has been widely investigated.[63-67] However, the self-assembly properties of PDIs in unusual solvation conditions are not as well characterized; understanding unconventional solvation regimes could improve our knowledge of these systems with regard to their applications in organic electronics. One way to self-assemble PDIs to explore these regimes is by binding them to the walls of the nanoscopic pores in an anodic aluminum oxide (AAO) membrane. By using a silatrane group attachment strategy on a metal oxide surface, Brennan, *et al*., anchored a tetra-arylporphyrin dye onto mesoporous $TiO_2$ incorporated in a dye-sensitized solar cell.[68] This binding method can be extended to AAO membranes, and has been used to control the orientation of photogenerated spin-correlated radical pairs in covalent donor-acceptor molecules at room temperature.[36]

Creating a system with PDI covalently attached to the walls of the pores of an AAO membrane allows us to probe chromophore orientation as well as CT and exciton trapping in these aggregates. An advantage of using AAO membrane assemblies is the ability to fill the pores with a wide range

of solvents without regard to the solubility of the PDIs adsorbed or covalently bound to the AAO membrane, allowing the interactions between the PDIs and the solvent to be tuned over an arbitrary range of solvent polarities. The AAO assemblies studied here are measured in air (with a static dielectric constant ε = 1.0), toluene (ε = 2.38), dichloromethane (ε = 8.93), and water (ε = 80.1). This series of solvents provides a wide range of polarities to observe the effects of changing dielectric constant on the degree of CT character. This approach allows us to observe the degree of CT character in the PDI excimers as they are modulated by different dielectric environments.

## 2.2 RESULTS AND DISCUSSION

### 2.2.1 Synthetic Route

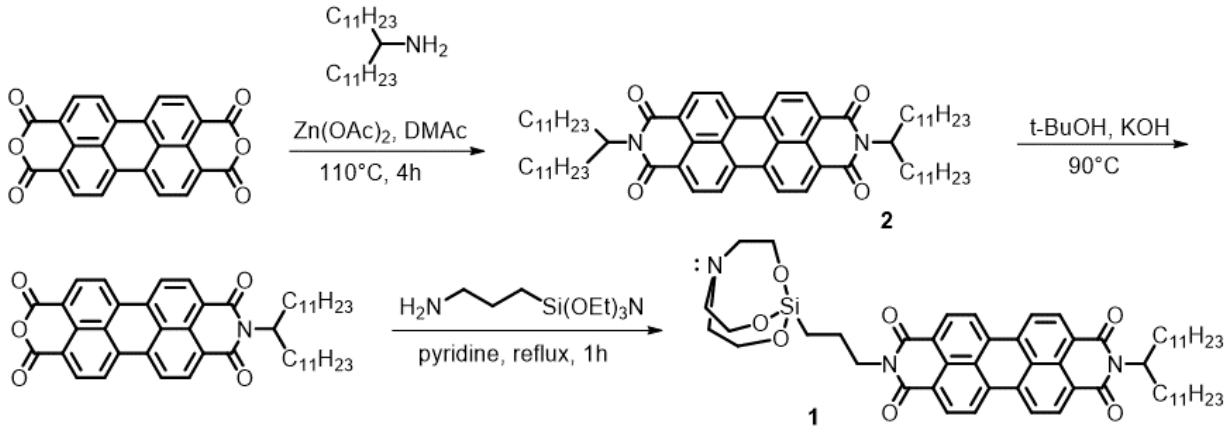


**Figure 2.1.** Synthesis for the PDI series investigated here.

Perylene dianhydride was purchased from Sigma-Aldrich and used without further purification. 12-tricosanylamine was synthesized following literature methods.[69] Details for the synthesis of the asymmetric PDI silatrane (**1**) can be found in the Supporting Information (SI, Section 2.4), while the symmetric PDI (**2**) with 12-tricosanyl tails was synthesized as previously reported (Figure 2.1).[70] Aminopropyl silatrane ($Si(OEt)_3N_2C_3H_8$) was also synthesized using published methods.[71] Intermediates and final products were characterized via $^1H$ NMR and high resolution mass spectrometry (ESI-MS). Details of the characterization can be found in the SI (Section 2.4).

### 2.2.1 Steady State Spectral Measurements

A detailed description of the synthesis and assembly of PDI derivatives on the AAO membranes is given in the Supporting Information. The steady-state absorption and emission spectra of PDI derivatives **1** and **2** in DCM solution and incorporated into AAO membranes are shown in Figure 1. The solution spectra are characteristic of monomeric PDI.[72] The Franck-Condon vibronic bands are well-defined in the solution absorption spectra (Figure 2.2a), while the vibronic progression is perturbed when attached to AAO (Figure 2.2c). Enhancement of the 490 nm band (0-1 transition) relative to the 525 nm band (0-0 transition) in **1** is due to excitonic coupling of PDI transition dipole moments (*H*-aggregation) when **1** is stacked in the AAO membrane,[65] indicating proximal binding of the PDI units to the membrane pore walls. The AAO system with **2** intercalated in the AAO having *n*-octadecylsilane chains covalently attached to the pore walls has absorption maxima at 524 nm and 499 nm, and also exhibits increased relative absorbance of the 0-1 to 0-0 transition. The spectrum of **2** in the AAO membrane is also significantly broadened relative to that **1** in the AAO membrane. This spectral broadening observed in **2** relative to that in **1** may result from increased disorder in the assemblies of **2**, which is not covalently bound to the AAO membrane wall. Unnormalized UV-Vis spectra (Figure 2.13) show that **2**/AAO has twice the absorption amplitude of **1**/AAO in DCM, which suggests the PDIs are more densely packed in the intercalated system. This denser packing may contribute to the higher disorder that leads to spectral broadening in the steady state absorption of **2**/AAO.

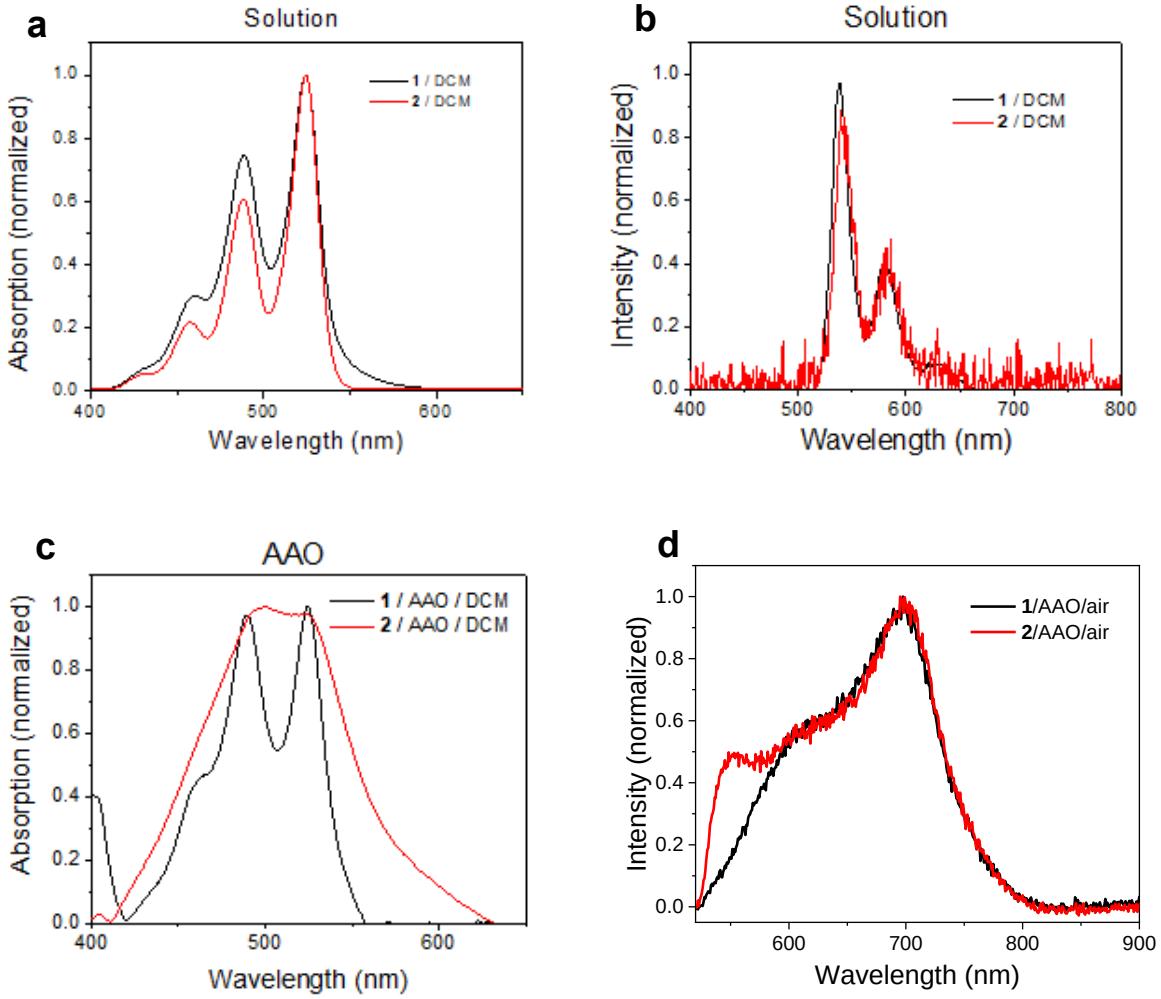


**Figure 2.2.** (a) UV-Vis spectra and (b) fluorescence spectra of PDI derivatives 1 and 2 in DCM solution. (c) UV-Vis spectra and (d) fluorescence spectra of 1 and 2 in AAO membranes.

The fluorescence spectra of **1** and **2** in solution are characteristic of monomeric PDI.[72] Upon the incorporation of **1** and **2** into the AAO membrane by covalent attachment or intercalation, the emission spectra broaden and redshift to 698 nm. These features are suggestive of excimer formation similar to that seen in other PDI aggregates.[73] The steady-state optical data are summarized in Table 2.1.

The loading of octadecyltriethoxysilane onto the AAO membrane walls was characterized by FTIR spectroscopy (Figure 2.11). The presence of the ~3000 $cm^{-1}$ stretch in the FTIR spectrum

of functionalized AAO confirms the attachment of lipid to the AAO wall because this stretch is absent in the spectrum of blank AAO and is characteristic of the octadecyltriethoxysilane solution spectra.

**Table 2.1.** Steady-state spectral data in DCM at 298 K.

| Compound | $\lambda_{max,abs}$ (nm) | $\lambda_{max,ems}$ (nm) | 0-1/0-0 transition intensity ratio |
|---|---|---|---|
| **1** | 524 | 537 | 0.76 |
| **2** | 524 | 539 | 0.64 |
| **1 on AAO** | 524 | 698 | 0.97 |
| **2 on AAO** | 499 | 698 | 1.02 |

### 2.2.2 Transient Absorption Spectroscopy

The excited-state dynamics of **1** and **2** were characterized by femtosecond transient absorption (fsTA) spectroscopy. The fsTA spectra of monomeric PDI derivatives **1** and **2** in DCM solution exhibit typical ground-state bleaching from 445 to 530 nm and stimulated emission from 530 to

640 nm (Figure 2.14). The excited-state absorption extends from 630 to 765 nm and appears as a sharp band that decays to the ground state over the course of the 8 ns pump-probe delay window.

The transient absorption spectra of **1** covalently attached to the AAO membrane pore walls are shown in Figure 2.3, where the pores are filled with $H_2O$, DCM, toluene and air. The fsTA

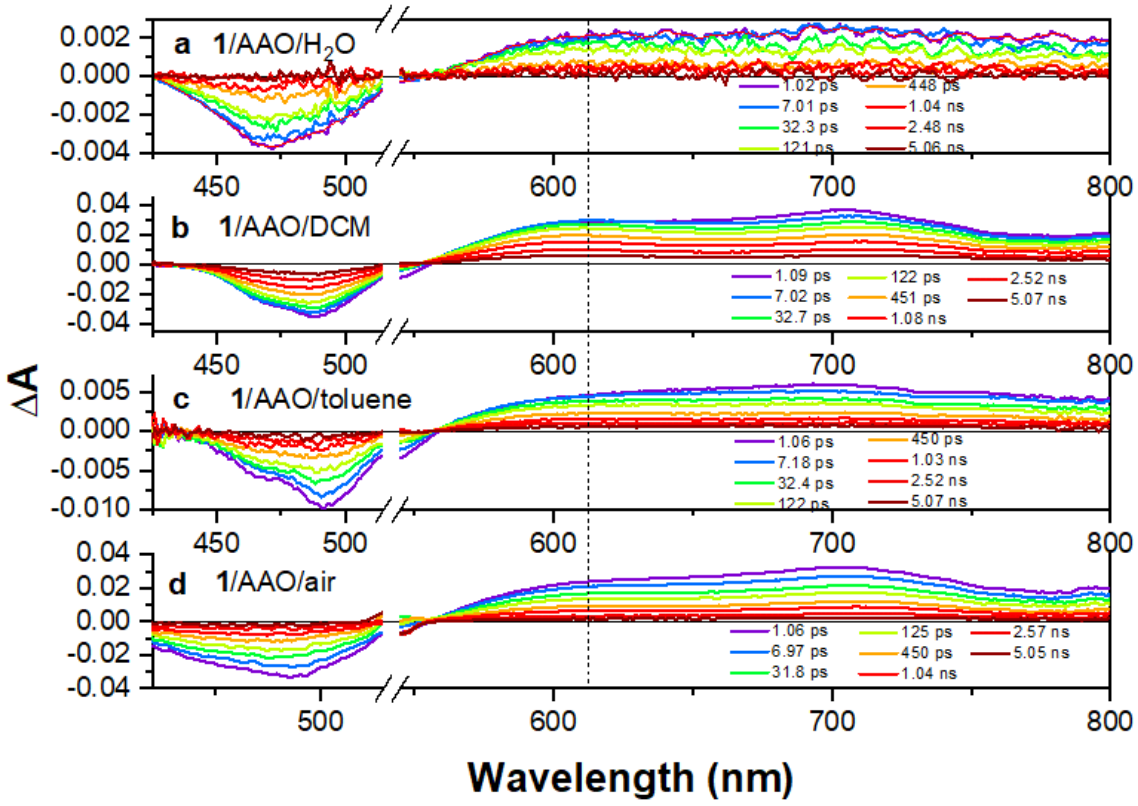


**Figure 2.3.** FsTA spectra at the indicated times of PDI 1 covalently bound to an AAO membrane with its pores containing a) $H_2O$, b) DCM, c) toluene, and d) air. The oscillations in the spectra of 1/AAO/$H_2O$ (a) result from interference effects from the regular array of AAO pores.

data show that the broadened excimer absorption features from 550-775 nm[20] appear shortly after excitation, implying that excimer formation is generally ultrafast in these systems, occurring within a few ps. Notably, very little stimulated emission is observed in the 550-630 nm range; however, this portion of the spectrum undergoes significant evolution in the first few ps (*vide infra*), suggesting that there may be some contribution at early times from the local excited state

prior to excimer formation. A broad absorption band centered at about 700 nm appears immediately upon photoexcitation and loses the peak definition over the first few ps. Spectral broadening is a general consequence of aggregation, however the shape of the spectrum after ~10 ps is characteristic of PDI excimer.[20] The PDIs within the AAO membrane have sufficient π-π overlap in the ground state to allow the photogenerated excited state to form an excimer,[74-75] so such a process is expected.

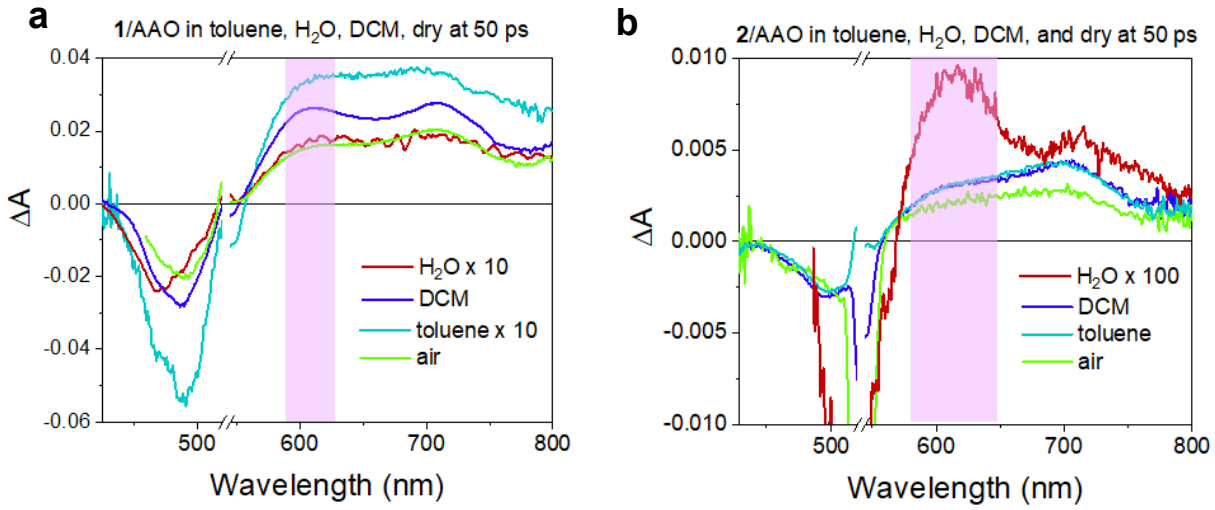


**Figure 2.4.** FsTA spectra at 50 ps of (a) PDI silatrane 1 covalently attached to the AAO membrane, and (b) PDI 2 intercalated into the silylated AAO membrane. The AAO membrane pores contain the indicated solvents. The cation band at 610 nm is highlighted.

A second feature at 610 nm also appears, which is illustrated in the expanded spectra presented in Figure 2.4a and 2.4b, and is most pronounced for **1**/AAO and **2**/AAO having DCM and $H_2O$ in the pores, respectively. This feature redshifts to 616 nm for **1**/AAO/air compared to **1**/AAO in other solvents and is less distinct in the fsTA spectra of the **1**/AAO/toluene. The sharpening of the feature between 600 and 620 nm as the solvent polarity increases suggests that this band correlates with CT character within the PDI assembly,[20, 23, 74] and is likely due to absorption by the PDI radical cation.[76]

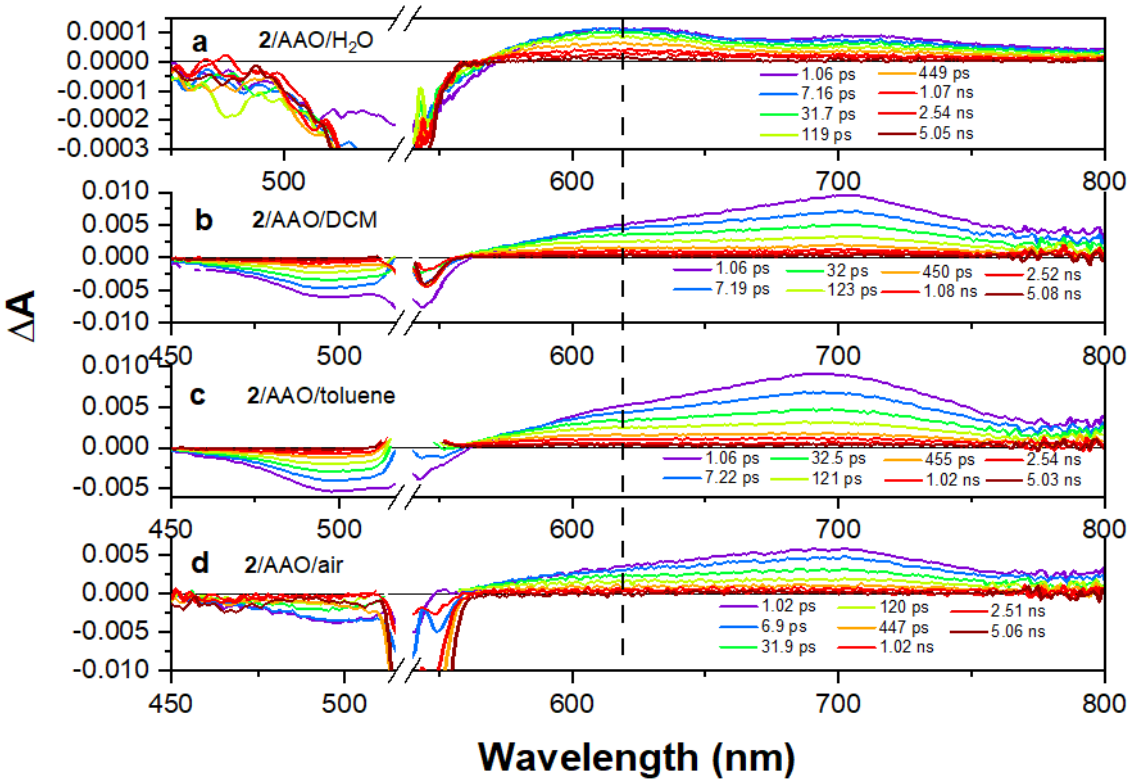


**Figure 2.5.** FsTA spectra of 2 at the indicated times intercalated in the silylated AAO membrane with its pores containing a) water, b) DCM, c) toluene, and d) air.

In the **1**/AAO system, the broad excited-state absorption maximum at later times appears as two absorption bands at 608 and 707 nm, which are more prominent in **1**/AAO/DCM and $H_2O$ (Figures 2.3a and 2.3b). As discussed above, the PDI cation has been reported to absorb at ~600 nm,[76] while the anion absorbs between 700-720 nm,[77] so the presence of the absorption bands at 608 and 707 nm are diagnostic for the CT character of the excimer, though this will be accompanied by the Frenkel exciton absorption of PDI around 700 nm as well. The fixed silatrane length may enforce *H*-type aggregation, which is consistent with the observed steady-state absorption spectrum. These two absorption bands are less distinct in **1**/AAO/toluene, which may be a consequence of a diminished contribution from CT states to the PDI excimer state. As

discussed above, these charge-resonance states are stabilized by high dielectric solvents. The energy of the CT state dictated by the environment changes the relative contributions to the quantum mechanical admixture that describes the excimer,[23] with more CT character accessible in higher dielectric constant solvents. Previously, transitions in the visible region from excimer to CT-like states have been detected and their band shape analyzed.[76, 78-79] Thus, the presence of the 608 nm and 707 nm support the presence of significant CT character in **1** when the AAO pores are filled with polar solvents.

The excited-state dynamics of **2** intercalated into the silylated AAO membranes ($\lambda_{ex}$ = 534 nm) were probed in the same solvents as **1** (Figure 2.5). Similar positive features at about 610 and 700 nm are observed for **2** compared to those in **1** (Figure 2.4b). The depressed relative intensity below 700 nm at early times may reflect the contribution from stimulated emission from the local excited state of PDI prior to excimer formation. This most likely results from a slowed rate of excimer formation (*vide infra*), at least for some of the pores. Notably, for **2** in AAO membranes containing $H_2O$ in their pores, the 610 nm band is very prominent, once again suggesting that this band likely derives from a CT state.

The transient absorption data were fitted to a sum-of-three exponentials in a decay-associated model (Figures 2.15-2.18) to describe simply and account for the disorder in the AAO system. Importantly, because of this disorder, we expect many different relative chromophore spacings and orientations to be present in the probe volume, leading to a distribution of rates with the observed values being the most strongly represented, i.e. the modes of the distribution. Nonetheless, multiphasic evolution in excimers has been previously proposed[80] wherein the initial excimer undergoes a structural change in intermolecular packing to better accommodate the

excited state before ultimately decaying. Given the span of rates extracted, we will discuss the dynamics in this context.

In **1**/AAO/$H_2O$, a short 2.6 ± 0.3 ps component is observed (Figure 2.6d), which has characteristics of $^{1*}$PDI, particularly the negative features below 600 nm. The other species live for 160 ± 20 ps and 1.8 ± 0.2 ns with similar decay-associated spectra. The 160 ps component likely represents some average geometric reorientation in the excimer state, which then forms the 1.8 ns relaxed excimer. Both components capture the absorption near 610 nm, indicating that the dynamics are associated with excimers of high CT character. The longer time constant is assigned to the lifetime of the excimer, which is significantly shorter than the monomeric $^{1*}$PDI lifetime of ~3 ns. While PDI excimers typically have lifetimes longer than 10 ns, previous studies have shown that strongly coupled excimers can have lifetimes shorter than the monomer.[20]

In moderate polarity DCM, the dynamics are similar, though the timescales change somewhat. The shortest component in **1**/AAO/DCM is 2.3 ± 0.1 ps and its spectrum again resembles the transient absorption spectrum of $^{1}$*PDI, suggesting that this is the timescale for excimer formation in this system, comparable to that in $H_2O$. The same structural relaxation observed in **1**/AAO/$H_2O$ is slightly slowed to 204 ± 5 ps, however the degree of stabilization appears higher compared to that observed in $H_2O$, as the longest-lived component exhibits a very prominent PDI cation absorption at 610 nm.. The higher degree of stabilization may be due to better solvation of the PDI by DCM compared to water. The π-stacking between the PDI units may be disrupted to a weak extent by the DCM which could penetrate between the edges or ends chromophores leading to a weaker excimer coupling. The 4.09 ± 0.05 ns species excimer lifetime is closer to that of $^{1*}$PDI in solution, which may also be a result of such better solvation and weaker coupling.

In toluene, the dynamics are mostly faster than in either water or DCM. The initial excimer formation occurs with a 0.9 ± 0.3 ps time constant, followed by 58 ± 2 ps and 2.32 ± 0.05 ns decays. The latter two components have similar spectra, though again the longer-lived component appears to have more CT character, which suggests the intermediate process is relaxation of the system to better accommodate the charge resonance states. The 2.3 ns excimer lifetime is again shorter than the monomer.

In the absence of a solvent, the PDI units are self-solvated and spectrally more closely resemble **1**/AAO/$H_2O$ than in other solvents, despite the largest difference in dielectric constants. This can be attributed to the lack of solvation in water, particularly between the PDI π-surfaces that is likely present in both DCM and toluene. Dynamically, excimer formation is faster in air than in other solvents, as there is no component resembling $^{1*}$PDI apparent in the analysis; the only stabilizing interaction present is between chromophores, leading to apparent optimal coupling for excimer formation. The 8 ps and 310 ps components are assigned to relaxation on the basis of their spectral shapes before decaying in 3.5 ns. As discussed above, theoretical studies show that while excimer formation may be ideal at one geometry, the adiabatic geometry of the excimer itself may be quite different, requiring relaxation along multiple coordinates, leading to the observed relaxation components in the TA data.

In the intercalated **2**/AAO systems we observe similar three-state decay dynamics. In **2**/AAO/$H_2O$, $^{1*}$PDI undergoes sub-picosecond excimer formation before relaxing in 122 ps and

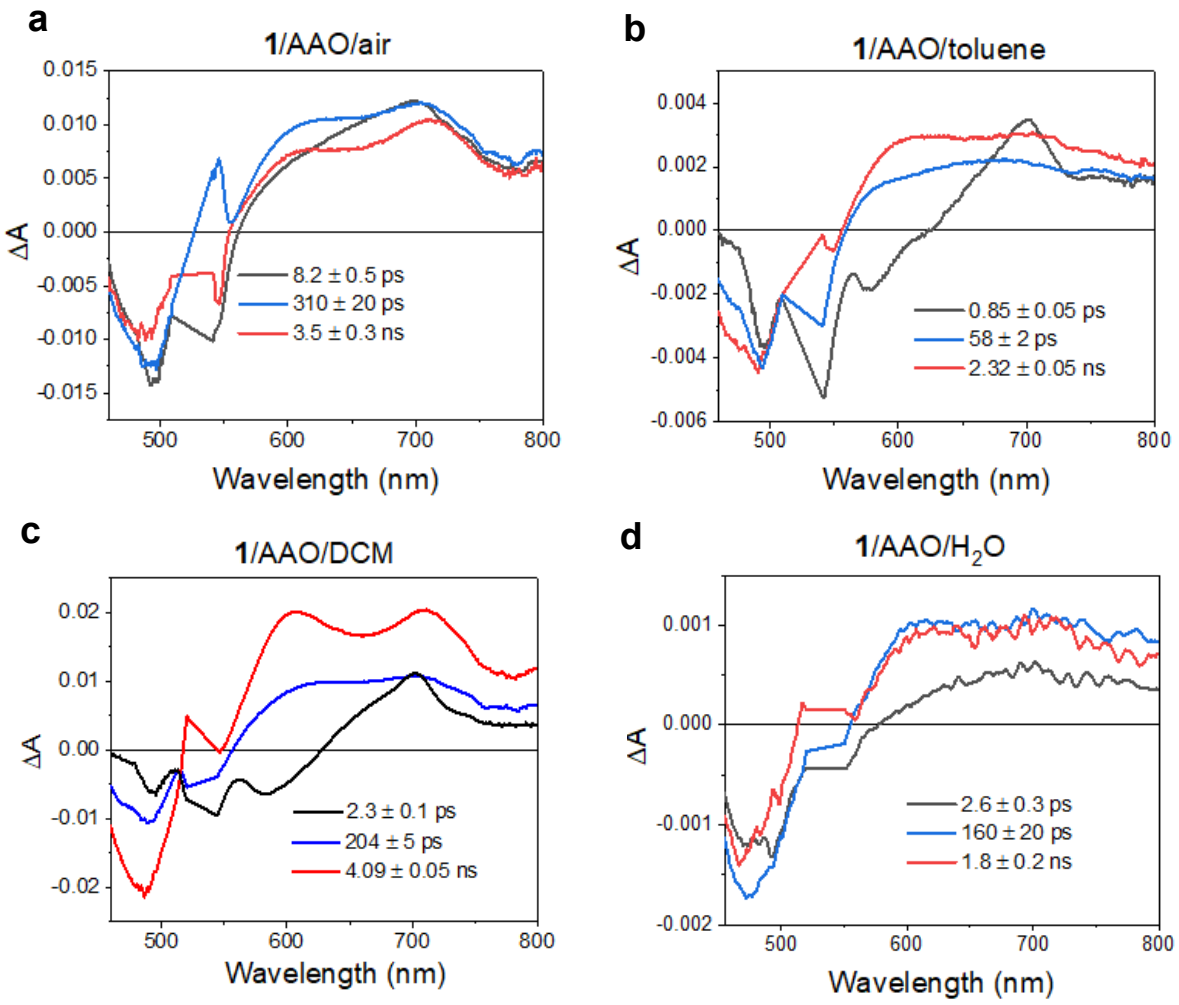


**Figure 2.6.** Decay-associated spectra for 1/AAO in (a) air, (b) toluene, (c) DCM, and (d) $H_2O$.

ultimately decaying in 2.4 ns (Figure 2.7d). Poor solvation by the water molecules is again the likely origin of the strong π-overlap necessary for rapid excimer formation. The drastic increase in the intensity of the 610 nm cation band is again attributed to stabilization of the charge resonance states by the high polarity water environment.

**2**/AAO/DCM exhibits excimer formation time of 2.9 ± 0.1 ps, which is followed by a ~60 ps relaxation with a decay-associated spectrum showing no stimulated emission but only a weak absorption near 600 nm accompanied by a relatively strong absorption near 700 nm. Since $^{1*}$PDI

absorbs strongly at 700 nm, the presence of this prominent band in the decay-associated spectrum may indicate an intermediate excimer composition which has strong Frenkel exciton character or may be capturing some slower excimer formation. The longer-lived 1.32 ns component features a more intense band at 610 nm associated with higher CT character, implying that this component represents the fully relaxed excimer decay. The excimer in **2**/AAO/DCM forms in 2.9 ± 0.1 ps. Since **2** is highly soluble in DCM, it would be expected that the solvent could disrupt π-stacking in this system and slow its formation. Additionally, the excimer decay is faster than the analogous process in **1**, which suggests it is an effect of the higher conformational and overlap freedom available to the intercalated **2** compared to the covalently linked **1**. The higher loading efficiency of PDIs in **2** compared to **1** (indicated by Figure 2.13) likely contributes to faster excimer decay in **2** because the greater number of PDIs in the probe volume also increases conformational freedom.

In toluene, **2**/AAO undergoes slower excimer formation, with a time constant of 4.4 ± 0.3 ps followed by relaxation to a higher CT character excimer in 83 ps that then decays in 1.8 ns. The formation and relaxation times are slower than in **1**/AAO/toluene, and the degree of CT character overall appears lower.

Finally, in **2**/AAO/air, we observe an excimer formation time of 1.3 ps, broadened but still recognizable features of $^{1*}$PDI decaying in that time. The other component spectra decay with 130 ps and 1.5 ns with similar spectra. The fast excimer formation time is in stark contrast to that of **1**/AAO/air where the slowest formation time was observed. Presumably both systems are affected by the lack of solvent which may force the PDIs to solvate themselves, as discussed above. However, in **2**/AAO the octadecyltriethoxysilane coating the walls of the AAO may be acting as a low-polarity "solvent" (ε ~ 2) in the absence of a bulk dielectric environment, which could lead to more aggregate-like behavior, with on-average stronger coupling leading to faster excimer

formation times. This pronounced aggregate-like behavior in **2** is also a result of the higher loading ratio of PDI on **2** compared to **1**.

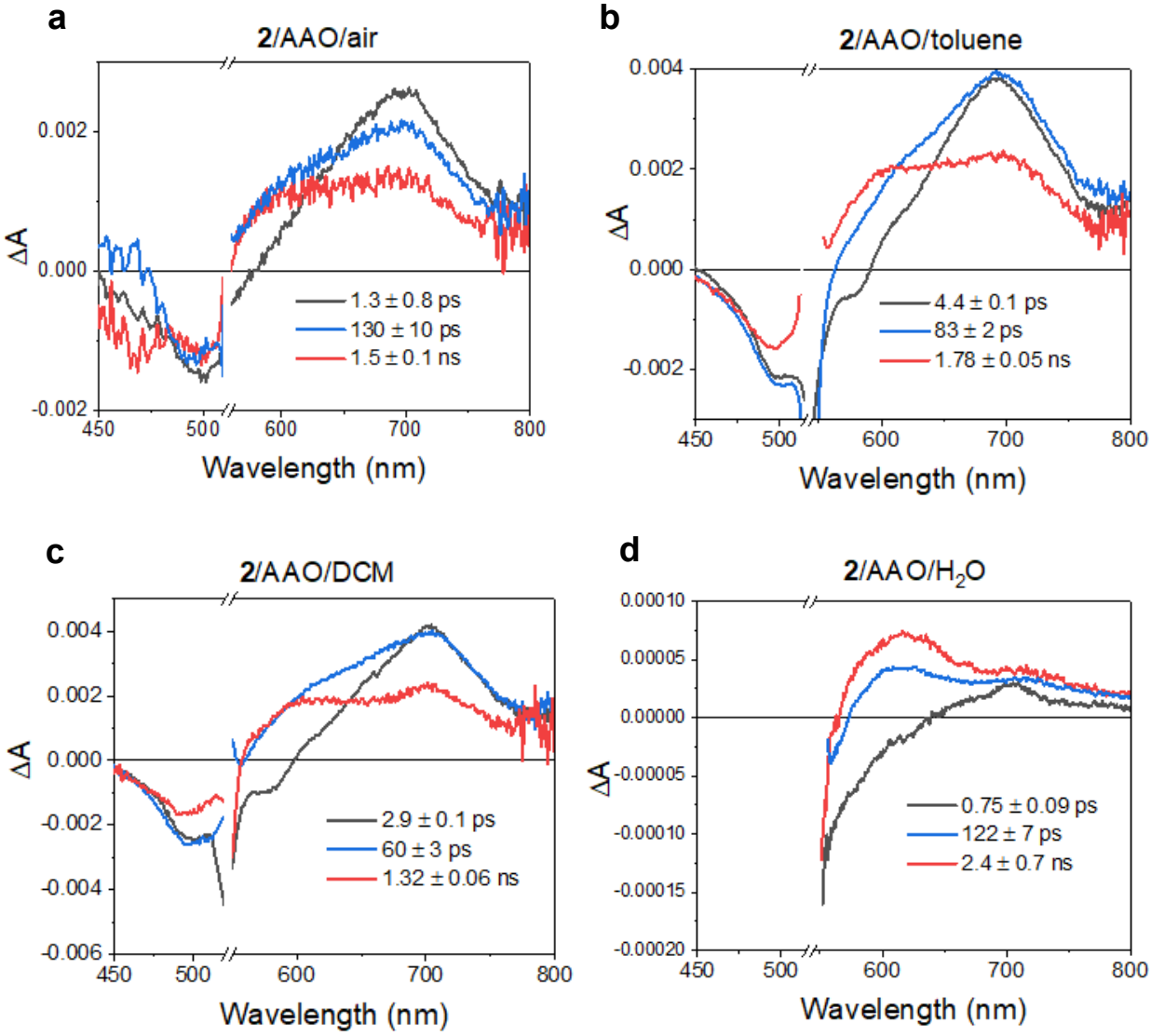


**Figure 2.7.** Decay-associated spectra for 2/AAO in (a) air, (b) toluene, (c) DCM, and (d) $H_2O$. Data between 550-570 nm for (a-c) and below 550 nm (d) are obscured by pump scatter and are omitted.

Generally, the excimer lifetimes in **2** are shorter than those observed in **1**. The bands attributed to charge-resonance character in system **1** are somewhat less prominent in **2**, except when $H_2O$ is present, indicating that the positions of the PDIs relative to one another when intercalated in the lipid-coated AAO walls may in general be larger causing the excimers have a higher relative

contributions from the Frenkel exciton state. This is attributed to the steric interactions between the 12-tricosanyl groups on the PDIs, which causes the torsional angle φ between N-N axes of cofacial PDIs to be somewhat larger than 0°. The fixed length of the silatrane in **1** encourages *H*-aggregation and increased order, while intercalation of **2** into the silylated AAO membrane nanopore walls leads to more inter-PDI conformational freedom. This may allow **2** to be fully stabilized in the ground state at φ ≈ 30° relative to its neighboring PDI molecules, according to theory.[20, 73] The intercalation method in **2** allows a greater number of interchromophore orientations because of the flexibility of the tails and lipid on the AAO wall; this flexibility gives rise to greater conformational and overlap freedom of the PDIs, as represented in Figure 2.8. The steric demands of the PDI 12-tricosanyl groups may also inhibit the PDI excimers from achieving their optimal conformations. The generally slower excimer formation times observed here relative to those in covalent dimers is likely a consequence of this conformational freedom, where relatively few PDIs are in an optimized configuration in equilibrium. Similarly, the PDIs in the AAO membrane may require greater geometric rearrangement to optimize their electronic interactions compared to dimers.

| | | $\tau_1$ | $\tau_2$ | $\tau_3$ |
|---|---|---|---|---|
| 1/AAO | air | 8.2 ± 0.5 ps | 310 ± 20 ps | 3.5 ± 0.3 ns |
| | toluene | 0.85 ± 0.05 ps | 58 ± 2 ps | 2.32 ± 0.05 ns |
| | DCM | 2.3 ± 0.1 ps | 204 ± 5 ps | 4.09 ± 0.05 ns |
| | $H_2O$ | 2.6 ± 0.3 ps | 160 ± 20 ps | 1.8 ± 0.2 ns |
| 2/AAO | air | 1.3 ± 0.8 ps | 130 ± 10 ps | 1.5 ± 0.1 ns |
| | toluene | 4.4 ± 0.1 ps | 83 ± 2 ps | 1.78 ± 0.05 ns |
| | DCM | 2.9 ± 0.1 ps | 60 ± 3 ps | 1.32 ± 0.06 ns |
| | $H_2O$ | 0.75 ± 0.09 ps | 122 ± 7 ps | 2.4 ± 0.7 ps |

**Table 2.2.** Comparison of fsTA time constants of kinetic species for 1/AAO and 2/AAO in air, toluene, DCM, and H,O.

The overall shorter excimer lifetimes in both **1** and **2** compared to typical PDI excimers in dimers may be a consequence of the higher flexibility and conformational freedom afforded by the AAOs, enhancing the rate of internal conversion and lowering the excimer lifetime; this is likely exacerbated in **2** by the interactions of the PDI with the surrounding octadecyltriethoxysilane chains and the closer packing of PDIs in **2** due to the higher loading efficiency.

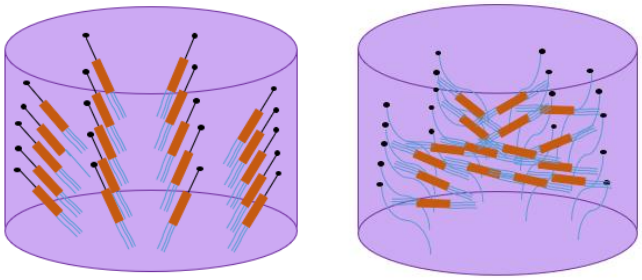

**Figure 2.8.** Left: Depiction of 1/AAO with PDIs arranged as *H*-aggregates and of Right: 2/AAO with PDIs intercalated in lipid and aggregated in numerous orientations.

While the anodization process used to create AAO layers has been improved to produce highly ordered pore structures,[81] the surface loading on the pore walls of **1** and **2** is not necessarily uniform, as seen in scanning electron microscope (SEM) images of the AAO membrane surface

(Figure 2.12). The silatrane has three potential binding sites to the oxide surface and depending on the rate of hydrolysis, the silatrane may bind to one, two, or all three sites. This will affect the orientation of the molecule on the surface and the subsequent binding of other molecules to the surface. Additionally, previous work has shown that molecules bound to the walls of AAO hang at an angle that is not perfectly perpendicular to the surface[36] and this angle may vary based on the proximity of the other surface-bound molecules. One way to improve the binding uniformity is to react the AAO walls with the molecules in the presence of acid to promote faster hydrolysis and higher loadings.[82] Future efforts to control the orientation of molecules on AAO membrane pore walls will include using stimuli-responsive materials covalently attached to an AAO wall that can be aligned using a magnetic field for long-range ordering. Anisotropic PDI mesogens in supramolecular block copolymer structures have been aligned with a magnetic field previously, resulting in monoliths with a singular orientation.[83]

## 2.3 CONCLUSIONS

We have prepared two PDI systems that exhibit excimer formation in aggregates that are assembled inside an AAO membrane. One system is formed by covalent attachment of a PDI silatrane molecule to the walls of the AAO, and the other through intercalation of PDI with long side chains into an AAO coated with lipid. By using steady-state and time-resolved absorption measurements, we observed excimer formation and subsequent relaxation and decay of PDI molecules closely arranged on the surface of the AAO membrane pore walls. Increased charge transfer character occurs with higher dielectric constant solvents for the covalently attached PDI system. These results show that AAO membranes are useful tools to self-assemble chromophores and understand the role of exciton trapping in a system that has characteristics in the intermediate regime between the solution and solid state.

## 2.4 SUPPLEMENTARY INFORMATION

### 2.4.1 Synthesis

$^1$H nuclear magnetic resonance spectra were collected on a Bruker Avance III 500 MHz system and chemical shifts are recorded in ppm (δ) and samples dissolved in deuterated chloroform. The matrix assisted laser desorption ionization – time of flight (MALDI-ToF) spectra were taken on a Bruker AutoFlex-III. The synthesis of **1** is outlined below.

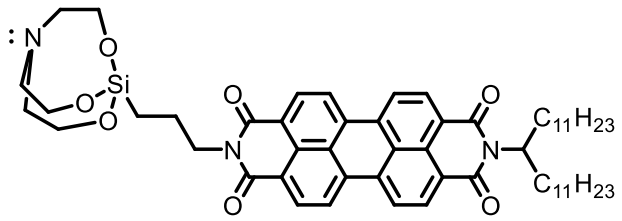


***N*-(12-tricosanyl)perylene-3,4:9,10-tetracarboxy-3,4-[(3-silatranylpropyl)amide]-9,10-imide**

N-(12-tricosanyl)perylene-3,4:9,10-tetracarboxy-3,4-anhydride-9,10-imide (0.44 g, 0.621 mmol) and (3-silatranylpropyl)amide[71] (0.433 g, 1.86 mmol) were dissolved in pyridine and stirred for 1 hour. The solvent was removed by rotary evaporation and the resulting solid dissolved in dichloromethane and purified on a silica gel column using $CHCl_3$ to elute the residual N,N'-bis(12-tricosanyl)perylene-3,4:9,10-bis(dicarboximide). A mixture of $CHCl_3$: acetic acid (9:1) was used to the elute the product. The product was further purified using $^1$H NMR (δ in $CDCl_3$, 500 MHz): 8.63 (m, 8H), 5.18 (m, 1H), 4.21 (t, 2H), 3.74 (t, 6H, $–CH_2–O–$), 2.78 (t, 6H, $–CH_2–N$), 2.25 (m, 2H), 1.86 (m, 2H), 1.47 (m, 2H), 1.12-1.33 (m, 36H), 0.84 (t, 6H), 0.57 (m, 2H). HR-MS (ESI)(m/z): [$M^+$] calc. for $C_{56}H_{73}N_3O_7Si$, 928.30; found, 928.5296.

### 2.4.2 Assembly of PDIs on AAO Membranes

Free-standing anodic aluminum oxide membranes (80 nm pore diameter, 1 cm diameter, 50 μm thickness) were purchased from InRedox. To covalently attach PDI to the surface of the AAO

membrane nanopores, a free-standing AAO membrane with an 80 nm pore diameter was soaked in a 1 mM solution of PDI silatrane in dichloromethane. To intercalate PDI in the AAO nanopores, an AAO membrane was soaked in 1 mM of octadecyltriethoxysilane for 24 hours. This lipid-coated AAO was then soaked in 1 mM solution of symmetric PDI for 24 hours. Both AAO membranes were washed with dichloromethane and methanol and dried prior to making measurements.

### 2.4.3 Steady-State Spectral Measurements

UV-vis spectra of the PDI derivatives were obtained at ambient temperature on a Shimadzu 1800 UV-vis spectrometer in DCM. Fluorescence measurements were obtained using a HORIBA Fluorolog-3 spectrofluorimeter. Fourier transform infrared (FTIR) spectra were acquired on a Shimadzu IRAffinity-1 spectrometer.

### 2.4.4 Femtosecond Transient Absorption (fsTA) Spectroscopy

Femtosecond transient absorption spectroscopy was conducted using a regeneratively amplified Ti:sapphire laser system (Spectra Physics, Spitfire Pro) operated at a 1 kHz repetition rate.[84] Samples were excited at 534 nm in 2 mm (for PDI in solution) and 1 mm (for PDI in AAO membranes) quartz cuvettes, with depolarized 110 fs, 1.0 μJ pulses focused to a 0.5 mm diameter (1/*e*) spot. FsTA measurements were made on sample **2**/AAO/$H_2O$ using a regeneratively amplified Yb:KGW laser system operating at 1040 nm and a 100 kHz repetition rate as previously described.[85] The probe beam on this system was generated by pumping a 5 mm YAG plate to create a continuum spanning 500-800 nm. The optical density at the excitation wavelength was ~0.3. The probe beam in the fsTA experiments was directed parallel to the long directions of the AAO pores, and the 534 nm pump was polarized at magic angle (54.7°) relative to the probe.

### 2.4.5 Time-Resolved Fluorescence (TRF) Spectroscopy.

Time-resolved fluorescence spectroscopy was used to obtain the lifetimes and spectra of the emissive species in AAO membranes with **1** and **2**. The time-resolved fluorescence spectra have similar features to the steady-state fluorescence spectra. Figure 7 shows the decay-associated TRF spectra and kinetics of the systems were excited

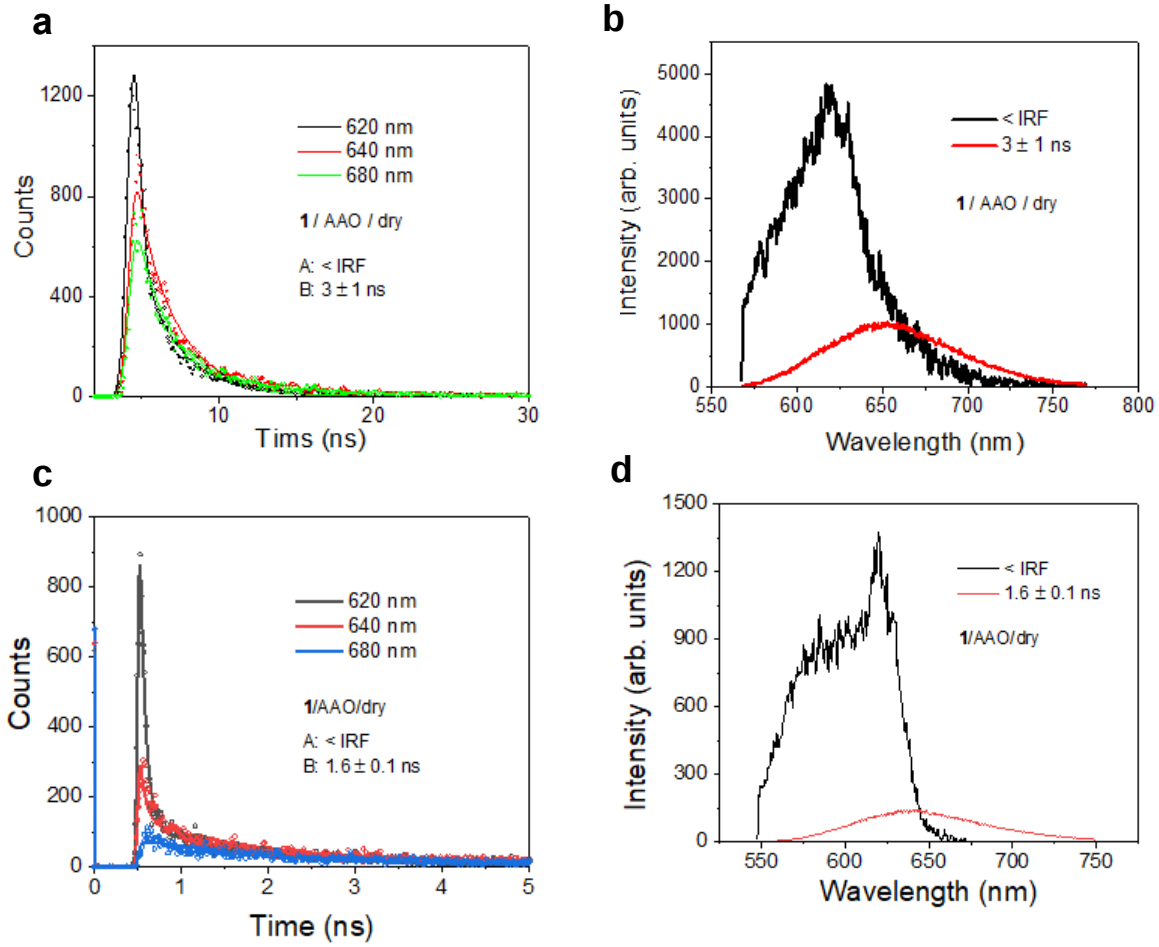


**Figure 2.9.** Time-resolved fluorescence of 1 covalently attached to AAO. Kinetic fits at selected wavelengths for the a) 50 ns time window, and c) 5 ns time window. Decay-associated spectra for the b) 50 ns time window and d) 5 ns time window. IRF is ~2% of time window.

at 510 nm and monitored at 660 nm. In **1** / AAO / dry, we observe a 1.6 ± 0.1 ns process, followed by decay of the emission with a lifetime of 3 ± 1 ns.

TRF data for **2** intercalated in AAO are shown in Figure 8. The fast component is 110 ± 40 ps, while the slow component is 622 ± 200 ps. The emission lifetime of the excimer is markedly shorter than that of **1** covalently attached to the AAO membrane, suggesting the availability of additional decay pathways or an increased rate of internal conversion due to the different interchromophore interactions between PDIs. The shorter lifetime of the excimer in **2** compared to **1** may be due to increased disorder in **2**. The intercalation method in **2** allows a greater number of interchromophore interactions because of the flexibility of the tails and lipid on the AAO wall; this flexibility gives rise to greater conformational and overlap freedom of the PDIs. The relatively small intensity of the excimer fluorescence in both systems shows that the longer component originates from a state that is not highly emissive.

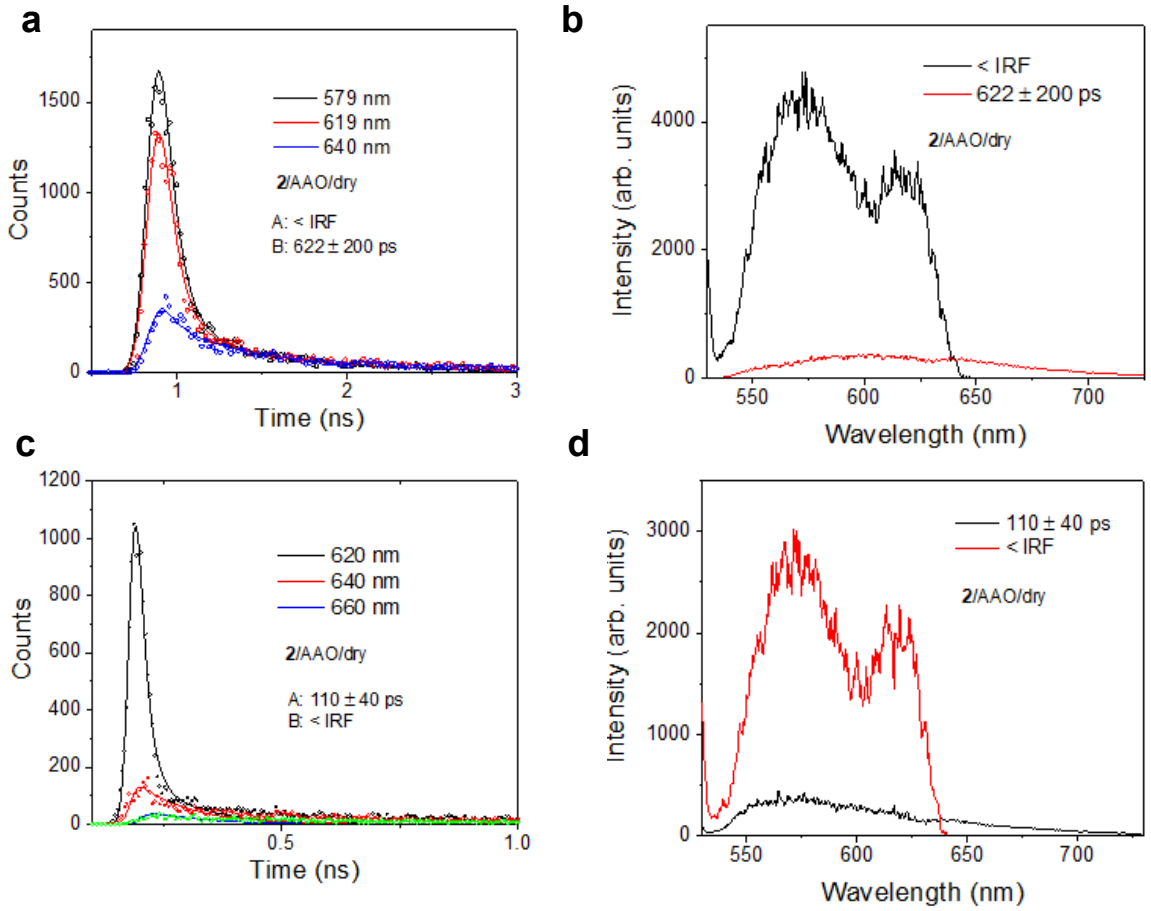


**Figure 2.10.** Time-resolved fluorescence of 2 intercalated in AAO. Kinetic fits at selected wavelengths for the a) 10 ns time window, and c) 2 ns time window. Decay-associated spectra for the b) 10 ns time window and d) 2 ns time window. IRF is ~2% of time window.

### 2.4.6 Kinetic Analysis of fsTA Data

Prior to kinetic analysis, the fsTA data were background/scatter-subtracted and chirp-corrected, and the visible and NIR data sets are spectrally merged (Surface Xplorer 4, Ultrafast Systems, LLC). The data sets of ΔA vs time vs wavelength were subject to global fitting to selected single-wavelength kinetics to yield the kinetic time constants and their decay-associated spectra in MATLAB[86] using lab-written programs.

The time-resolution is given as $w$ = 300 fs (full width at half maximum, FWHM); the assumption of a uniform instrument response across the frequency domain and a fixed time-zero

($t_0$) are implicit in global analysis. Each wavelength was given an initial amplitude that is representative of the spectral intensity at time $t_0$ and varied independently to fit the data. The time/rate constants and $t_0$ are shared between the various kinetic data and are varied globally across the kinetic data to fit the model. We globally fit the dataset to a set of three exponential decays and use the resultant populations to deconvolute the dataset and reconstruct decay-associated spectra. The MATLAB program convolutes the solutions with a Gaussian instrument response function with width *w*, before employing a least-squares fitting using a Levenberg-Marquardt or Simplex method to find the parameters which result in matches to the kinetic data. Each function corresponds to a given population with a well-defined temporal evolution. The raw data matrix is deconvoluted with the resultant populations as functions of time to produce the spectra associated with each mathematical component.

### 2.4.7 Fourier Transform Infrared Spectroscopy characterization of octadecyltriethoxysilane chains on the AAO surface.

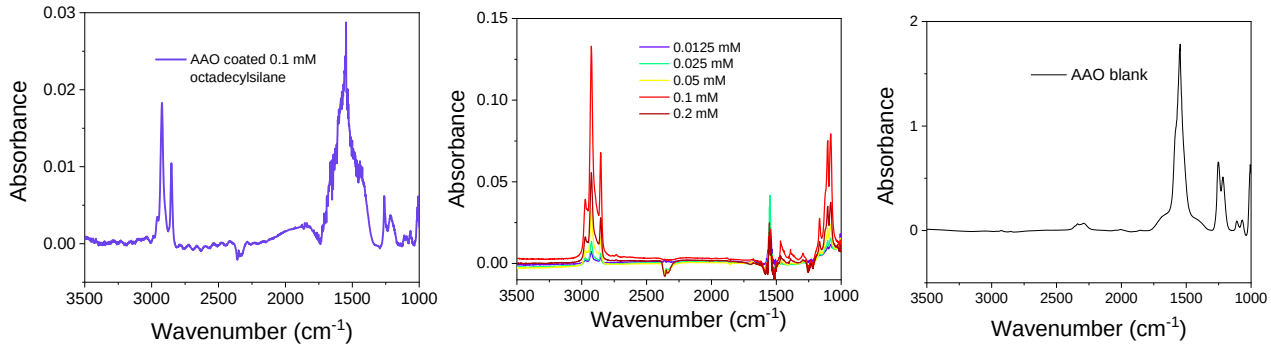


**Figure 2.11.** Left: FTIR spectrum of AAO coated in 0.1 mM of octadecyltriethoxysilane for 24 h. Middle: Concentration study of octadecyltriethoxysilane in carbon tetrachloride ($CCl_4$). Right: FTIR spectrum of uncoated AAO which exhibits no stretch at ~3000 $cm^{-1}$.

### 2.4.8 Scanning Electron Microscopy Images of Anodic Aluminum Oxide Membrane

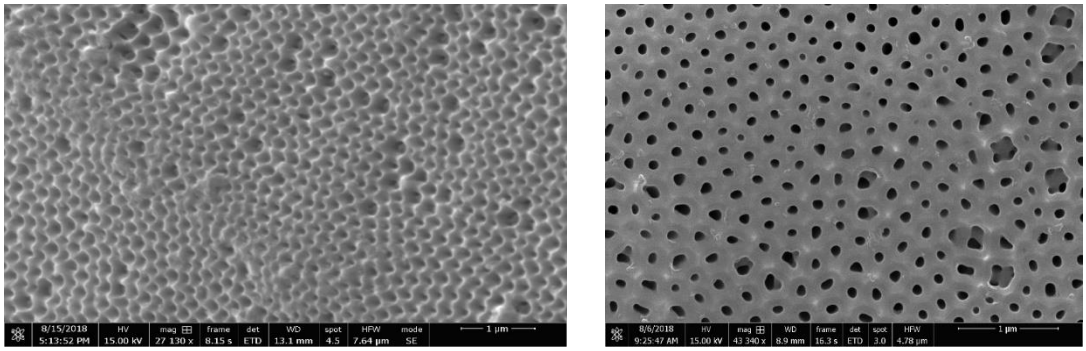

**Figure 2.12.** Left: Scanning electron microscope (SEM) image of the edge of an AAO membrane. Right: SEM image of the top of an AAO membrane.

### 2.4.9 Additional Steady-State Absorption Spectroscopy

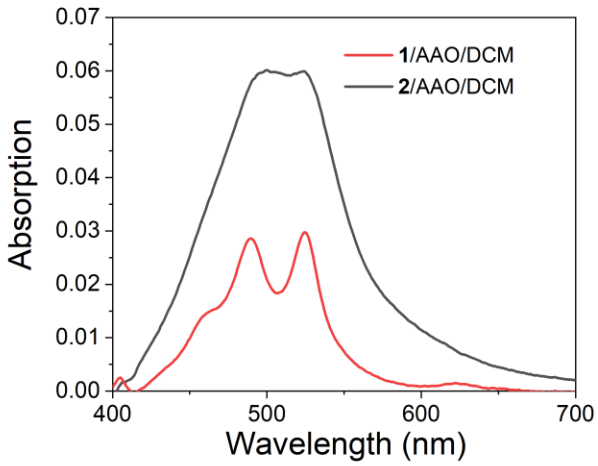


**Figure 2.13.** Unnormalized UV-Vis spectra of 1/AAO/DCM and 2/AAO/DCM.

### 2.4.10 Additional Transient Absorption Spectroscopy

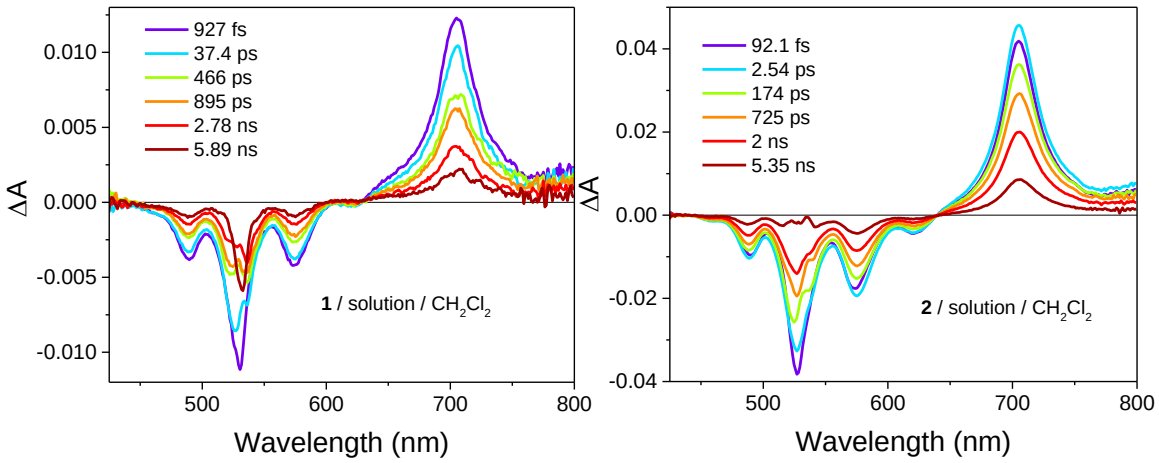


**Figure 2.14.** TA spectra for a solution of 1 (left) and 2 (right) in DCM acquired with $\lambda_{ex}$ = 534 nm, ~110 fs pulses.

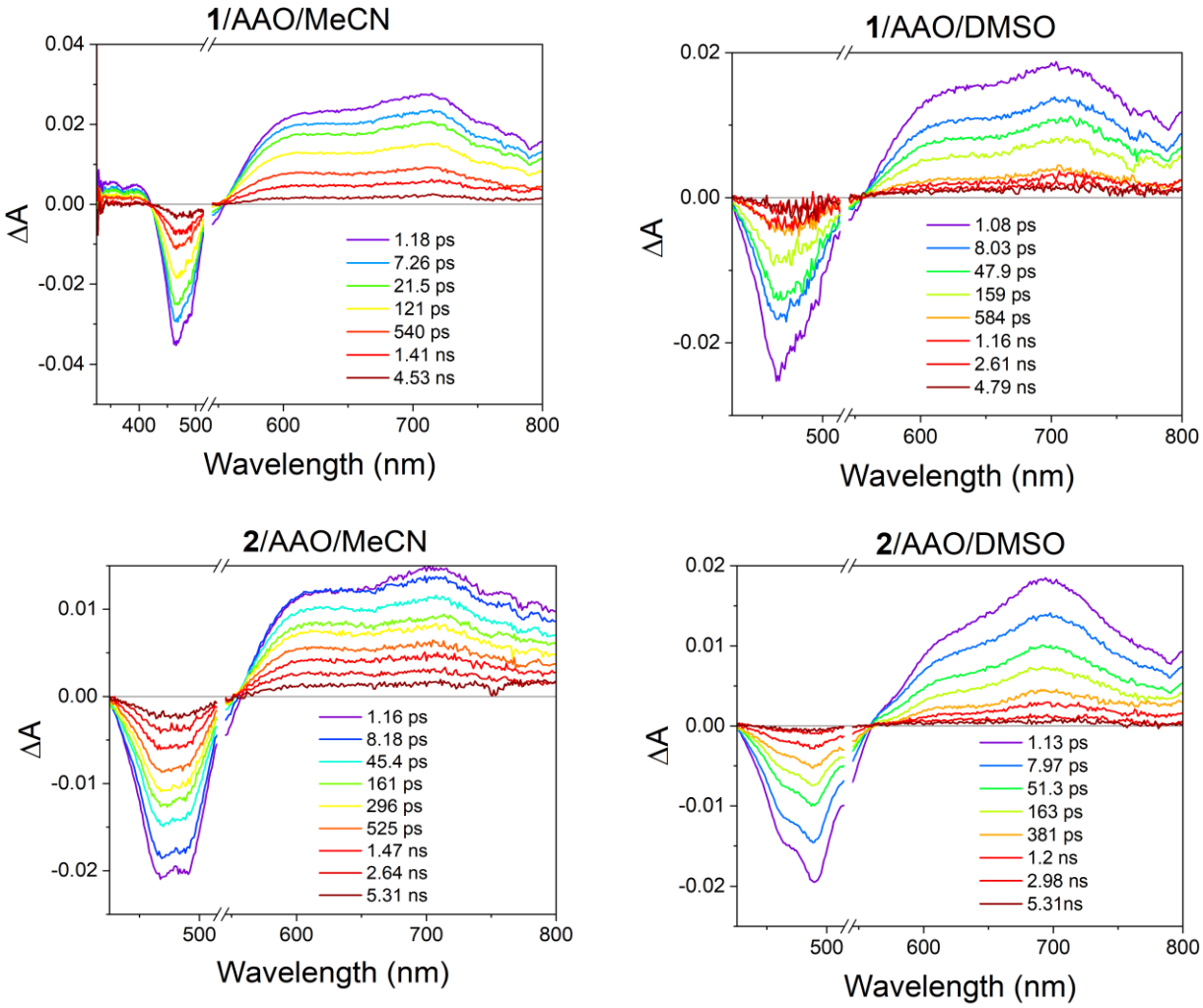


**Figure 2.15.** TA spectra for 1/AAO and 2/AAO in MeCN and DMSO.

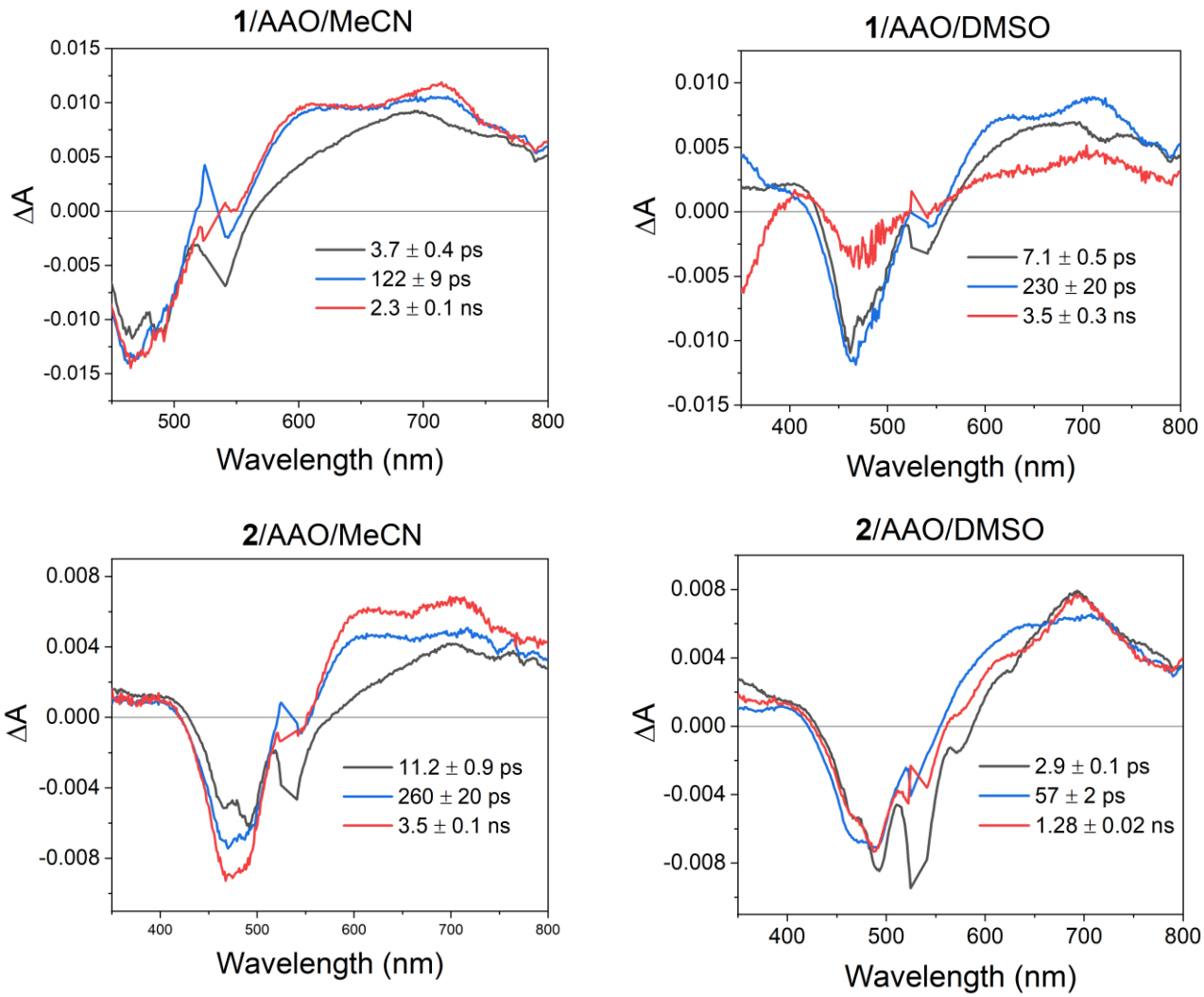


**Figure 2.16.** Decay-associated spectra for 1/AAO and 2/AAO in MeCN and DMSO.

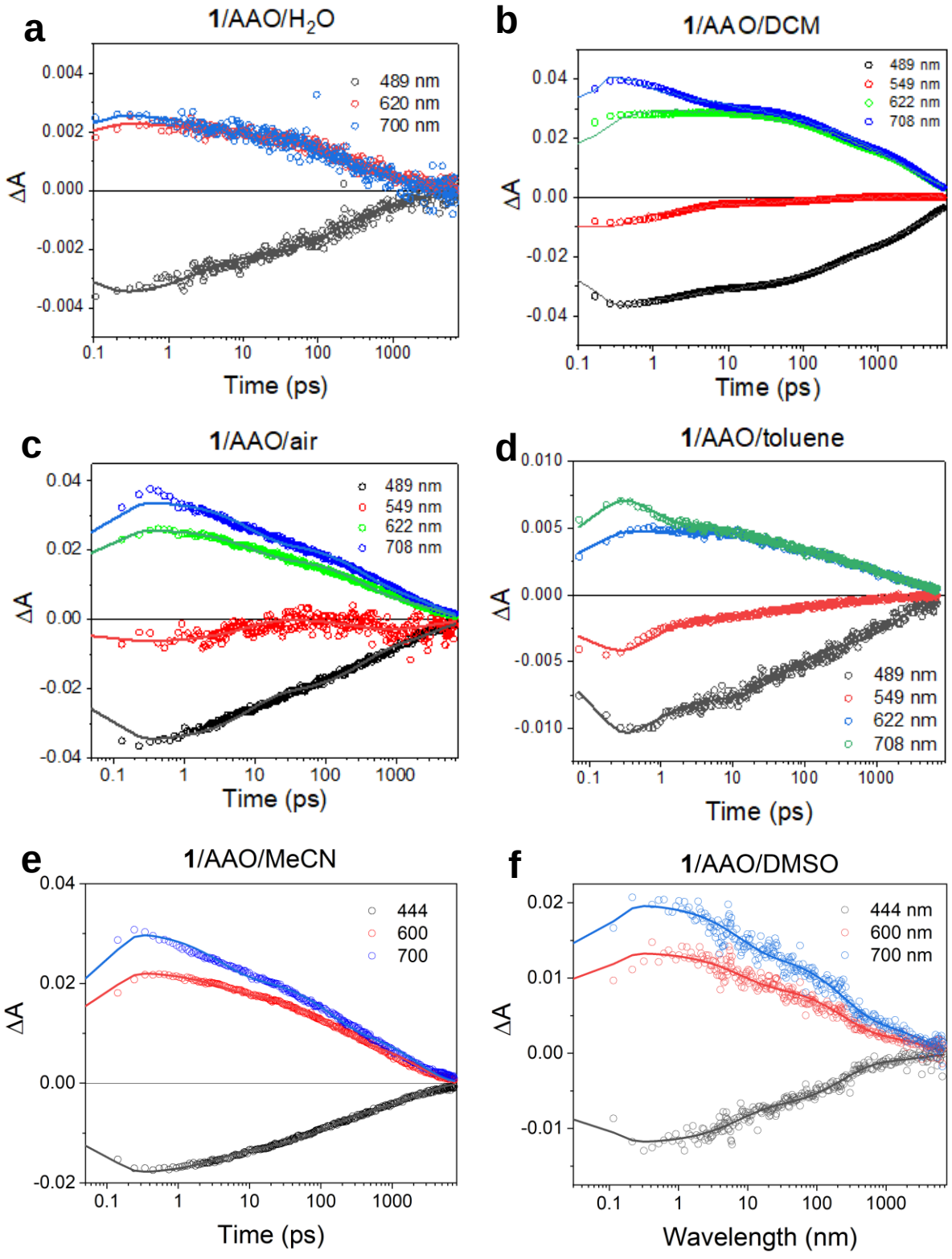


**Figure 2.17.** Kinetic fits for 1/AAO. (DCM = $CH_2Cl_2$; MeCN = acetonitrile; DMSO = dimethylsulfoxide)

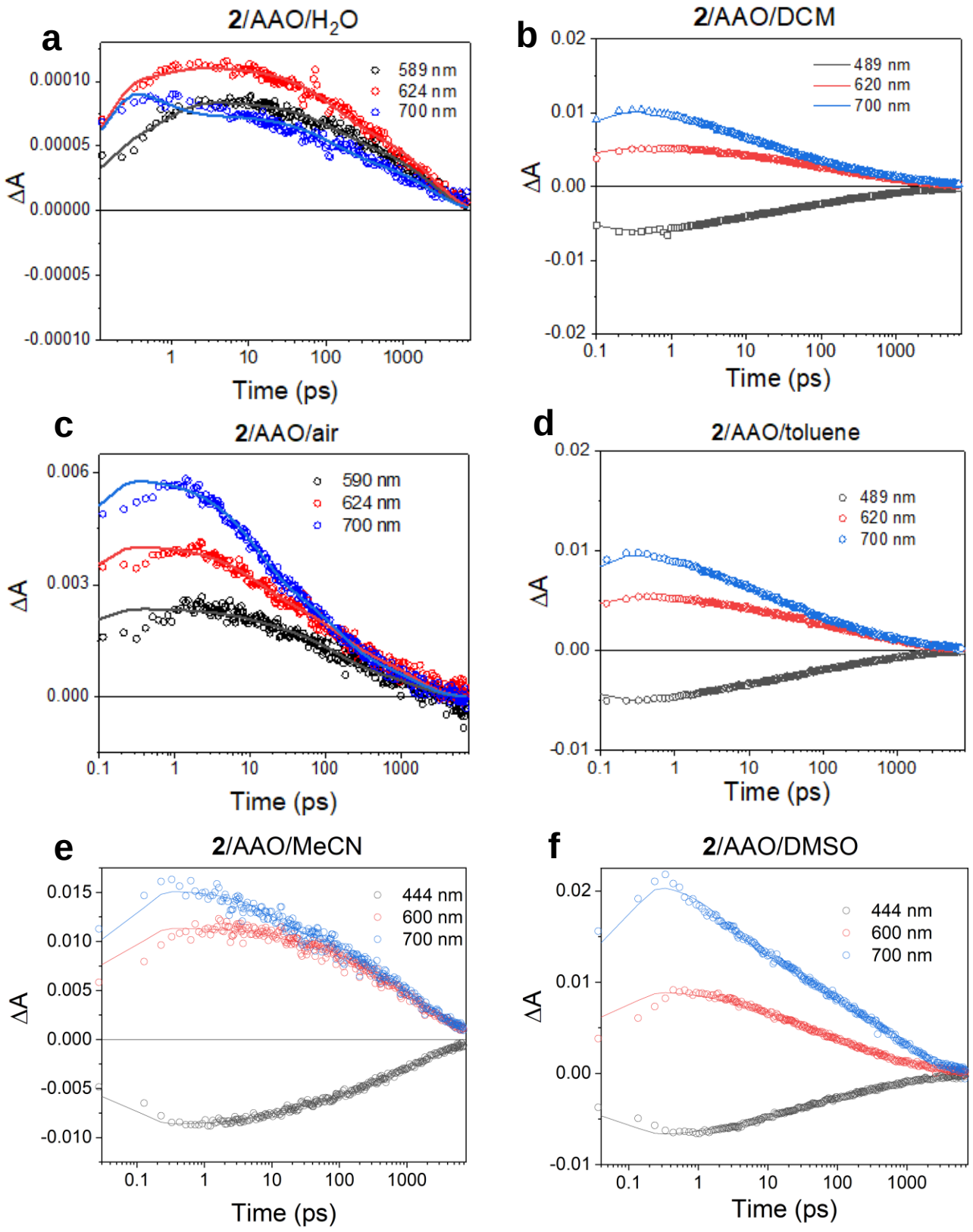


**Figure 2.18.** Kinetic fits for 2/AAO. (DCM = $CH_2Cl_2$; MeCN = acetonitrile; DMSO = dimethylsulfoxide)

# Chapter 3.

# Excimer Diffusivity in 9,10-Bis(phenylethynyl)anthracene Assemblies on Anodic Aluminum Oxide Membranes

## 3.1 INTRODUCTION

To meet the world's energy demands, solar energy must be captured, transferred, and stored efficiently.[87] The efficiency of natural photosynthetic light harvesting systems depends on the electronic energy transfer between molecules in chromophore assemblies (often comprised of ~200 chromophores) that surround a reaction center.[7, 88-90] Because the electronic coupling between the chromophores determines the degree of energy transfer and can be tuned by the modifying the distance and orientation between molecules, research efforts have focused on creating self-assembled supramolecular chromophore structures.[91] The interactions between chromophores in these assemblies can be optimized through rational design of the constituent molecules, making them suitable systems for studying light harvesting applications. In these photoactive assemblies, a variety of excited-state dynamics occur, including symmetry-breaking-charge transfer, excimer formation, and singlet fission.[92-94] Supramolecular assemblies have been formed from molecules by exploiting their π-π interactions, hydrogen bonding,[25-27] and host-guest interactions.[95] Alternatively, nanoporous anodic aluminum oxide (AAO) membranes can be used to create ordered supramolecular aggregates through either covalent binding to the pore walls or electrostatic interactions between the molecules and lipid-coated walls.

The strong electronic coupling between the molecules in self-assembled 9,10-bis(phenylethynyl)anthracene (BPEA) molecules covalently bound to AAO membranes induces excimer formation, which has been observed for BPEA molecular dimers.[96] In light harvesting applications, the excimer is often viewed as an undesirable lower energy trap state.[94, 97] Despite their lower energy compared to the first singlet excited state, pyrene excimers have a high fluorescence quantum yield making them good blue light emitters,[98] benzanthracene excimers emit green light useful for organic light-emitting diodes (OLEDs),[99] and cyanovinylene excimers can

probe caspase for disease diagnostics.[100] Additionally, the lifetime of excimer states typically exceeds that of the singlet excited state of one of the constituent chromophores, which enhances their ability to undergo further transformation or to be harvested prior to decay. Hence, excimers are useful in a range of applications including energy conversion although they limit energy migration, and a comprehensive description of the excimer state, and in particular its mobility, is needed to exploit its useful properties. The formation of excimer states is known to be a multi-step process, in which a primary exciton forms an intermediate before decaying to the ground state from its relaxed excimer state.[101-103] This depiction indicates that excimers share characteristics of excitons, a key to fully describing the character of the relaxed exciton intermediate that is shown to have useful applications. Numerous studies have shown that excimer and exciton states share a degree of mobility, and excimer exciton diffusion constants have been reported for pyrene excimers.[80, 104-106] In the remainder of this paper, the term excimer will be used to indicate the mobile excimer exciton.

In this study, we probe the excimer mobility in supramolecular assemblies of BPEA chromophores on AAO membranes. We have demonstrated that BPEA dimers in solution undergo rapid excimer formation times (<1 ps), while having relatively long lifetimes (~10s of ns), both of which were modulated by the relative degree of overlap between BPEA units and the solvent environment.[96] Formally, excimers are considered a mixture of local (Frenkel) excitonic states and charge resonance or charge transfer (CT) states.[55-57, 107-110] The charge transfer contribution of the exciton state can be modulated by the dielectric environment, with more polar solvents stabilizing the constituent CT state and promoting mixing with the singlet excited state. This increased CT character typically lowers the overall energy of the excimer state, leading to a red-shift and broadening of the excimer emission and an abbreviation of the excimer state lifetime.

Hence it is desirable to work with excimers in a low polarity environment to maximize both the excimer energy, but also to mimic the environment of organic solids. For these reasons we submersed the BPEA-AAO membranes in toluene (ε = 2.38). Although the length of the *N*-(3-(triethoxysilyl)propyl) functional group in each silyl-BPEA (Figure 3.1) is fixed, the inhomogeneity of the AAO surface may allow for a distribution in lateral slip distances, which can also affect the electronic coupling[111] and potentially influence excimer migration.

Using transient absorption spectroscopy, we calculate diffusion coefficients to compare the excimer mobility in BPEA assemblies to that of other chromophore aggregates. These findings align with previous studies that show that the excimer is generally less mobile than primary excitons and expands our understanding of excimers in multichromophore systems. The AAO membrane geometry confines the mobility of the excimer to one dimension, highlighting the ability of the nanostructure to serve as a platform that forces many chromophores into specific geometric relationships. BPEA molecules self-assembled on AAO membranes also represent the mesoscopic regime between the solution phase and solid state in which we can study both how bimolecular diffusion in solution and close packing in the AAO membrane influence the mechanism of excimer formation and diffusion. Immersing the BPEA-AAO system in toluene allows some degree of solvent-assisted structural rearrangement between the BPEAs.[112] At the same time, this supramolecular structure with intrinsic disorder displays the close packing of molecules seen in nanoparticles and single crystals, which often leads to instantaneous excimer formation because the molecules in *H*-aggregates are pre-associated. Our findings support an exciton theory description of the excimer and its application to a wider range of supramolecular systems. The BPEA excimer has a greater mobility than that of the pyrene excimer and is only an order of magnitude lower than the highly mobile excitons in non-fullerene based acceptor

chromophores used in organic photovoltaic (OPV) cells.[113] This study explores a unique instance of mobile excimers in a nanoporous material that is distinct from the well-studied pyrene excimer and will guide the future synthesis of supramolecular systems to study energy transfer in light harvesting systems.

## 3.2 EXPERIMENTAL

### 3.2.1 Synthesis

The synthesis of silyl-BPEA is shown in Figure 3.1. Details of the synthetic procedures and purification methods are given in the Supporting Information (Section 3.5).

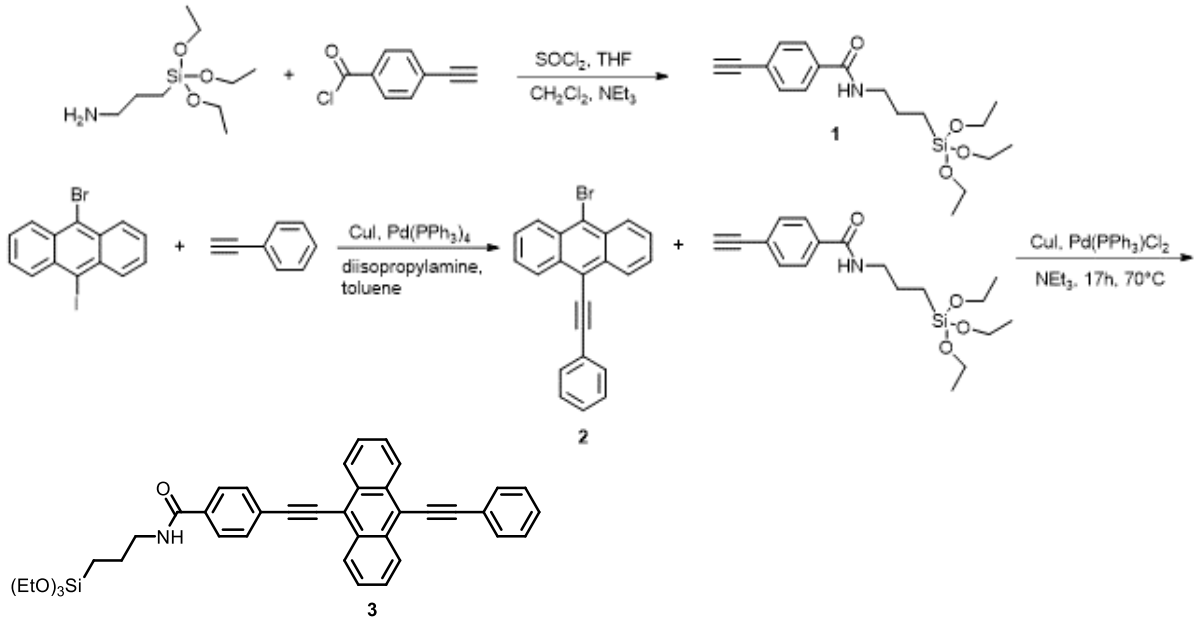


**Figure 3.1.** Synthesis of silyl-BPEA (3) by Sonogashira coupling of 1 and 2.

### 3.2.2 Preparation of AAO Assemblies

An InRedox AAO membrane wafer (diameter = 1 cm, pore size = 80 nm, thickness = 50 μm) was prepared by first sonicating it in deionized water and then in MeOH each for 5 min. The AAO membrane was immersed in a 1 mM solution in toluene of silyl-BPEA for 24 h. Afterward,

the residual silyl-BPEA was washed away by flowing dichloromethane, methanol, and toluene through the AAO membrane pores. The silyl-BPEA functionalized AAO membranes were dried prior to measurements. The AAO membrane was placed in a 1 mm thick cuvette (Starna Cells) filled with toluene solvent for time-resolved measurements.

### 3.2.3 Transient Absorption Spectroscopy

The femtosecond and nanosecond transient absorption (fsTA) experiments were conducted using a previously described instrument.[96] The 414 nm pump pulses were generated using by frequency-doubling the 827 nm fundamental, and the 430 nm excitation pulses were generated in a commercial collinear optical parametric amplifier (TOPAS-Prime, Light-Conversion, LLC). Excitation power was modulated using a neutral density filter and depolarized to suppress the effects of orientational dynamics. Transient absorption spectra were detected using a customized Helios/EOS spectrometer (Ultrafast Systems, LLC).

## 3.3 RESULTS AND DISCUSSION

### 3.3.1 Properties of the BPEA-AAO membrane assemblies

The **s**ilyl-BPEA reacts with the hydroxy-terminated surface of the AAO membrane to form siloxane attachments to the AAO membrane pore walls. The total number of BPEA molecules loaded into the membrane was calculated using the mass ($m$) of the silyl-BPEA attached to the membrane and it was assumed that the BPEAs occupy the volume of an annulus that is one BPEA molecule thick and are evenly spaced on a square with surface area of one pore ($A$). The average distance between the chromophores is ~2.8 Å, indicating that the BPEAs are π-stacked in the AAO pore. Average distance calculations using the model shown in Figure 3.5 are presented in Section 3.5.2. The aggregation implied by this short intermolecular distance between BPEAs in the AAO

pores is observed directly as changes in the vibronic bands of the steady-state absorption and emission spectra.

### 3.3.2 Steady-State Optical Properties

The steady-state absorption spectra of the silyl-BPEA monomer shows 0-0 and 0-1 bands with maxima at 468 and 446 nm, where the 0-0 transition has greater intensity than the 0-1 transition (Figure 3.2a). The steady state emission of the BPEA monomer in dichloromethane shows the clear vibronic progressions of the 0-0, 1-0, and 2-0 bands, as seen in previously reported emission spectra of BPEA monomer.[96] The crossing point of the absorption and emission curves yields a lowest excited state singlet energy of 2.61 eV.

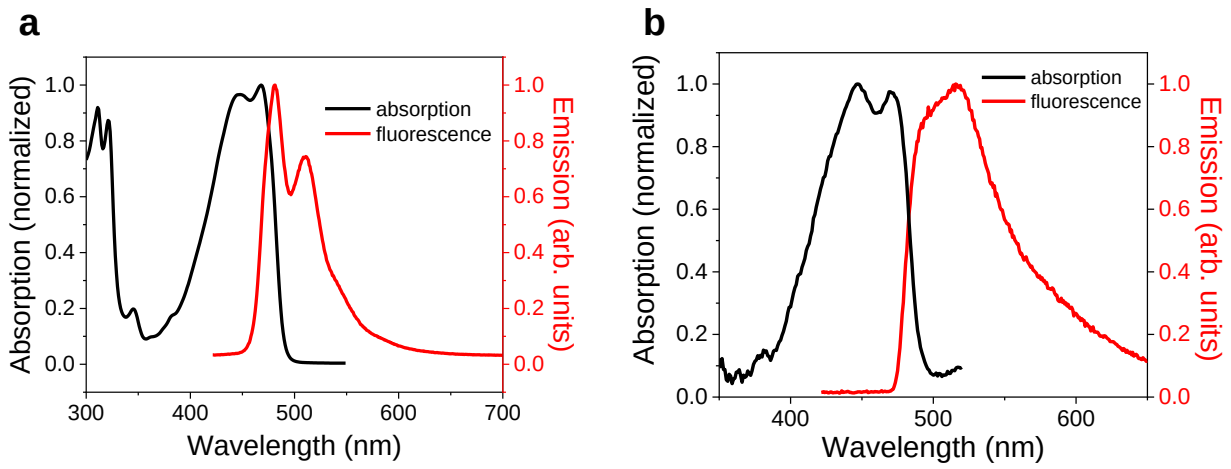


**Figure 3.2.** Steady-state absorption of emission spectra of silyl-BPEA (a) in solution and (b) on AAO

In contrast, the BPEA assemblies on the AAO membrane have a 0-1 absorption transition with a higher intensity than the 0-0 transition (Figure 3.2b). The higher intensity of the 0-1 transition indicates that the BPEA assemblies resemble *H*-aggregates.[14] The maxima of the 0-0 and 0-1 transitions are at 470 and 447 nm, respectively, and are redshifted slightly from those of the BPEA monomer. The steady-state emission spectrum of the BPEA assembly on the AAO membrane is broadened and redshifted with the 0-0 and 1-0 bands at 517 and 494 nm, respectively. In addition,

a broad emission band characteristic of excimer formation occurs at ~570 nm, which corresponds to an excimer state energy of ~2.2 eV. The emission spectra resemble that of a recently reported rigid π-stacked BPEA molecular dimer in which the two BPEA molecules are slipped along their long axes by ~4.3 Å[96] as well as that of a BPEA cyclophane,[114] both of which displayed somewhat distinct vibronic progressions in their emission spectra.

### 3.3.3 Excited-State Dynamics

The fsTA spectra of monomeric silyl-BPEA in dichloromethane solution show a ground-state bleach (GSB) from 415-470 nm, stimulated emission from 470-510 nm, and a sharp excited-state absorption (ESA) band from 520-635 nm (Figure 3.6). The ESA decays to the ground state over the 8 ns pump-probe delay window. Similar spectral features and lifetimes are observed for unsubstituted BPEA.[111]

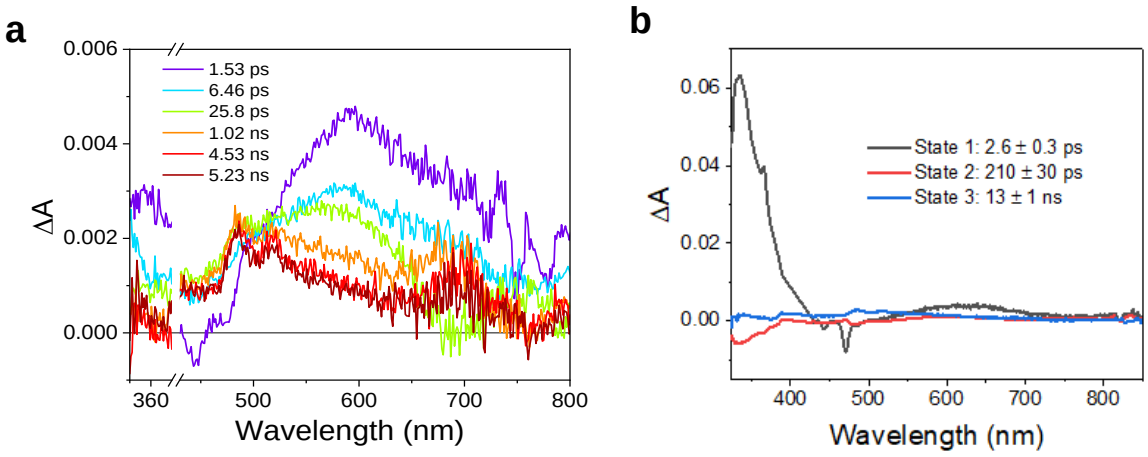


**Figure 3.3.** (a) fsTA spectra of silyl-BPEA covalently bound to AAO; (b) The decay-associated spectra extracted from the decay-associated global fit.

Transient absorption data of silyl-BPEA covalently bound to AAO reveal fast formation of an excimer species. Within the first few picoseconds after excitation of the BPEA-AAO assembly in toluene at 414 nm, there is a GSB from 435-455 nm with very little stimulated emission (SE) from

480-500 nm observed. An absorption band that spans 500-700 nm and is centered at 595 nm slightly broadens over ~30 ps and blue shifts to form absorption maxima at 486 and 695 nm (Figure 3.3a). Near zero-time delay there is a strong non-resonant response from the toluene solvent and AAO membrane that is prominent below 400 nm and persists for the first picosecond; this feature is not involved in the BPEA excited-state dynamics. A decay-associated global fit of the data using a sum of three exponentials shows a state that decays in 2.6 ± 0.3 ps (state 1, Figure 3.3b); this is assigned to the decay of the localized exciton state because the 0-0 transition at 470 nm is stronger than the 0-1 transition at 443 nm. The non-resonant response is also partially captured by this state. States 2 and 3 show the ESA of the excimer species with slower decays (210 ± 30 ps and ~13 ns, respectively), with the primary spectral difference between them being that the 486 nm absorption band is more prominent in state 3 (blue). The significant π-π orbital overlap between the BPEAs in the BPEA-AAO system as indicated by the close interchromophore distance promotes excimer formation, as has been observed for BPEA molecular dimers.[96] Thus, the excimer formation time is 2.6 ± 0.3 ps, similar to that observed for a π-stacked BPEA molecular dimer in which the two BPEA molecules are slip-stacked by ~8.6 Å along their long axes,[96] which may indicate some conformational disorder in the stacking as the formation time is slower than for direct, cofacial stacking. The slower time constants associated with states 2 and 3 may imply some degree of either structural relaxation or population loss due to annihilation. While the data can be adequately fit using exponential decays, we will demonstrate below that they are more properly interpreted using non-first order diffusion kinetics for exciton annihilation.

Previous work has also shown that the structure of the BPEA molecular dimer having ~8.6 Å slip-stacked BPEA molecules has a dihedral angle $\theta = 22°$ between the π systems of the two BPEA molecules while the corresponding angle in the BPEA dimer slip-stacked by only ~4.3 Å is $\theta$ =

41°. Solvation would change that optimized geometry and twist angle between the chromophores, modulating the mixing between the singlet exciton and CT states and altering the excimer energy.[96] Additionally, the penetration of a solvent molecule between the chromophores in the two-phenyl spaced BPEA might decrease the twist angle and increase the π-surface overlap because of a more cofacial orientation, though at the expense of increasing the center-to-center distance between the BPEA units. The π-surfaces of the BPEAs would still interact strongly because excimer formation occurs in AAO assemblies even with solvent molecules penetrating between the chromophores.[112] The energetics of the excimer are also influenced by the solvent, which also impacts the excimer mobility in the BPEA-AAO assemblies.

Numerous studies have also reported a multi-step excimer formation process in aromatic hydrocarbons such as perylene and pyrene.[101, 115-116] The observed relaxation is due to intermolecular structural changes to stabilize the excimer.[92, 102] Another possibility is that a vibrationally excited excimer is formed rapidly after excitation that then cools to a relaxed state. This mechanism is ruled out because there is no band narrowing or shifting, which is characteristic of thermal effects.[80] Changes in electronic structure manifest in the fsTA spectra as the appearance of the absorption maxima at 486 and 695 nm, indicating that intermolecular structural changes are indeed reasonable in the BPEA-AAO system.

Notably, singlet fission (SF) is absent in this system because the intermolecular packing differs significantly from that of BPEA polycrystalline films that undergo SF.[111] Here, rapid excimer formation is outcompeting SF, which occurs on the ≥100 ps timescale in polycrystalline thin films. We attribute the rapid excimer formation in BPEA aggregates on AAO membranes to the strong CT contribution, as seen in the molecular dimers. At the same time, the CT contribution is

insufficient to promote symmetry-breaking charge separation to form a BPEA contact ion pair and has been observed as a minor decay pathway in covalent BPEA dimers.[96]

### 3.3.4 Excimer Mobility in One Dimension

The transient absorption spectra show that bands closely related to the Frenkel exciton state evolve into other absorption bands that are signatures of the excimer state. From the perspective of exciton theory, the excimer is described as an exciton that has relaxed through intermolecular structural changes to an excimer geometry that allows for mixing with the CT states.[80]

This concept of the excimer implies a degree of mobility through the chromophore assembly. Exciton mobility is a shared characteristic of both excimers and Frenkel excitons [104-106] and has been observed for a range of organic chromophores. The mobility of the excimer state in the system presented here is supported by our observation that ΔA in the transient absorption data is sensitive to incident pump power, as seen in Figure 3a. As the pump power increases from 0.25-1.50 mW, ΔA decays more rapidly (Figures 3.7-3.11). This indicates that the kinetics are not purely first-order, meaning that even though the TA data were reasonably well fit by exponential functions (Figure 3.3), the underlying dynamics are better described using more complicated processes. Annihilation between the Frenkel exciton states is ruled out as the cause of the intermediate time behavior because the transformation to the excimer state is sufficiently fast to outcompete Frenkel annihilation, with excimer formation observed directly in the data within the first few ps. Thus, we consider annihilation between nearby excimers and that these excimers are mobile.

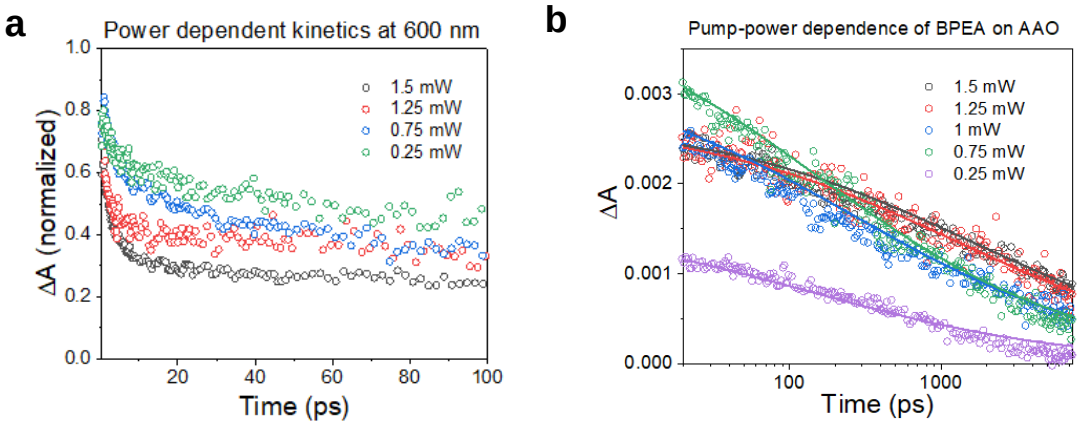


**Figure 3.4.** (a) Power dependence of ΔA signal at 600 nm where the excimer exciton photoinduced absorption band appears, taken as the average from 595-605 nm. (b) Fit of the TA data to the one-dimensional exciton annihilation model at different pump powers.

Excimer mobility was investigated in the BPEA assemblies by studying the dependence of ΔA on the excitation photon fluence. In systems with high exciton densities, ultrafast bimolecular annihilation can occur where one exciton transfers its energy to a neighboring exciton. One exciton then decays to the ground state while the other is promoted to a higher excited state that is singlet in character before relaxing to the $S_1$ state. The bimolecular annihilation rate constant can be used to determine diffusion coefficients and exciton diffusion lengths. The decay curves are fit to the kinetic model for bimolecular one-dimensional annihilation based on the geometry of the system where the π-π interactions in columnar BPEA aggregates on the AAO membrane force the diffusion to be preferentially one-dimensional. Following formation, the excimers decay according to the kinetic model:

$$\frac{d[\mathrm{E}]}{dt} = -k_1[\mathrm{E}] - k_2[\mathrm{E}]^2 \qquad \text{(Eqn. 3.1)}$$

where $k_1$ is the intrinsic unimolecular decay rate constant of the excimer and $k_2$ is the bimolecular annihilation rate coefficient, which can take on a time-dependence based on the dimensionality of the exciton diffusion. For one-dimensional diffusion, this coefficient is expressed as:[117]

$$k_2(t) = \pi R_\rho^2 \sqrt{\frac{8D_{1D}}{\pi t}} = \frac{C}{\sqrt{t}} \quad \text{(Eqn. 3.2)}$$

where $R_\rho$ is the annihilation radius, $D_{1D}$ the one-dimensional diffusion coefficient, and $C$ is a composite constant that is determined by the fit and used to extract $D_{1D}$. We assume that the distance $R_\rho$ = 1.1 Å, based on the average annihilation radius for reported organic materials (see SI for details).

The intrinsic lifetime of the BPEA excimer state ($k_1$ ~ (10 ns)$^{-1}$)[96] is significantly longer than the 10s of ps timescale on which we observe exciton annihilation, and at larger pump fluences we can neglect it in eqn. 3.1 to yield:

$$\frac{d[\mathrm{E}]}{dt} = -k_2[\mathrm{E}]^2 \quad \text{(Eqn. 3.3)}$$

which can be solved to obtain the time-dependent excimer concentration:[118]

$$[\mathrm{E}] = ([E]_0^{-1} + 2C\sqrt{t})^{-1} \quad \text{(Eqn. 3.4)}$$

The excimer appears in the time-resolved spectra as the excited-state absorption (ESA) centered at 600 nm. The transient absorption data were fit to (3.4) and the diffusion coefficient was obtained by solving for $D_{1D}$ in (3.2). The details of calculating the diffusion coefficient and the constant $C$ in (3.2) are detailed in Section 3.5.5. It was observed that the annihilation rate coefficient, $k_2$, changes with pump power due to the number of initial excimer states formed (Figure 3.13). This trend has also been observed in an organic cocrystal that undergoes charge-transfer biexciton annihilation.[42] The average diffusion coefficient of the excimer is 2.4× 10$^{-3}$ cm$^2$/s at a pump power of 1.5 mW (far into the annihilation regime), which is only about an order of magnitude lower than that of singlet excitons in organic materials with strong π-π interactions.[119-120] The lower diffusivity of the excimer is due to the intermolecular structural changes in the BPEA aggregate that lead to

reduced efficiency of the energy transfer process.[80] The reduced mobility of the excimer in the one-dimensional BPEA assemblies may also be due to the intrinsic heterogeneity of the AAO system where the molecules can adopt a range of conformations.[112] This disorder potentially disrupts the association of the BPEAs with one another in various areas of the assembly, further limiting the migration of the excimer. The change in the relative transition dipole moments of the BPEA molecules due to the structural relaxation that the excimer undergoes may also lead to less efficient Förster energy transfer.[121]

Potential mechanisms of excimer diffusion have been proposed where either the excimer adopts the ground-state geometry of an adjacent dimer pair, or a ground-state molecular dimer relaxes to the excimer geometry prior to energy transfer.[80, 106, 122-123] Previous studies of temperature-dependent pyrene absorption support a mechanism where the distance between the units of the ground-state dimer expands to the geometry of the excimer prior to the excitation energy transfer. It is also possible that the observed excimer diffusion occurs by a mechanism where both the distance between the units of the ground-state dimer expands, and the interplanar distance in the excimer contracts to accommodate energy transfer. However, since the emission of the BPEA aggregates is considerably perturbed compared to the monomeric emission, it is likely that the excimer geometry is also distorted relative to that of the monomer, as mixing with the CT state typically leads to structural changes as the excimer adjusts to the new electron distribution.

## 3.4 CONCLUSIONS

BPEA chromophores were self-assembled on nanoporous AAO membranes using silyl-BPEA. Excimer formation in this supramolecular system is a multi-step process and the system is well-described by exciton theory. This description reveals that the BPEA excimer undergoes one-dimensional diffusion in the AAO membrane. The BPEA-AAO assemblies show that the excimer

diffusion coefficient is greater than that of other excimers and is nearly as mobile as some singlet excitons. This makes it possible that BPEA chromophore aggregates can serve as light harvesting systems for solar energy applications.

## 3.5 SUPPLEMENTARY INFORMATION

### 3.5.1 Synthesis

**Instrumentation and materials.** All reagents and solvents were commercial grade and used without further purification. Column chromatography was performed on silica gel. $^{1}H$ nuclear magnetic resonance spectra were collected on a Bruker Avance III 500 MHz system and chemical shifts are recorded in ppm (δ) and samples dissolved in deuterated chloroform. The high-resolution mass spectroscopy (HRMS) spectra were taken on an Agilent LCTOF 6200 series mass spectrometer using electrospray ionization (ESI).

**Synthetic procedures.**

*Synthesis of N-(3-(triethoxysilyl)propyl)-4-ethylnylbenzamide (**1**)*

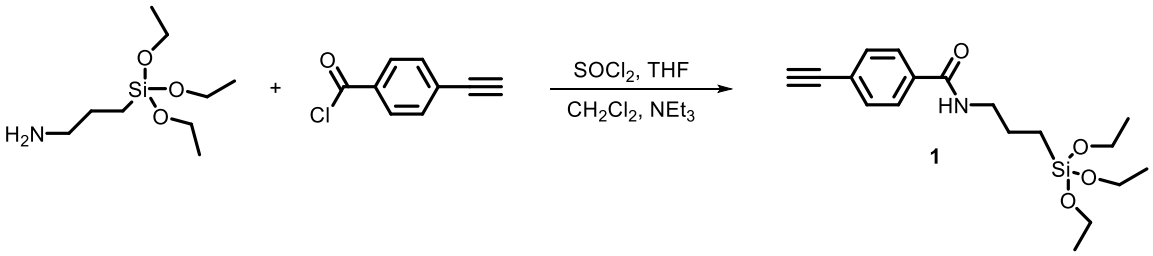


A previous synthetic procedure was followed for the synthesis of **1**.[124] 4-ethynylbenzoic acid (0.3 g), 3-aminopropyltriethoxysilane (0.6 mL), and $SOCl_2$ (5 mL) were refluxed in THF (20 mL) for 3h, and the mixture was vacuum distilled to remove residual solvent and $SOCl_2$. The black residue was dissolved in anhydrous $CH_2Cl_2$ (20 mL), then 3-aminopropyltriethoxysilane (20 mL) and $NEt_3$ (2 mL) were added dropwise to the reaction. The mixture was dry loaded onto silica gel and

purified by column chromatography (75% hexanes: 25% EtOAc) to yield the pure product (311 mg, 44% yield) as a white solid.

$^1$H NMR (δ in $CDCl_3$, 500 MHz) *δ*: 7.72 (d, 2H), 7.53 (d, 2H), 6.53 (b, 1H), 3.83 (q, 6H), 3.46 (m, 2H), 3.18 (s, 1H), 1.76 (m, 2H), 1.24 (t, 9H), 0.69 (t, 2H)

*Synthesis of 9-Bromo-10-phenylethynylanthracene (**2**)*

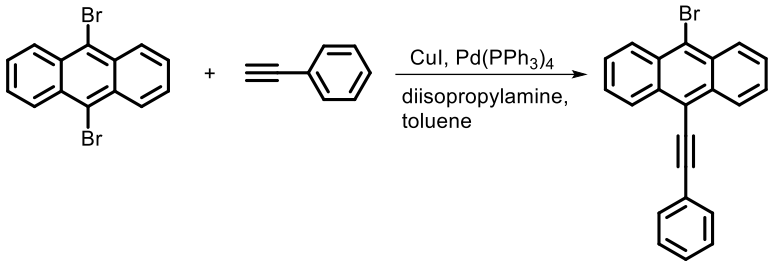


**2**

A mixture of 9,10-dibromoanthracene (1.5 g), phenylacetylene (0.43 g), and $Pd(PPh_3)_4$ dissolved in toluene:i-$Pr_2NH$ 7:3 was stirred under N2 at 55°C for 24 h. The reaction mixture was cooled to room temperature, $CH_2Cl_2$ was added, and the mixture was stirred until all the solid was dissolved. The mixture was extracted with $CH_2Cl_2$ (3x), washed with water, and dried over $Na_2SO_4$. The product was purified by column chromatography using a solvent gradient of 100% hexanes → 15% $CHCl_3$:85% hexanes to yield the pure product (340 mg, 25% yield) as yellow needles.

$^1$H NMR (δ in $CDCl_3$, 500 MHz): 8.69 (m, 2 H), 8.55 (m, 2 H), 7.73 (m, 2 H), 7.63 (m, 4 H), 7.42 (m, 3 H).

*Synthesis of silyl-BPEA (**3**)*

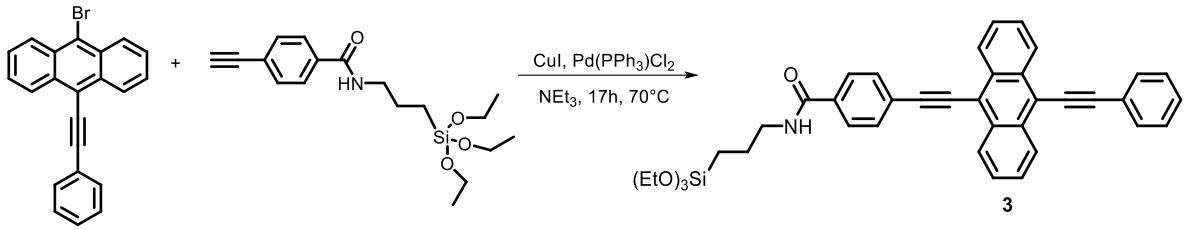


9-Bromo-10-phenylethynylanthracene (20 mg), *N*-(3-(triethoxysilyl)propyl)-4-ethynylbenzamide (19 mg), and CuI (1 mg) were dissolved in diisopropylamine:THF (10 mL:10mL) and degassed with $N_2$ for 15 min. $Pd(PPh_3)_2Cl_2$ (2 mg) was added to the reaction under N2 and the mixture was degassed for another 15 min. The reaction was heated to 70°C and run to completion over 20 h. The reaction was purified using column chromatography and eluted with 50% hexanes: 50% EtOAc to yield the pure product (15 mg, 40% yield).

$^1$H NMR (δ in $CDCl_3$, 500 MHz): 8.70 (m, 3H), 7.87 (d, 2H), 7.83 (d, 2H), 7.78 (dd, 2H), 7.75 (d, 1H), 7.66 (m, 3H), 7.58 (d, 1H), 7.45 (m, 3H), 6.63 (t, 1H), 3.84 (m, 6H), 3.51 (m, 2H), 1.79 (m, 2H), 1.25 (m, 9H), 0.72 (m, 2H). HR-MS (ESI)(m/z): [$M^+$] calc. for $C_{40}H_{39}NO_4Si$, 625.84; found, 626.27.

### 3.5.2 Average Distance between BPEAs on Nanoporous AAO Membranes

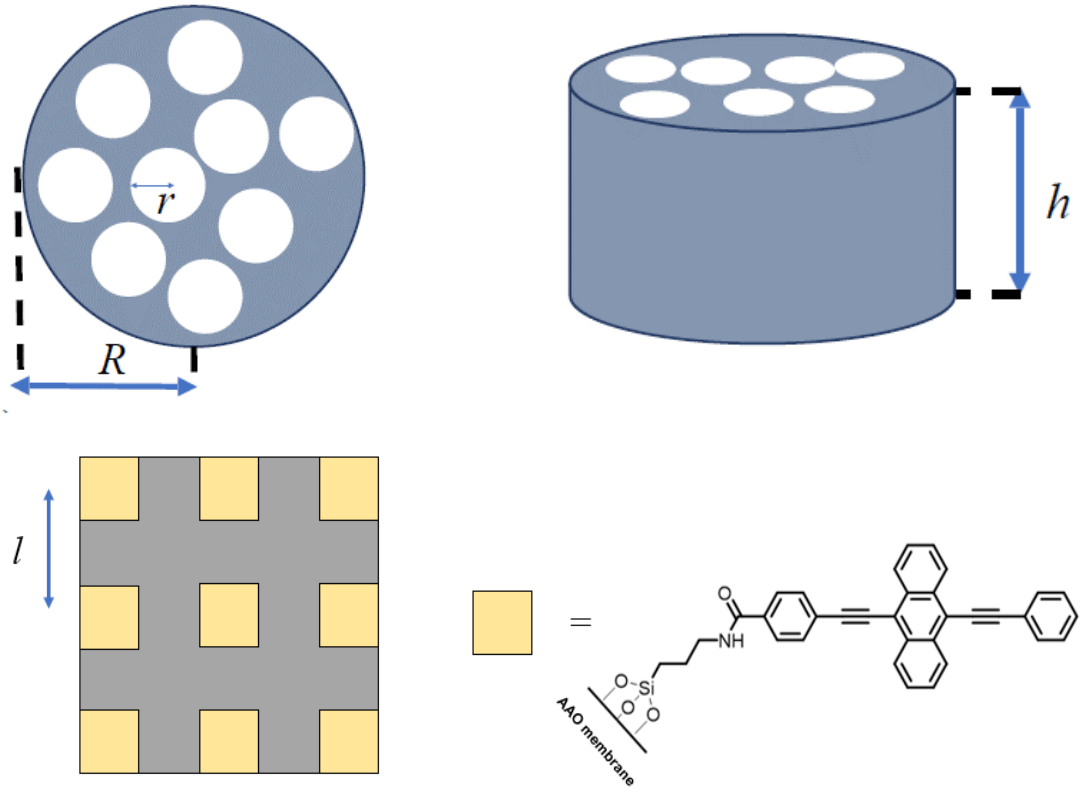


**Figure 3.5.** Schematic of AAO membranes depicting the parameters used for calculation of the average BPEA spacing.

Blank AAO membranes were pre-weighed and soaked in a solution of silyl-BPEA for 24 h. After extensive rinsing with DCM and drying, the coated AAO membranes were weighed to obtain the average mass ($m$) of silyl-BPEA covalently bound to the AAO membranes. Thus, the mass $m$ = 0.4 mg for silyl-BPEA bound to one AAO membrane. The pore density ($d$) of the AAO membrane is $3\times10^9$ $cm^{-2}$ (provided by the manufacturer InRedox).

The total number of pores in the AAO membrane is:

$$N = \pi R^2 d \quad \text{(Eqn. 3.5)}$$

The surface area ($S$) of one pore is:

$$S = 2\pi r h \quad \text{(Eqn. 3.6)}$$

Therefore, the total surface area $A$ of the AAO membrane is:

$$A = 2\pi R \times h + 2(\pi R^2 - N\pi r^2) + NS \cong NS \quad \text{(Eqn. 3.7)}$$

The number of BPEA molecules on the AAO membrane is:

$$N_A \times \frac{m}{M_{BPEA}} \quad \text{(Eqn. 3.8)}$$

Assuming the distance $l$ between the BPEAs on AAO is the same, and the BPEAs are distributed evenly over a square with area $A$, the number of BPEAs on the AAO membrane can be described by equating two expressions:

$$\left(\frac{\sqrt{A}}{l}\right)^2 = N_A \times \frac{m}{M_{BPEA}} \quad \text{(Eqn. 3.9)}$$

The left side of the equation describes the number of BPEAs on AAO from the square with area $A$, while the right side uses the mass $m$ to determine the number of BPEAs. By solving the equation above for distance $l$, where $h$ is the height of the membrane, $r$ the radius of the AAO pore, $R$ the radius of the AAO membrane, $M_{BPEA}$ the molecular weight of the silyl-BPEA, and $N_A$ Avogadro's number. We calculate that the distance between the BPEAs on AAO is 0.28 nm.

### 3.5.3 Femtosecond Transient Absorption Spectroscopy

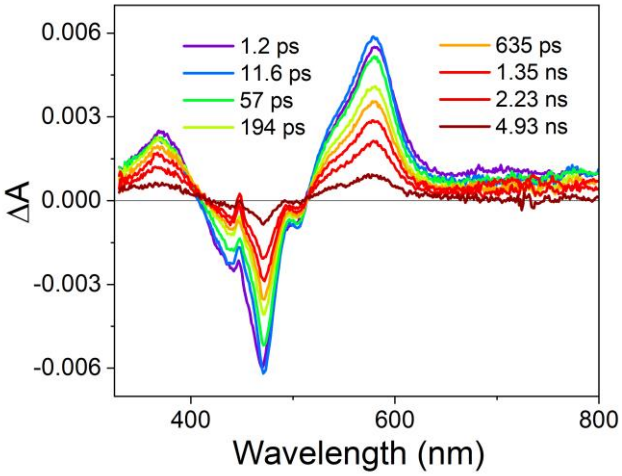


**Figure 3.6.** fsTA spectra of monomeric silyl-BPEA in dichloromethane following 414 nm, ~100 fs excitation (1 μJ/pulse) at 500 Hz.

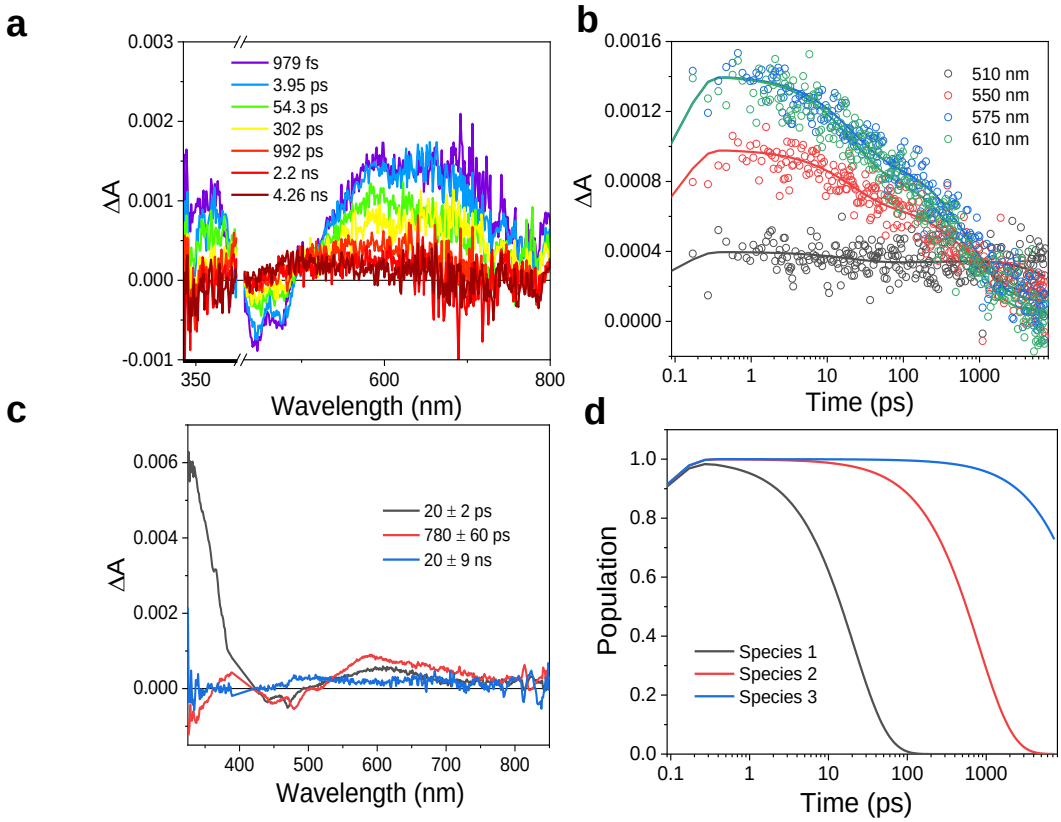


**Figure 3.7.** fsTA spectra of BPEA-AAO at 0.25 mW pump power: a) spectra, b) kinetic fits at selected wavelengths, c) decay-associated spectra, d) species populations.

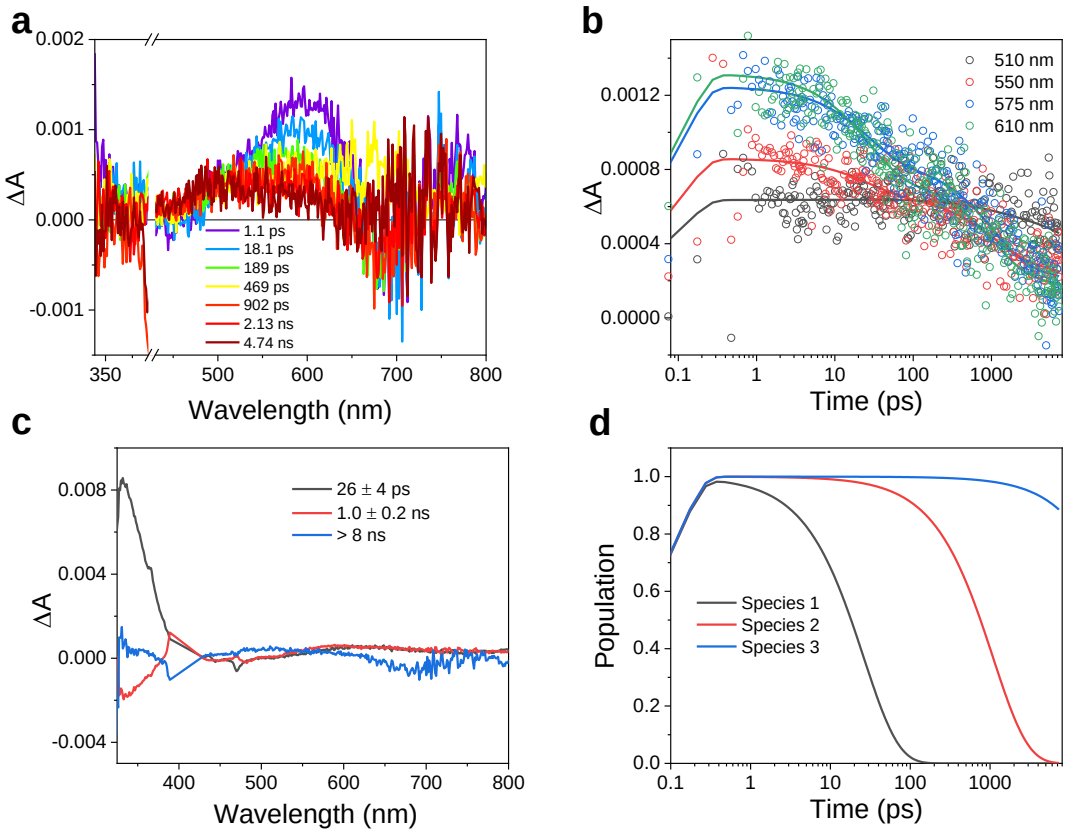


**Figure 3.8.** fsTA spectra of BPEA-AAO at 0.5 mW pump power: a) spectra, b) kinetic fits at selected wavelengths, c) decay-associated spectra, d) species populations.

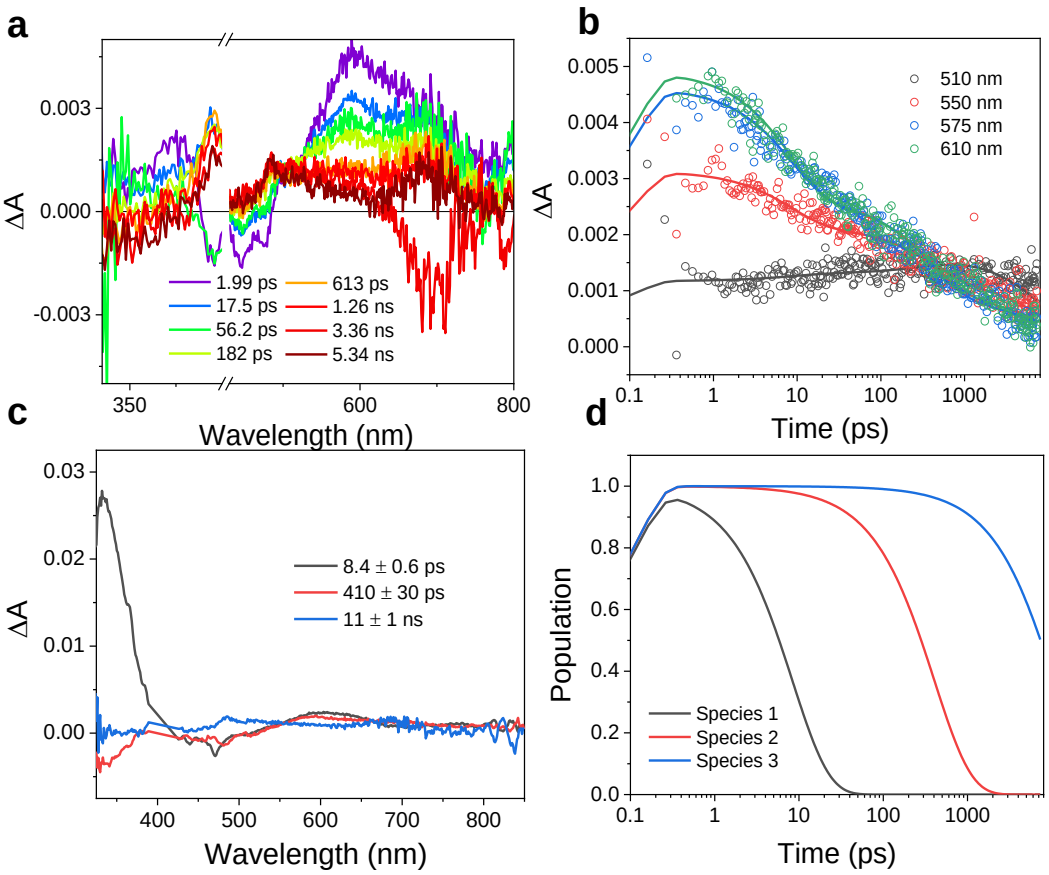


**Figure 3.9.** fsTA spectra of BPEA-AAO at 0.75 mW pump power: a) spectra, b) kinetic fits at selected wavelengths, c) decay-associated spectra, d) species populations.

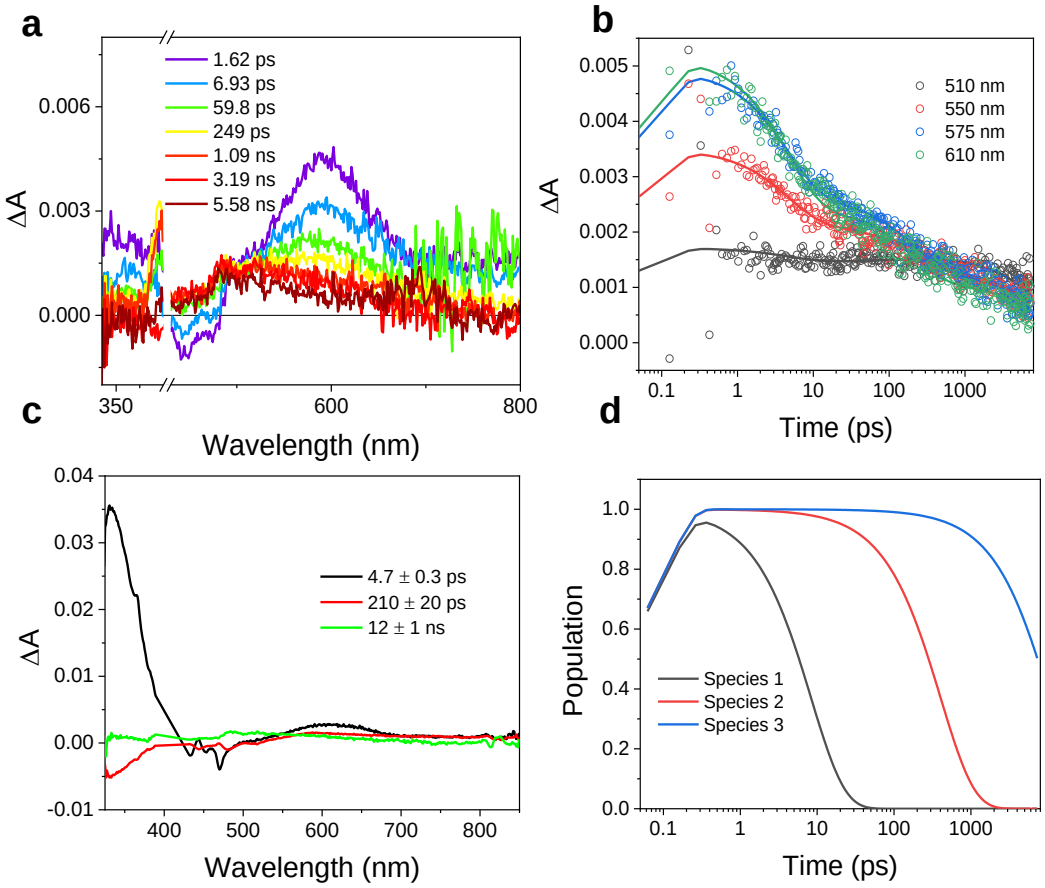


**Figure 3.10.** fsTA spectra of BPEA-AAO at 1.0 mW pump power: a) spectra, b) kinetic fits at selected wavelengths, c) decay-associated spectra, d) species populations.

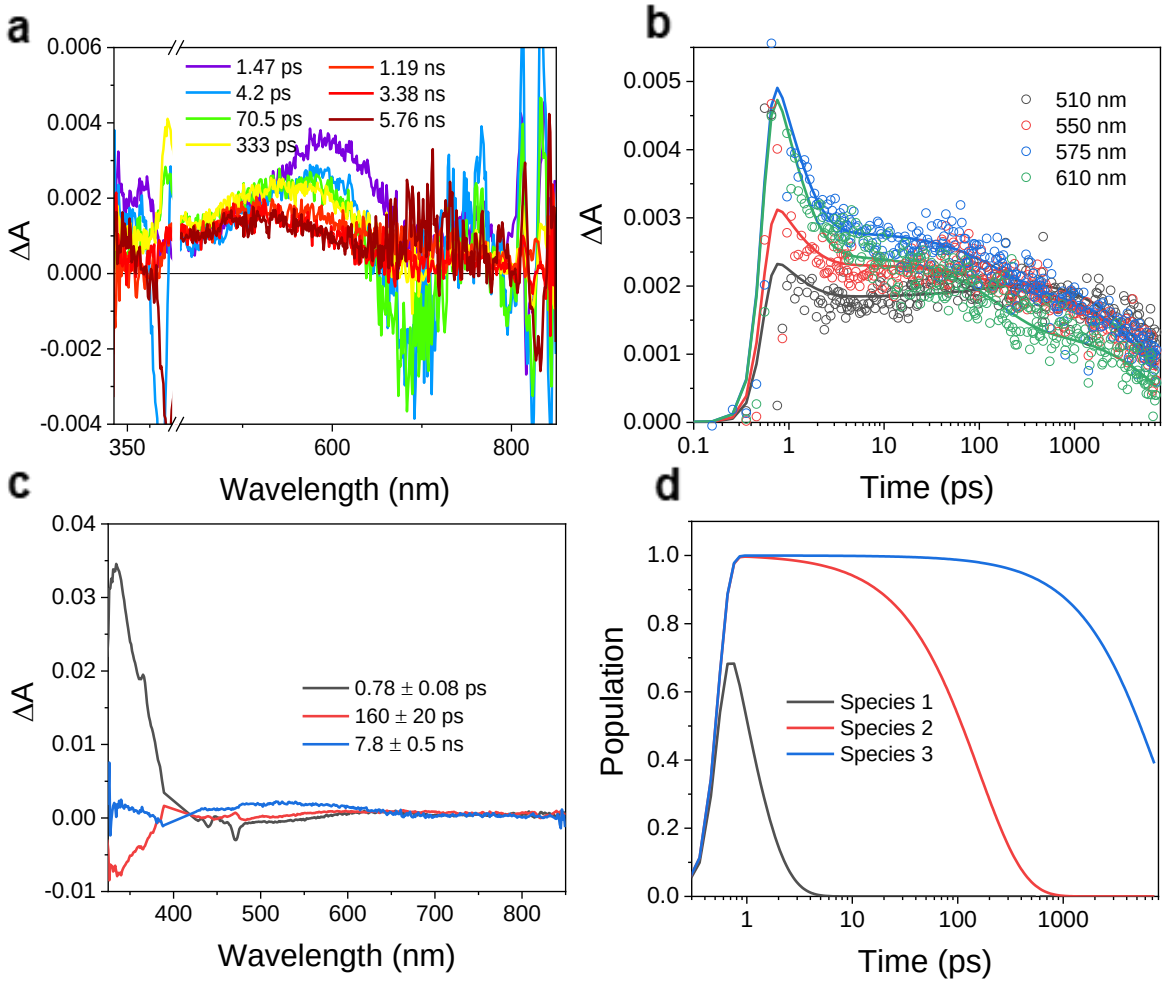


**Figure 3.11.** fsTA spectra of BPEA-AAO at 1.25 mW pump power: a) spectra, b) kinetic fits at selected wavelengths, c) decay-associated spectra, d) species populations.

### 3.5.4 Calculation of Excitation Density

The excitation density ($\xi$) is the number of absorbed photons ($N_p$) in the excitation volume ($V$) per pulse. The values $\lambda, P, A, f, r$, and $t$ are the excitation wavelength, pump power, absorbance at the excitation wavelength, pump repetition rate, radius of the probe beam, and thickness of the crystal. Values $h$ and $c$ are Planck's constant and the speed of light in a vacuum.

$$\xi = \frac{N_p}{V} \qquad \text{(Eqn. 3.10)}$$

$$N_p = \frac{\lambda \times P \times (1 - 10^{-A})}{h \times c \times f} \qquad \text{(Eqn. 3.11)}$$

The excitation volume ($V$) is the volume of an annulus of a ring of BPEA molecules around the pore rim, multiplied by the number of AAO pores in the probe area. $R$, $r$, $H$, $A_{probe}$, and $d$ are the radius of the pore, inner radius (to the edge of the annulus), height of the pore, area of probe (radius = 100 μm), and pore density, respectively.

For the experiment at these parameters the excitation density is: $3.78 \times 10^{18}$ cm$^{-3}$.

**Table 3.1**: Excitation density at different powers

| Power (mW) | Excitation density (cm$^{-3}$) |
|---|---|
| 1.5 | $3.78 \times 10^{18}$ |
| 1.25 | $3.15 \times 10^{18}$ |
| 1.0 | $2.52 \times 10^{18}$ |
| 0.75 | $1.89 \times 10^{18}$ |
| 0.25 | $6.29 \times 10^{17}$ |

$$V = \pi(R - r)^2 H \times A_{probe} \times d$$

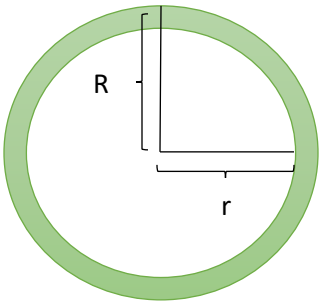


**Figure 3.12.** The area of an annulus of BPEA molecules in the AAO pore is highlighted in green.

**Table 3.2.** Parameters for calculating number of photons, $N_p$

| $\lambda$ (nm) | $P$ (mW) | $A$ (OD) | $f$ (Hz) |
|---|---|---|---|
| 414 | 1.5 | 0.007 | 500 |

**Table 3.3.** Parameters for calculating excitation volume, $V$

| $R$ (nm) | $r$ (nm) | $H$ (μm) | $A_{probe}$ (cm$^2$) | $d$ (cm$^{-2}$) |
|---|---|---|---|---|
| 40 | 37.7 | 50 | $3.14\times10^{-4}$ | $3\times10^{9}$ |

### 3.5.5 Calculation of Diffusion Coefficient

To calculate the bimolecular rate coefficient, the data were fit to the following kinetic model. The excimers decay unimolecularly with an intrinsic lifetime not captured by the following one-dimensional diffusion model. We neglect the unimolecular decay process because it is >>10x slower than the excimer annihilation process. Excimers annihilate through one-dimensional diffusion:

$$\frac{d[\mathrm{E}]}{dt} = -k_2[\mathrm{E}]^2 \qquad \text{(Eqn. 3.12)}$$

Where [EE] is the concentration of excimers and $k_2$ is a Smoluchowski-type rate coefficient for diffusion-controlled excimer annihilation. Assuming one-dimensional diffusion of excimers and that annihilation is effectively instantaneous upon contact, $k_2$ may be related to the one-dimensional diffusion coefficient $D_{1D}$ and the annihilation radius $R_\rho$ of excimers by[117]:

$$k_2(t) = \pi {R_\rho}^2 \sqrt{\frac{8D_{1D}}{\pi t}} = \frac{C}{\sqrt{t}}, \quad C = \pi {R_\rho}^2 \sqrt{\frac{8D_{1D}}{\pi}} \qquad \text{(Eqn. 3.13)}$$

with $R_\rho$ estimated as 1.1 nm according to literature.[125] Solving the differential equation (3.12) with $k_2$ expressed as (3.13) yields[118]:

$$[\mathrm{E}] = ([E]_0^{-1} + 2C\sqrt{t})^{-1} \qquad \text{(Eqn. 3.14)}$$

where $[\mathrm{E}]_0$ is the initial concentration of excimers after excitation, and $k_2 = 2C$. With TA spectra, the concentration of excimers [E] at any given time *t* after can be expressed as:

$$[\mathrm{E}] = \frac{\Delta \mathrm{A}}{\Delta \mathrm{A}_0} \times [\mathrm{E}]_0 \qquad \text{(Eqn. 3.15)}$$

Where $\Delta A$ and $\Delta A_0$ are the TA signal at time *t* and at time zero, respectively. Assuming every photon absorbed by the system converts to an excimer, $[E]_0$ reduces to the excitation density $\xi$, calculated in the previous section.

Inserting equation (3.15) into (3.14), the evolution of TA signal in time can be expressed in units of $\Delta A$ as:

$$\Delta \mathrm{A} = (\Delta \mathrm{A}_0{}^{-1} + \frac{2\xi C}{\Delta \mathrm{A}_0}\sqrt{t})^{-1} \qquad \text{(Eqn. 3.16)}$$

The TA data excited at 414 nm were fit at 600 nm to equation (3.14) to obtain the *C* value, and finally equation (3.13) can be solved for the value of $D_{1D}$:

$$D_{1D} = \left(\frac{C}{\pi {R_\rho}^2}\right)^2 \times \frac{\pi}{8} = \frac{{k_2}^2}{32\pi {R_\rho}^4} \qquad \text{(Eqn. 3.17)}$$

### 3.5.6 Annihilation Rate vs. Power

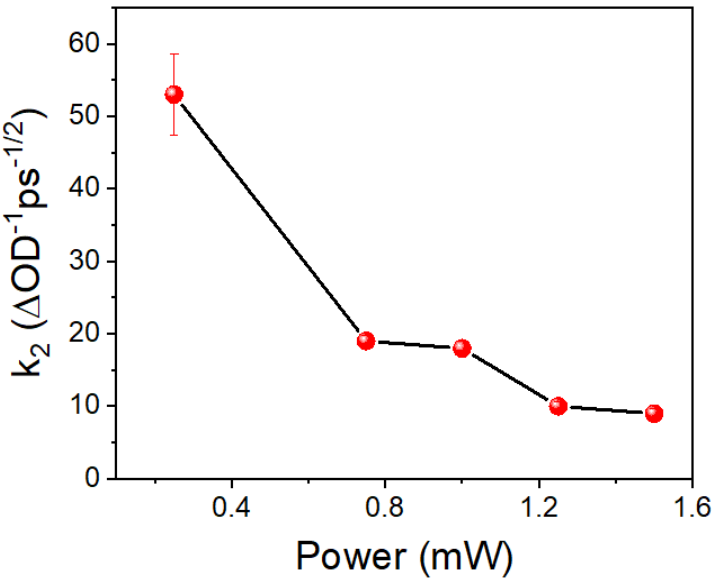


**Figure 3.13.** Rate coefficient of annihilation (from fitting to a one-dimensional annihilation model) vs. pump power. Annihilation rate decreases as power increases.

Using the values of $k_2$ defined above, the value of $C$ was obtained according to Eqns. 3.12-3.17 and calculated in units $cm^3\ s^{-1/2}$. The larger deviation and uncertainty associated with the extracted value of $k_2$ for lowest measured power is likely a consequence of neglecting first order decay or other, slower processes such as structural relaxation that are outcompeted by excimer annihilation at higher pump powers.

# Chapter 4.

# Ultrafast Photo-driven Charge Transfer Exciton Dynamics in Mixed-Stack Pyrene-Perylenediimide Single Cocrystals

***4.1 INTRODUCTION**

Organic donor-acceptor (D-A) cocrystals are formed by charge transfer (CT) interactions between their two components, which result in new photophysical properties[126-128] with potential applications in tunable dye lasers,[129-130] sensors,[131-132] and organic photovoltaics.[133-136] Several studies characterizing the CT ground state optical absorption as well as the steady-state and time-resolved photoluminescence of D-A co-crystals have been reported.[43-44, 46, 127, 137-145] While a few reports on excited state dynamics in D-A cocrystals employ transient absorption and emission spectroscopy on polycrystalline powders to draw conclusions about the crystal morphology dependence of the dynamics,[139, 146-149] there are even fewer studies that employ transient optical absorption measurements to study CT exciton dynamics in single D-A co-crystals.[150-152]

Port and co-workers reported the first example of using femtosecond transient absorption to study ultrafast CT exciton dynamics in single cocrystals of anthracene and PMDA.[150-151] We recently reported on a single cocrystal of a *peri*-xanthenoxanthene (PXX) donor with a *N*,*N*-bis(3-pentyl)-2,5,8,11-tetraphenylperylene-3,4:9,10-bis(dicarboximide) ($Ph_4PDI$) acceptor to give an orthorhombic PXX-$Ph_4PDI$ D-A π-stacked cocrystal with a CT transition dipole moment (TDM) perpendicular to the TDMs for $S_n \leftarrow S_0$ excitation of PXX and $Ph_4PDI$. Using polarized, broadband, femtosecond transient absorption microscopy (fsTAM), we determined that selective photoexcitation of $Ph_4PDI$ in the single cocrystal results in CT exciton formation within the 300-fs instrument response time. At early times ($0.3 \leq t \leq 500$ ps), the CT excitons decay with a $t^{-1/2}$ dependence, which was attributed to CT biexciton annihilation within the one-dimensional D-A π-stacks producing high-energy, long-lived (>8 ns) electron-hole pairs in the crystal.

Here, we have cocrystallized a pyrene (Pyr) electron donor with either an *N*,*N*′-bis(2,6-diisopropylphenyl)- or *N*,*N*′-bis(3-pentyl)-perylene-3,4:9,10-bis(dicarboximide) (diisoPDI or

$C_5$PDI) electron acceptor to yield single Pyr-diisoPDI or Pyr-$C_5$PDI donor-acceptor cocrystals with mixed π-stacking. Polarized, broadband fsTAM was used to study the CT exciton dynamics of Pyr-diisoPDI and Pyr-$C_5$PDI single cocrystals, which reveal that the CT exciton diffusion coefficient in the Pyr-diisoPDI cocrystal (~$3\times10^{-4}$ $cm^2/s$) is about two orders of magnitude higher than that of Pyr-$C_5$PDI (~$3.5\times10^{-6}$ $cm^2/s$). Additionally, when the pump polarization is perpendicular to its crystallographic *a*-axis (crystal long axis), the CT exciton decay kinetics in the Pyr-diisoPDI cocrystal are dominated by CT exciton annihilation, while charge recombination of the CT exciton contributes significantly to the dynamics when the pump polarization is parallel to the *a*-axis. In contrast, CT exciton recombination contributes significantly to the dynamics in the Pyr-$C_5$PDI cocrystal for both pump polarizations. A comparison of the two cocrystal morphologies shows that CT exciton diffusion is most likely confined to individual D-A π stacks in the Pyr-$C_5$PDI cocrystal, while rapid charge hopping or delocalization between adjacent donors and acceptors in the Pyr-diisoPDI cocrystal results in more rapid diffusion, even though CT exciton diffusion remains one-dimensional. These results provide insight into how crystal morphologies can be designed to tailor CT exciton mobilities in organic semiconductors for optoelectronic applications.

## 4.2. EXPERIMENTAL

### 4.2.1 Steady state absorption and emission microscopy

Steady-state absorption spectra on the single crystals were obtained using an adapted commercial epi-illumination microscope (Nikon Ti-U) using the white light continuum probe beam from the femtosecond apparatus (see below). The white light source was focused on the sample with a 60× objective lens (Nikon, NA= 0.70), and the transmitted light was collected and recollimated with another 50× objective lens (Nikon, NA= 0.55) mounted over the sample. The collimated output

was directed to a home-built spectrometer and the spectrally dispersed signal was recorded with a fast line-scan camera (OctoPlus, Teledyne e2v). To obtain an absorption spectrum, a reference transmission was first taken with the beam focused on the bare glass substrate, and the signal transmission was measured on the single crystal. The polarization of the beam was controlled with a broadband half-wave plate (HWP) before the microscope to obtain the steady-state absorption spectra at different polarizations.

Steady-state emission spectra were measured using a similar epi-illumination microscope (Nikon Ti-U), excited by a 532 nm continuous-wave laser (Spectra-Physics) beam. A 40× magnification objective lens (Nikon, NA = 0.60) was used both to focus the incident beam onto a single crystal and to collect the emitted light. The emitted light was then sent into an Acton spectrograph (Princeton Instruments) equipped with a PIXIS 400BR CCD Camera (Princeton Instruments). A long-pass filter was used to block the scattered excitation beam within the signal.

### 4.2.2 Transient absorption microscopy

Femtosecond transient absorption microscopy (fsTAM) was performed as follows: The 1040 nm fundamental output (> 8 W, < 400 fs, 200 kHz repetition rate) of a commercial amplified laser system (Spirit One, Spectra-Physics) was down-counted to 100 kHz with the integrated pulse picker, and then divided with a beam splitter (BS) into two beam paths. One beam (probe path) was sent to a double-pass linear delay line (Newport), and then focused into a 10 mm thick undoped yttrium aluminum garnet (YAG) crystal for white light continuum generation. The other fraction of the 1040 nm fundamental beam was used to drive a collinear optical parametric amplifier (Spirit-OPA, Spectra-Physics), which generated the visible pump pulses. The visible pump pulses were modulated at 50 kHz with an electro-optic amplitude modulator (EOAM-NR-C4, Thorlabs), which was synchronized to the fundamental laser output. The pump was converted to a circularly

polarized beam before entering the modulator, and the modulated output pump beam was routed through a polarizer. This is followed by dispersion compensation of the modulated pump pulses using a prism compressor consisting of two prisms. The pump and probe beams were co-axially combined using a 50:50 BS and sent into the same microscope setup, spectrometer, and camera used for steady-state absorption measurements described above. The polarizations of the pump and the probe beams were varied independently using two HWPs. The pump and probe focused spot sizes (FWHM) on the sample were 0.83 μm and 0.93 μm, with Gaussian beam shapes. The total instrument response function (IRF) was 400-600 fs.

## 4.3 RESULTS

### 4.3.1 Donor-acceptor cocrystal structures

Single cocrystals containing a 1:1 stoichiometric ratio of pyrene to either diisoPDI or $C_5$PDI in their unit cells were grown and their x-ray diffraction structures were determined using techniques given in Section 4.6. The Pyr-diisoPDI cocrystal is monoclinic with the space group $P2_1/c$. Bravais-Friedel-Donnay-Harker (BFDH) cell morphology calculations (Figure 4.5) show that the crystallographic *a*-axis is nearly parallel to the crystal long axis. The view down the *b*-*c*

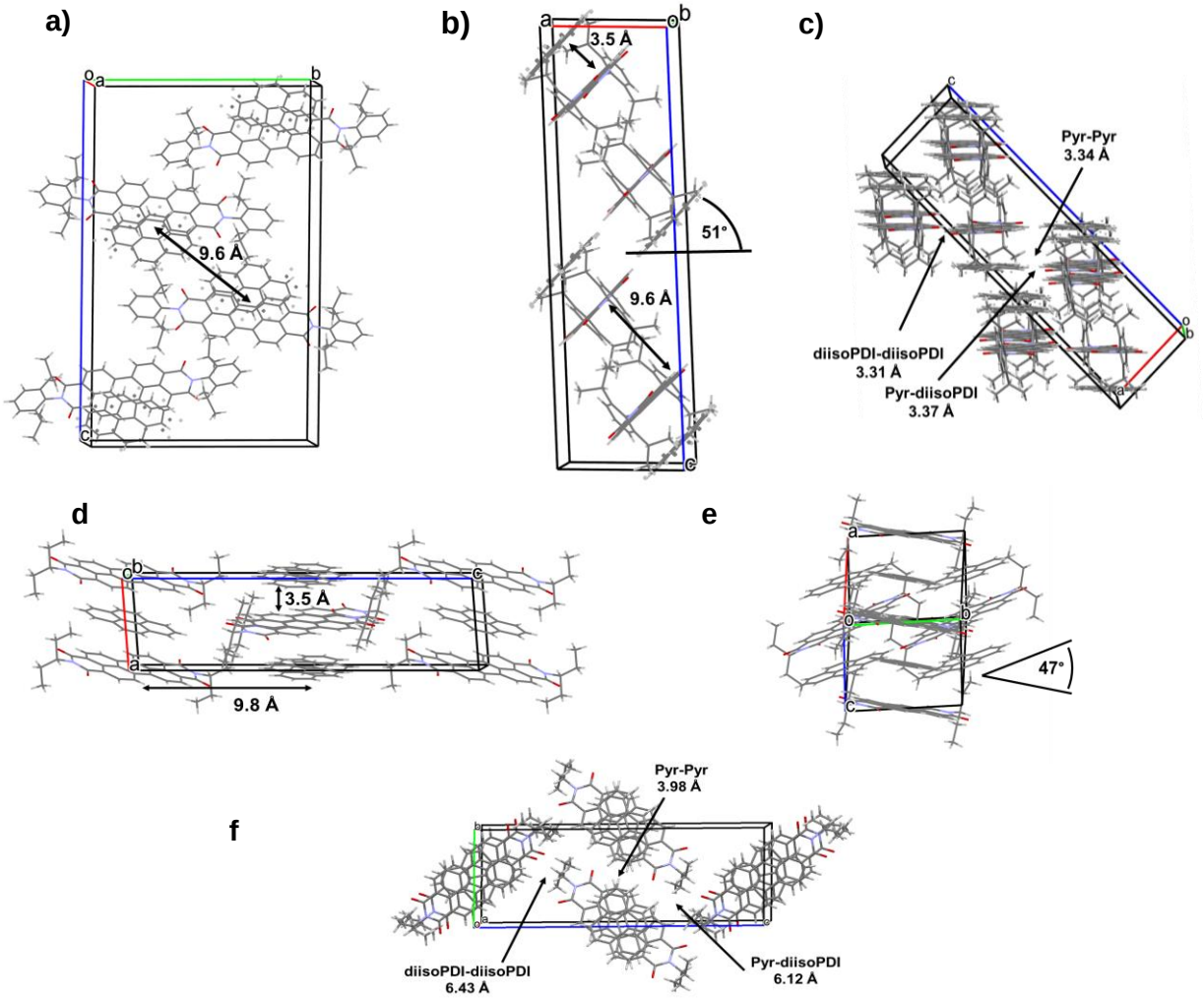


**Figure 4.1.** Pyr-diisoPDI cocrystal structure: (a) View down the *b*-*c* crystallographic plane with the interstack distance labeled, (b) View down the *a*-*c* crystallographic plane with the Pyr-diisoPDI and diisoPDI-diisoPDI distances labeled as well as the angle between the planes of the molecules and the crystallographic *c*-axis, and (c) View nearly in line with the crystallographic *b*-axis showing the edge-to-edge π-π distances of Pyr-Pyr, Pyr-diisoPDI, and diisoPDI-diisoPDI. Pyr-$C_5$PDI cocrystal structure: (d) View down the *a*-*c* crystallographic plane with intrastack and interstack distances labeled, (e) View down the *a*-*b* crystallographic plane, (f) View down the crystallographic *a*-axis with the Pyr- $C_5$PDI, $C_5$PDI- $C_5$PDI, and Pyr-Pyr distances labeled.

crystallographic plane shows that the interstack distance between the D-A pairs is 9.6 Å (Figure 4.1a). The planes of the diisoPDI and pyrene molecules are tilted 51° from the *a*-axis of the unit cell (Figure 4.1b) and the Pyr-diisoPDI π-π stacking distance is 3.5 Å. While the center-to-center distance between two diisoPDI molecules in separate D-A stacks is 7.2 Å, they have an edge-to-edge distance of one of their oxygen atoms to the carbon atom of an adjacent diisoPDI of only 3.31

Å (Figure 4.1c). The structure also shows that half of the Pyr molecules are in the same plane as diisoPDI with an edge-to-edge closest distance of the diisoPDI oxygen atom to the Pyr carbon atom of 3.37 Å. In addition, adjacent Pyr molecules have a slip-stacked arrangement in which the closest edge-to-edge distance of their π systems is only 3.34 Å. While the intrastack π-π interactions of the cofacial Pyr and diisoPDI should be large, given the close edge-to-edge interstack Pyr-Pyr, diisoPDI- diisoPDI, and Pyr-diisoPDI distances (Figure 4.1c), the interstack electronic interactions may also be sufficiently large to influence the formation, migration, and decay of CT excitons.

The Pyr-$C_5$PDI cocrystal is triclinic with space group P-1 and its interstack distance is 9.8 Å, while the Pyr-$C_5$PDI π-π stacking distance is 3.5 Å, both of which are very similar to the Pyr-diisoPDI cocrystal (Figure 4.1d). BFDH cell morphology calculations (Figure 4.6) once again show that the crystallographic *a*-axis is nearly parallel to the crystal long axis. Looking down the *a-b* crystallographic plane, the angle between the planes of adjacent D-A stacks is 47° (Figure 4.1e). In contrast to the Pyr-diisoPDI cocrystal, the Pyr-$C_5$PDI cocrystal has significantly greater edge-to-edge π-π distances of closest approach, where these distances are 6.43 Å for $C_5$PDI-$C_5$PDI, 6.12 Å for Pyr-$C_5$PDI, and 3.98 Å for Pyr-Pyr (Figure 4.1f). This implies that the photophysics of the Pyr-$C_5$PDI may be dominated by intrastack cofacial D-A interactions.

**4.3.2 Steady state absorption and emission**

Polarization-dependent steady-state absorption and PL spectra of both cocrystals are shown in Figure 4.2. The Pyr-diisoPDI cocrystal exhibits three distinct absorption bands at 460, 510, and 550 nm that are assigned to transitions of diisoPDI (Figure 4.2a).[152] Absorption peaks related only to Pyr are not observed because the molecule absorbs at 300-350 nm, which is outside of the range of the absorption measurement. The absorption in the 600-700 nm range is assigned to the CT

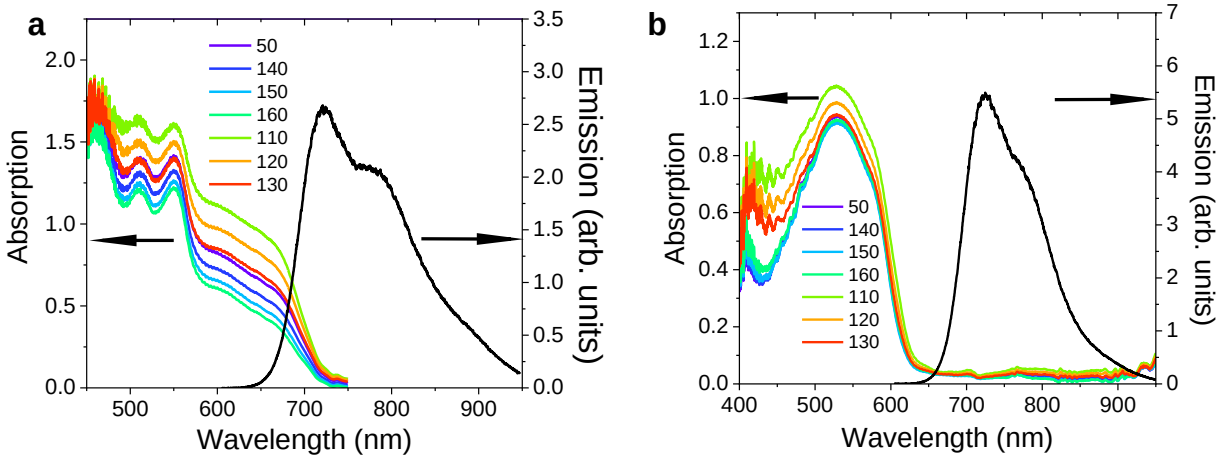


**Figure 4.2.** Steady-state absorption spectra at various polarizations with respect to the macroscopic crystal long axis (crystallographic *a*-axis), and unpolarized PL of (a) Pyr-diisoPDI cocrystal and (b) Pyr-$C_5$PDI cocrystal.

band of the cocrystal. The CT TDM lies along the direction normal to the π-stacking direction, so that the TDM makes an angle of ~40° relative to the crystallographic *a*-axis, which is parallel to the glass substrate surface. In contrast, the TDM of diisoPDI lies along its N-N axis,[64] which is also ~40 relative to the crystallographic *a*-axis. As the direction of the linearly polarized light relative to the *a*-axis is changed, both the diisoPDI and CT bands exhibit modest intensity changes (Figure 4.2a). Additional polarized absorption data are given in Figures 4.7-4.9. The unpolarized PL spectrum of the Pyr-diisoPDI cocrystal shows a maximum at 710 nm.

The Pyr-$C_5$PDI cocrystal displays a broad absorption band with a maximum at 530 nm and a shoulder at 577 nm that are both assigned to vibronic transitions of $C_5$PDI (Figure 4.2b).[64] The Pyr-$C_5$PDI CT band is not observed because its TDM is nearly perpendicular to the crystallographic *a*-axis, which is parallel to the glass substrate surface, and is thus nearly orthogonal to all orientations of the polarized light. The orientation of the $C_5$PDI TDM[64] is ~40° relative to the crystallographic *a*-axis, so that the $C_5$PDI absorption of the cocrystal exhibits a modest dependence of the polarized light orientation. The sharp absorption band at 410 nm may result from the red-shifted pyrene absorption in the solid state. Additional polarized absorption

data are given in Figures 4.10-4.12. The unpolarized PL spectrum of the Pyr-$C_5$PDI single crystal shows a band maximum at 710 nm, which is nearly identical to that of Pyr-diisoPDI. We assign this PL to the CT emission in both cocrystals.

### 4.3.3 Transient absorption microscopy

Polarization-dependent femtosecond transient absorption microscopy (fsTAM) was used to investigate the CT exciton dynamics of both the Pyr-diisoPDI and Pyr-$C_5$PDI cocrystals. The pump and probe focused spot sizes (FWHM) on the sample were 0.83 μm and 0.93 μm, with Gaussian beam shapes (Figure 4.13). The total instrument response function (IRF) was 300 fs. The spectral features of Pyr-diisoPDI differ when the probe polarization is parallel or perpendicular to the *a*-axis of the cocrystal. After selective photoexcitation of diisoPDI at 540 nm, an absorption peak appears at 710 nm within the IRF when the probe is perpendicular to the crystallographic *a*-axis that is assigned to diisoPDI$^{\bullet-}$ within the Pyr$^{\bullet+}$-diisoPDI$^{\bullet-}$ exciton (Figure 4.3a).[77] In contrast, when the probe direction is parallel to the crystal *a*-axis, the diisoPDI$^{\bullet-}$ positive absorption feature broadens. Both spectra decay over the ~8 ns time window of the pump-probe experiment. The spectral shape resembles the solution phase spectrum of PDI$^{\bullet-}$ observed previously.[77] Pyr$^{\bullet+}$ is not observed because the spectral feature would be around 400 nm,[153] which is outside the wavelength window of the experiment. The sharper diisoPDI$^{\bullet-}$ absorption observed for the perpendicular probe orientation is a consequence of cancellation of part of the diisoPDI$^{\bullet-}$ absorption by the ground state bleach of the CT absorption band at 600-700nm (Figure 4.3a). When the probe is parallel to the crystallographic *a*-axis, the ground state bleach of the CT band is diminished and thus, the diisoPDI$^{\bullet-}$ absorption appears more symmetric (Figure 4.3b).

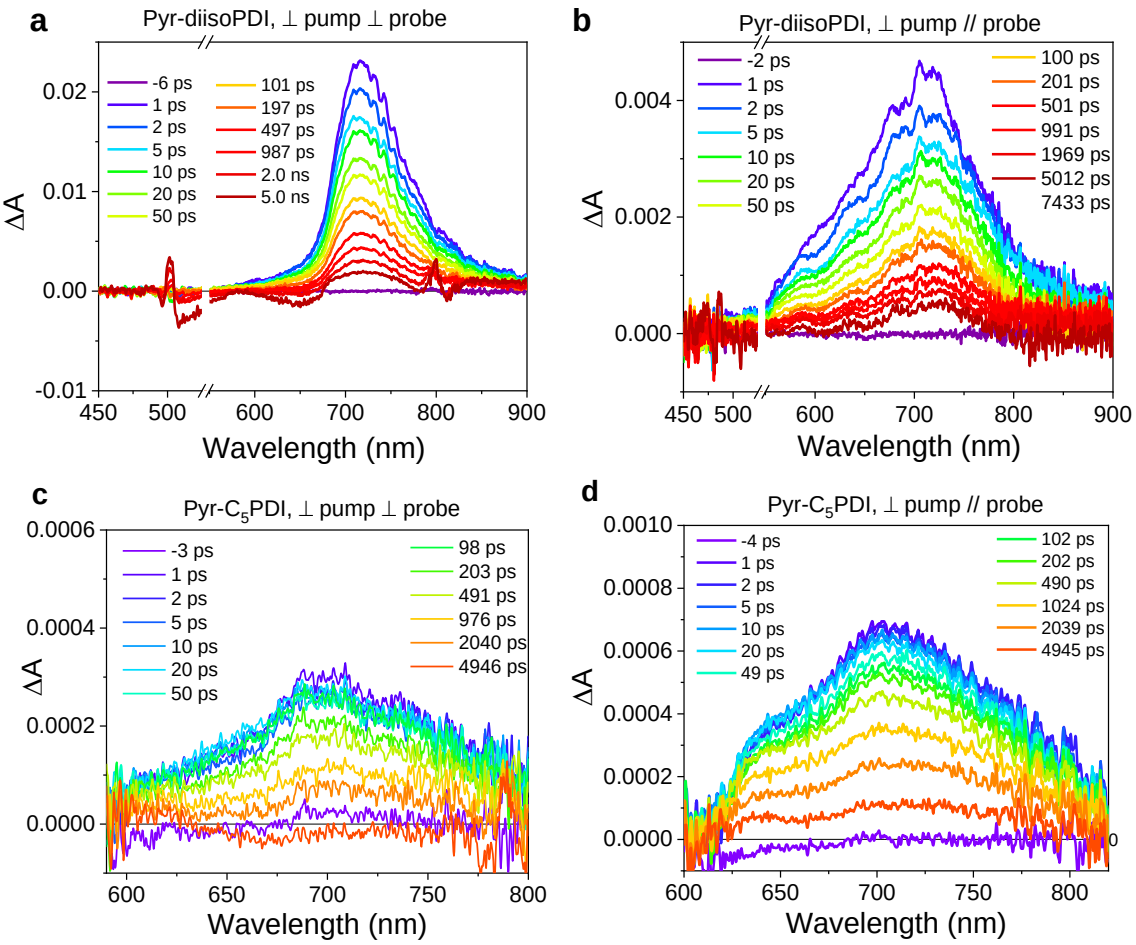


**Figure 4.3.** FsTAM spectra of the Pyr-diisoPDI cocrystal with probe polarized (a) perpendicular or (b) parallel to crystallographic *a*-axis and of the Pyr-$C_5$PDI cocrystal with probe polarized (c) perpendicular or (d) parallel to crystallographic *a*-axis.

The fsTAM spectra of the Pyr-$C_5$PDI cocrystal are only slightly probe-polarization dependent. After selective excitation of $C_5$PDI, formation of the $Pyr^{\bullet+}$-$C_5PDI^{\bullet-}$ CT exciton **is** observed as a broadened positive absorption band at 700 nm due to $C_5PDI^{\bullet-}$ when the probe is perpendicular to the *a*-axis of the crystal. The $C_5PDI^{\bullet-}$ feature decays within the 8 ns pump-probe delay window (Figure 4.3c). Similar spectral features are observed when the probe is parallel to the crystal long axis. $C_5PDI^{\bullet-}$ is observed at 700 nm along with a shoulder at 640 nm (Figure 4.3d).

## 4.4 DISCUSSION

### 4.4.1 CT exciton diffusion and decay dynamics

Our data show that the kinetics of CT exciton diffusion in the Pyr-diisoPDI cocrystal depend on the pump polarization relative to the crystallographic *a*-axis. When the pump is polarized perpendicular to the crystallographic *a*-axis, the TDM of diisoPDI within the Pyr-diisoPDI cocrystal is nearly parallel to the polarization direction of the light (Figure 4.1a), so maximal light absorption occurs. The decay kinetics are best modeled using a bimolecular, one-dimensional CT exciton annihilation process:

$$\frac{d[\mathrm{CT}]}{dt} = -k_2[\mathrm{CT}]^2 \qquad \text{(Eqn. 4.1)}$$

which for a Smoluchowski-type time-dependent rate coefficient $k_2 \propto t^{-1/2}$ has the analytical solution:[118]

$$[\mathrm{CT}] = ([CT]_0^{-1} + 2C\sqrt{t})^{-1} \qquad \text{(Eqn. 4.2)}$$

where *C* is a composite constant discussed below. This model fits the data well for the ~8 ns time window of the pump-probe experiment (Figure 4.4a).

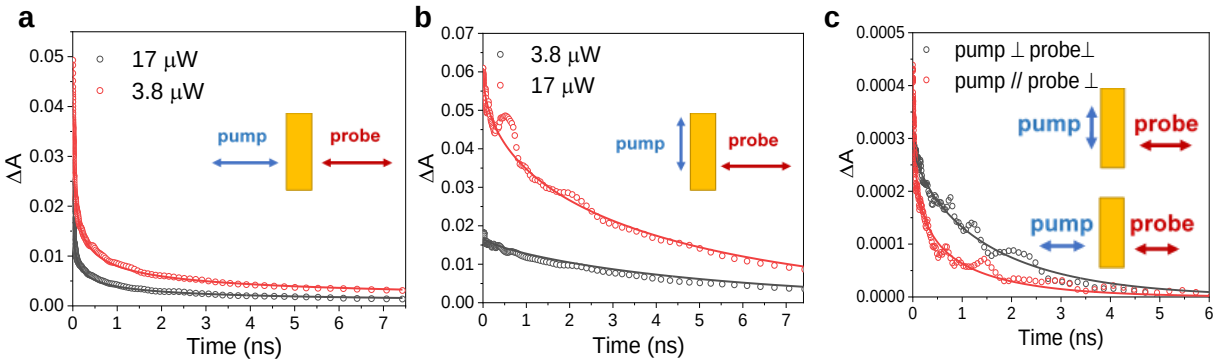


**Figure 4.4.** (a) Kinetic fits to a bimolecular, one-dimensional decay model at two different pump fluences for Pyr-diisoPDI with the indicated pump and probe polarizations. (b) Kinetic fits to a bimolecular, one-dimensional decay and first order decay model at two different pump fluences for the Pyr-diisoPDI cocrystal with the indicated pump and probe polarizations. Oscillations in the data are due to acoustic phonons produced in the cocrystal at higher pump powers. (c) Kinetic fits to a bimolecular, one-dimensional decay and first order decay model in the Pyr-$C_5$PDI cocrystal with the indicated pump and probe polarizations. The pump energy is 2.3 μW for both polarizations. Oscillations in the data are due to acoustic phonons produced in the cocrystal at higher pump powers.

In contrast, when the pump is polarized parallel to the crystallographic *a*-axis, the TDM of diisoPDI within the Pyr-diisoPDI cocrystal is nearly perpendicular to the polarization direction of the pump diminishing the absorbance. The kinetic model that best describes the data requires the addition of a first order decay component to eqn. 4.1:

$$\frac{d[\mathrm{CT}]}{dt} = -k_1[\mathrm{CT}] - k_2[\mathrm{CT}]^2 \qquad \text{(Eqn. 4.3)}$$

The analytical solution[117] to eqn. 4.3 as detailed in the ESI is:

$$[\mathrm{CT}] = \frac{[\mathrm{CT}]_0\sqrt{k_1}e^{-k_1 t}}{\sqrt{k_1}+[\mathrm{CT}]_0 C\sqrt{\pi}-[\mathrm{CT}]_0 C\sqrt{\pi}\times erfc\left(\sqrt{k_1 t}\right)} \qquad \text{(Eqn. 4.4)}$$

This model fits the data well for the ~8 ns time window of the pump-probe experiment (Figure 4.4b).

Charge recombination of the CT exciton begins to compete with the CT biexciton annihilation process when the pump polarization changes because irradiating the crystal with a parallel polarized pump reduces the number of absorbed photons and leads to fewer initial CT excitons

produced (Figure 4.4b). This leads to a diminished CT biexciton annihilation rate and increased contribution of charge recombination to the decay kinetics. Indeed, the effects of the concentration of CT excitons on the kinetics can be seen in both pump polarizations when the incident pump power is decreased from 17 μW to 3.8 μW (Figures 4.4a and 4.4b). The lower concentration of CT excitons causes the nonlinear contribution in eqn. 3 to diminish, leading to slower decay kinetics and a larger contribution of first-order geminate charge recombination.

The TDM of $C_5$PDI in the Pyr-$C_5$PDI cocrystal is rotated by ~40° relative to the crystallographic *a*-axis, so that the CT exciton dynamics are nearly independent of the pump polarization direction. The CT exciton dynamics in the Pyr-$C_5$PDI cocrystal are best modeled using eqns. 4.3 and 4.4, regardless of pump polarization direction. The Pyr-$C_5$PDI transient absorption data and kinetic fits using eqn. 4.4 are shown in Figure 4.4c. The presence of a significant first-order decay term at both pump polarizations indicates there is a significant contribution from the CT exciton recombination in addition to the dominant CT biexciton annihilation process. This is reasonable because interstack CT exciton diffusion is strongly diminished by the long $C_5$PDI- $C_5$PDI and Pyr-Pyr edge-to-edge distances (Figure 4.1f), relative to the corresponding distances in the Pyr-diisoPDI cocrystal (see below).

The bimolecular annihilation rate constant, $k_2$, can be cast as a one-dimensional diffusion coefficient using:[117]

$$k_2 = \frac{1}{R_{1D}N_0}\sqrt{\frac{8D_{1D}}{\pi t}} = \frac{C}{\sqrt{t}}, C = \frac{1}{R_{1D}N_0}\sqrt{\frac{8D_{1D}}{\pi}} \qquad \text{(Eqn. 4.5)}$$

Solving for the value of $C$ in eqn. 4.5, we calculated the CT exciton diffusion coefficients for both Pyr-diisoPDI and Pyr-$C_5$PDI, which are listed in Table 4.1. The details of the calculations for the diffusion coefficients from *C* and ΔA are given in Section 4.6 (eqns. 4.6-4.17). While the mobility

of the CT exciton in a donor-acceptor cocrystal can be described by a hopping rate,[152] the movement of excitons in crystalline pentacene and similar materials has also been modeled by a diffusion coefficient.[117, 154-156] It is known that CT excitons in mixed-stack donor-acceptor systems diffuse via a superexchange mechanism, where the hole on $D^{\bullet+}$ tunnels to the next D through a virtual singlet state, $^{1*}A$.[49, 152, 157-160] A similar mechanism for tunneling of $A^{\bullet-}$ is possible, but less likely in the cases presented here because the virtual $^{1*}D$ is much higher in energy.

**Table 4.1.** Rate constants and diffusion coefficients for Pyr-diisoPDI and Pyr-$C_5$PDI cocrystals at different pump polarizations.

| Cocrystal | $k_1$ ($ps^{-1}$) | $k_2$ ($OD^{-1}\cdot ps^{-1/2}$) | $D$ ($cm^2/s$) |
|---|---|---|---|
| Pyr-diisoPDI, ⊥ pump | - | 6.86 ± 0.05 | $2.16 \times 10^{-4}$ |
| Pyr-diisoPDI, \|\| pump | $1.57 \pm 0.08 \times 10^{-4}$ | 0.137 ± 0.004 | $3.70 \times 10^{-4}$ |
| Pyr-$C_5$PDI, ⊥ pump | $5.1 \pm 0.3 \times 10^{-4}$ | 23 ± 1 | $1.82 \times 10^{-6}$ |
| Pyr-$C_5$PDI, \|\| pump | $6.3 \pm 0.5 \times 10^{-4}$ | 119 ± 2 | $5.05 \times 10^{-6}$ |

What aspect of the Pyr-diisoPDI cocrystal structure leads to a 100-fold increase in its CT exciton diffusion coefficient relative to that of the Pyr-$C_5$PDI cocrystal? Photoexciting the Pyr-diisoPDI cocrystal may lead to efficient charge hopping or delocalization because the diisoPDI-diisoPDI and Pyr-Pyr edge-to-edge distances are close enough to ensure interstack wavefunction overlap (Figure 4.1c). Using EPR and ENDOR spectroscopy, we demonstrated earlier that the radical anions of PDI dimers and trimers with orthogonal core π-systems separated by ~3.2 Å have charge hopping rates that are $>>10^7$ $s^{-1}$,[161] so that the nearly coplanar diisoPDI π-systems in the Pyr-diisoPDI cocrystal should also have a comparable or higher hopping rate. Dispersing the charge in the CT exciton will reduce the Coulomb attraction of the CT state and the probability of charge recombination.[162] Moreover, charge dispersal should result in additional electronic coupling pathways for CT exciton diffusion via the superexchange mechanism outlined above.

Thus, CT exciton diffusion becomes more favorable, even though CT exciton migration remains largely one-dimensional**.** In contrast, the Pyr-$C_5$PDI cofacial π-stacks in the cocrystal structure are positioned farther apart, so that charge hopping or delocalization between adjacent π-stacks is unlikely, thus confining CT exciton diffusion to the individual π-stacks. Thus, the fact that the CT exciton diffusion coefficient for the Pyr-diisoPDI cocrystal is almost 100 times larger than that of the Pyr-$C_5$PDI cocrystal is consistent with the cocrystal morphologies, although one cannot completely discount some contribution from differences in the density of CT exciton trap sites.

## 4.5 CONCLUSIONS

Two cocrystals, Pyr-diisoPDI and Pyr-$C_5$PDI, were characterized using X-ray crystallography, steady-state absorption and emission microscopy and fsTAM. The fsTAM spectra of both cocrystals indicates the formation of $Pyr^{\bullet+}$-$diisoPDI^{\bullet-}$ and $Pyr^{\bullet+}$-$C_5PDI^{\bullet-}$ CT excitons, whose kinetics were modeled using a one-dimensional CT exciton annihilation model with the addition of a first-order decay term in certain cases. It was determined that one-dimensional CT exciton diffusion occurs in the π-stacking direction in both Pyr-diisoPDI and Pyr-$C_5$PDI cocrystals. The 100-fold increase in the CT exciton diffusion coefficient of the Pyr-diisoPDI cocrystal relative to that of the Pyr-$C_5$PDI cocrystal is attributed to charge dispersal within the CT exciton in the former case. These results illustrate how D-A cocrystal morphology strongly influences CT exciton diffusion and provide insight into optimizing D-A-cocrystals for optoelectronic applications.

## 4.6 SUPPLEMENTARY INFORMATION

### 4.6.1 Crystal Growth and Structure Determination

The Pyr-$C_5$PDI cocrystal was grown from 4 mL of 3.75 mM pyrene and 3.75 mM $C_5$PDI in $CHCl_3$. This solution was pipetted into culture tubes (Fisher brand, 6×50 mm lime glass), which were placed in a 20 mL glass vial filled with ~8 mL of MeOH, and the single cocrystals were

grown by vapor diffusion. Similarly, the Pyr-diisoPDI cocrystal was grown from 4 mM pyrene and 4 mL of 4 mM diisoPDI in $CHCl_3$ using the same techniques. Once the crystals were visible by eye, they were drop cast from the mother solution onto a glass slide and their excited-state properties were measured.

### 4.6.2 Single Crystal X-ray Diffraction

A suitable single crystal of Pyr-$C_5$PDI with dimensions of 0.049×0.071×0.268 $mm^3$ was mounted on a loop with paratone oil on an XtaLAB Synergy diffractometer equipped with a micro-focus sealed X-ray tube PhotonJet (Cu) X-ray source and a Hybrid Pixel Array Detector(HyPix) detector. The temperature of the crystal was controlled at 100.0 K with an Oxford Cryosystems low-temperature device. Data reduction was performed with CrysAlisPro software using an empirical absorption correction. The crystal under investigation was found to be non-merohedrally twinned. The orientation matrices for the two components were identified using the program CrysAlisPro (Rigaku Oxford Diffraction, 2019). The exact twin matrix identified by the integration program was found to be (-0.9996 0.0001 -0.0007 -0.0023 -0.9991 0.0022 -0.4445 -0.0238 1.0001). The second domain is rotated from first domain by -179.9126% about the reciprocal lattice c axis. An hklf5 file was used in all refinements. The structure was solved using direct methods with only the non-overlapping reflections of component 1. The twin fraction refined to a value of 0.413(2).The structure was solved using the XS[163] structure solution program using direct methods and by using Olex2[164] as the graphical interface. The model was refined with the XL[165] refinement package using Least Squares minimization. The final structure has been submitted to the Cambridge Crystallographic Data Centre: CCDC 2092900.

Crystal Structure Data for Pyr-$C_5$PDI:$C_{100}H_{80}N_4O_8$ ($M$ =1437.75 g/mol): triclinic, space group P-1 (no. 2), $a$ = 7.3795(10) Å, $b$ = 9.5328(2) Å, $c$ = 26.1396(6) Å, $\alpha$ = 89.271(2)°, $\beta$ = 86.498(2)°,

$\gamma$ = 84.068(2)°, $V$ = 1825.55(6) Å$^3$, $Z$ = 1, $T$ = 100.0 K, μ(CuKα) = 0.7659 mm$^{-1}$, *Dcalc* = 1.333 g/cm$^3$, 10696 reflections measured (6.776° ≤ 2Θ ≤ 155.016°), 7547 unique ($R_{int}$ = merged, $R_{sigma}$ = 0.0075) which were used in all calculations. The final $R_1$ was 0.0901 (I > 2σ(I)) and $wR_2$ was 0.2825 (all data).

A suitable single crystal of Pyr-diisoPDI with dimensions of 0.064×0.098×0.255 mm$^3$ was mounted on a loop with paratone oil on the diffractometer system described above, and the diffraction data was collected at 100.1 K. The structure was solved as described above for the Pyr-$C_5$PDI crystal. Squeeze was used to remove disordered chloroform solvent molecules. The pyrene moiety (C48-63) displayed disorder and was modeled over two positions. Restraint RIGU was applied to moiety C48-C63 and C48A-C63A. The final structure has been submitted to the Cambridge Crystallographic Data Centre: CCDC 2092901.

Crystal Structure Data for Pyr-diisoPDI: $C_{64}H_{51}N_2O_4$ ($M$ = 912.07 g/mol): monoclinic, space group P2$_1$/c, $a$ = 8.6684(3) Å, $b$ = 19.1525(5) Å, $c$ = 30.3884(8) Å, $\alpha$ = 90°, $\beta$ = 92.739(3)°, $\gamma$ = 90°, $V$ = 5039.4(3) Å$^3$, $Z$ = 4, $T$ = 100.0 K, μ(CuKα) = 0.648 mm$^{-1}$, *Dcalc* = 1.202 g/cm$^3$, 32028 reflections measured (7.432° ≤ 2Θ ≤ 153.554°), 10136 unique ($R_{int}$ = 0.0329, $R_{sigma}$ = 0.0249) which were used in all calculations. The final $R_1$ was 0.1070 (I > 2σ(I)) and $wR_2$ was 0.3059 (all data).

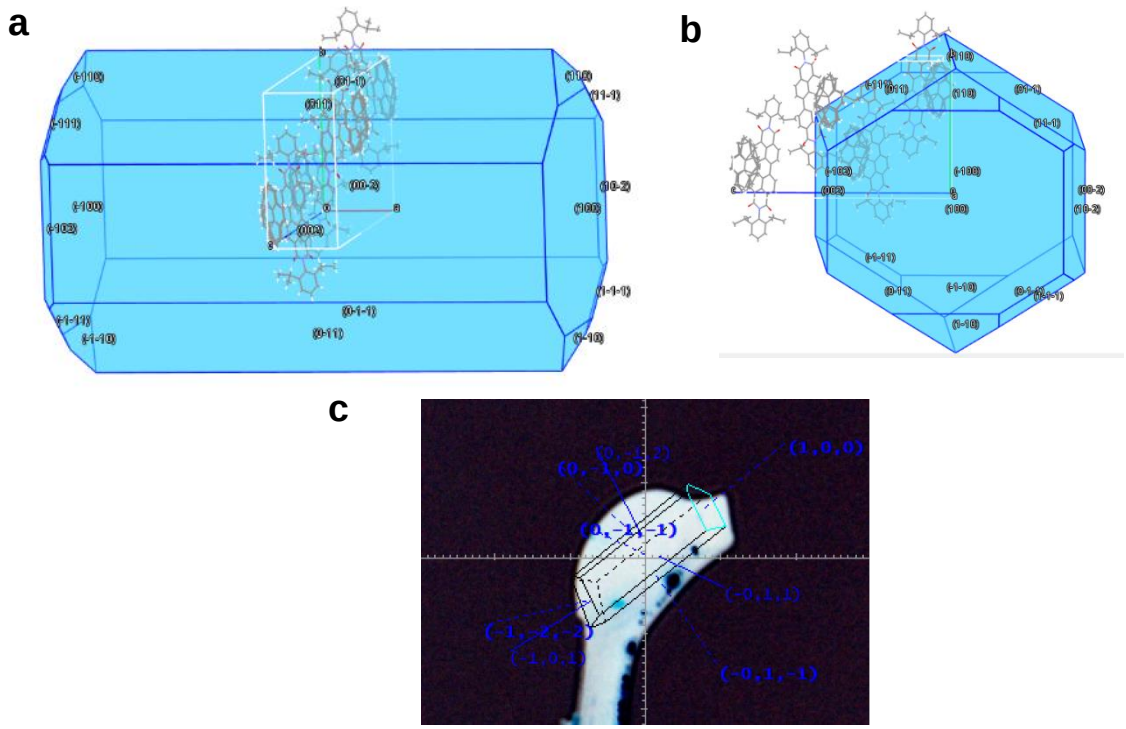


**Figure 4.5.** BFDH calculations were completed in Mercury for Pyr-diisoPDI cocrystal. (a) View of the crystal along the (002) axis shows the molecules stack with their transition dipole moments perpendicular to the long axis of the crystal. (b) View of the crystal along the (100) axis shows a degree of interstack overlap, though the planes of the molecules are not perfectly cofacial with the axis of the crystal. (c) Manual face indexing of the mounted single crystal that was diffracted shows reasonable agreement with the BFDH calculated structures.

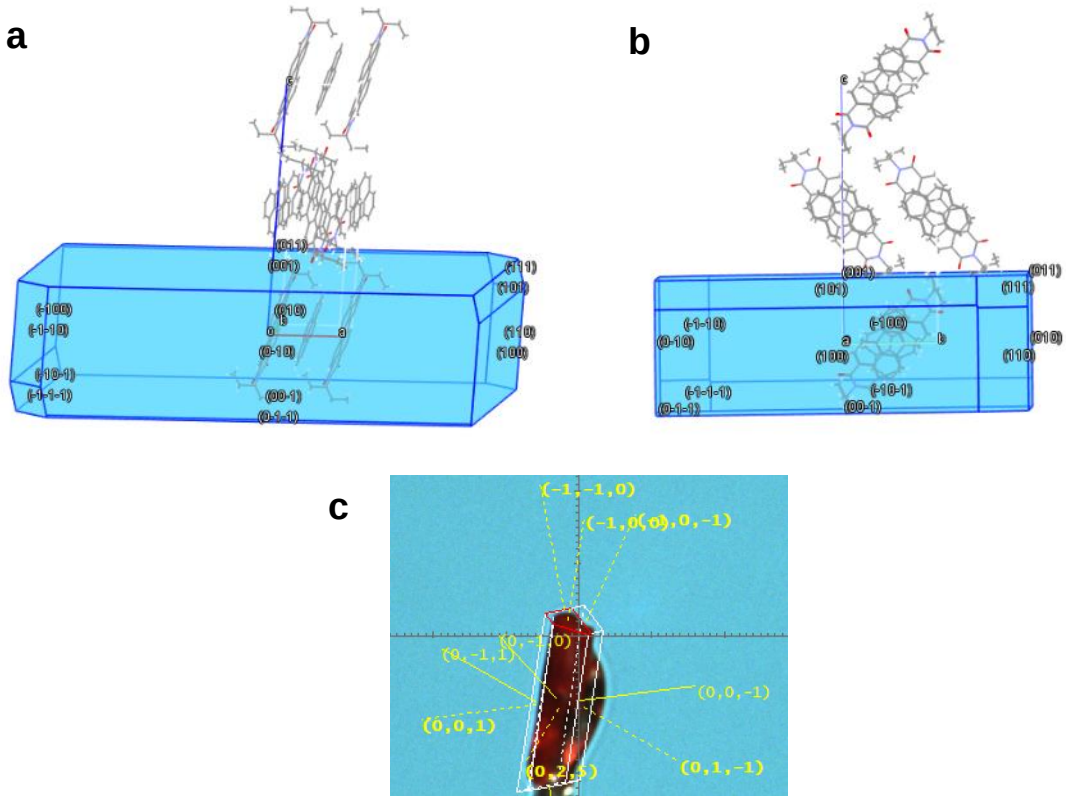


**Figure 4.6.** BFDH calculations were completed in Mercury for Pyr-$C_5$PDI cocrystal. (a) View of the crystal along the (010) axis shows the molecules stack with their transition dipole moments perpendicular to the long axis of the crystal. (b) View of the crystal along the (100) axis shows cleanly segregated stacks, with the planes of the molecules perfectly cofacial with the axis of the crystal. (c) Manual face indexing of the mounted single crystal that was diffracted shows reasonable agreement with the BFDH calculated structures.

### 4.6.3 Steady-state Absorption and Emission Microscopy

Steady-state absorption spectra on the single crystals were obtained using an adapted commercial epi-illumination microscope (Nikon Ti-U) using the white light continuum probe beam from the femtosecond apparatus (see below). The white light source was focused on the sample with a 60× objective lens (Nikon, NA= 0.70), and the transmitted light was collected and recollimated with another 50× objective lens (Nikon, NA= 0.55) mounted over the sample. The collimated output was directed to a home-built spectrometer and the spectrally dispersed signal was recorded with a fast line-scan camera (OctoPlus, Teledyne e2v). To obtain an absorption spectrum, a reference transmission was first taken with the beam focused on the bare glass substrate, and the signal transmission was measured on the single crystal. The polarization of the beam was controlled with a broadband half-wave plate (HWP) before the microscope to obtain the steady-state absorption spectra at different polarizations.

Steady-state emission spectra were measured using a similar epi-illumination microscope (Nikon Ti-U), excited by a 532 nm continuous-wave laser (Spectra-Physics) beam. A 40× magnification objective lens (Nikon, NA = 0.60) was used both to focus the incident beam onto a single crystal and to collect the emitted light. The emitted light was then sent into an Acton spectrograph (Princeton Instruments) equipped with a PIXIS 400BR CCD Camera (Princeton Instruments). A long-pass filter was used to block the scattered excitation beam within the signal.

### 4.6.4 Polarized Absorption Plots

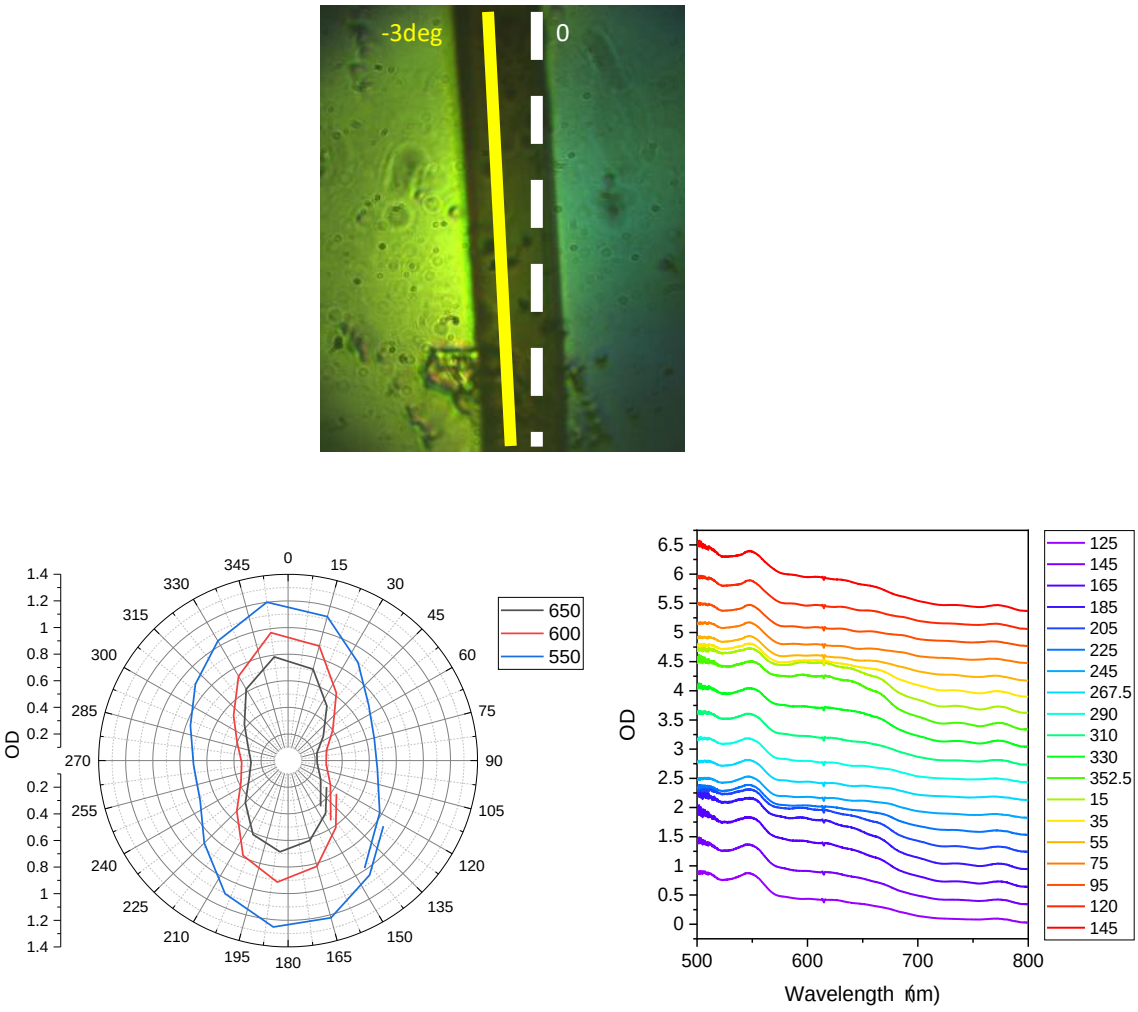


**Figure 4.7.** Pyr-diisoPDI measured with probe at various polarizations.

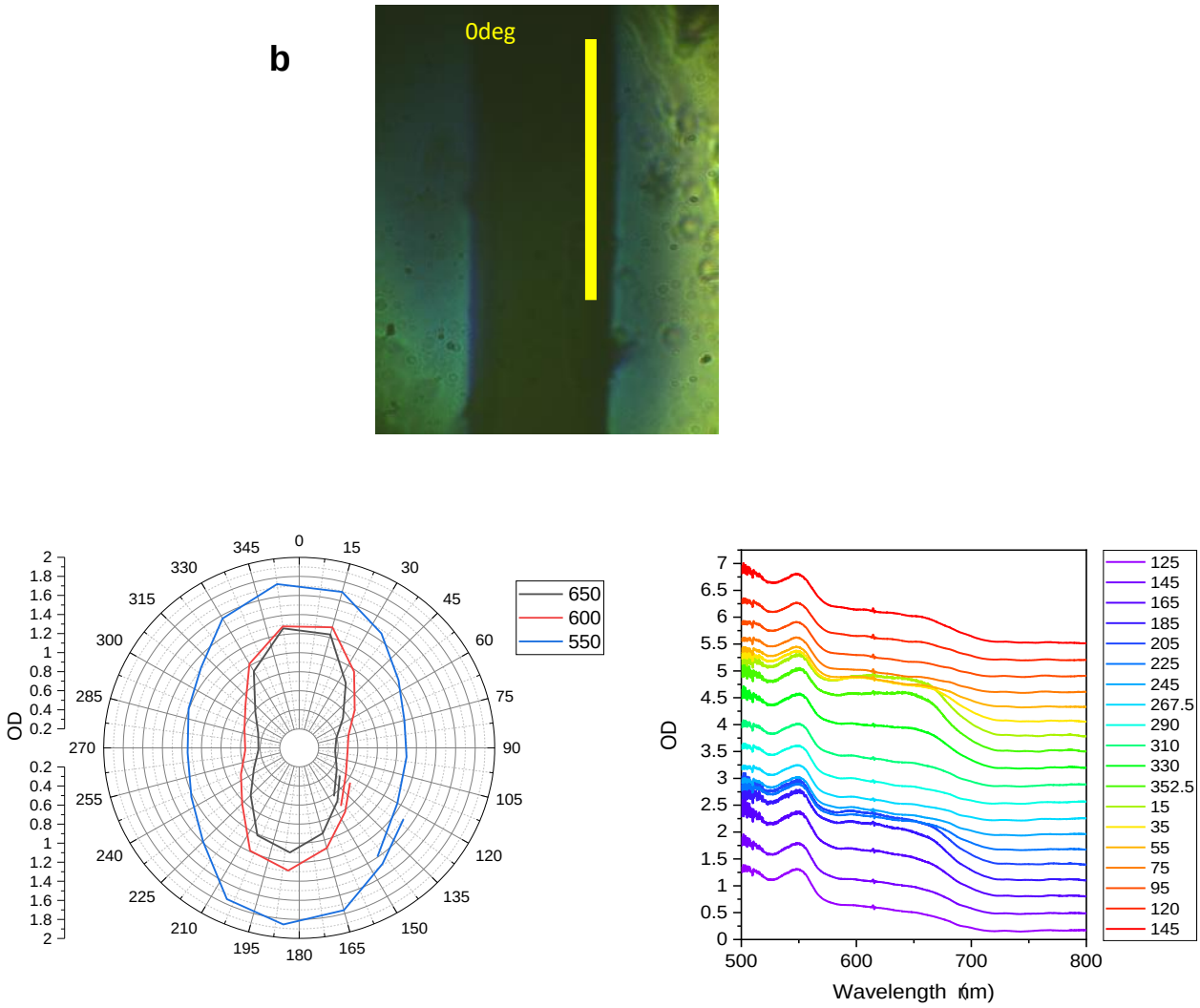


**Figure 4.8.** Pyr-diisoPDI measured with probe at various polarizations.

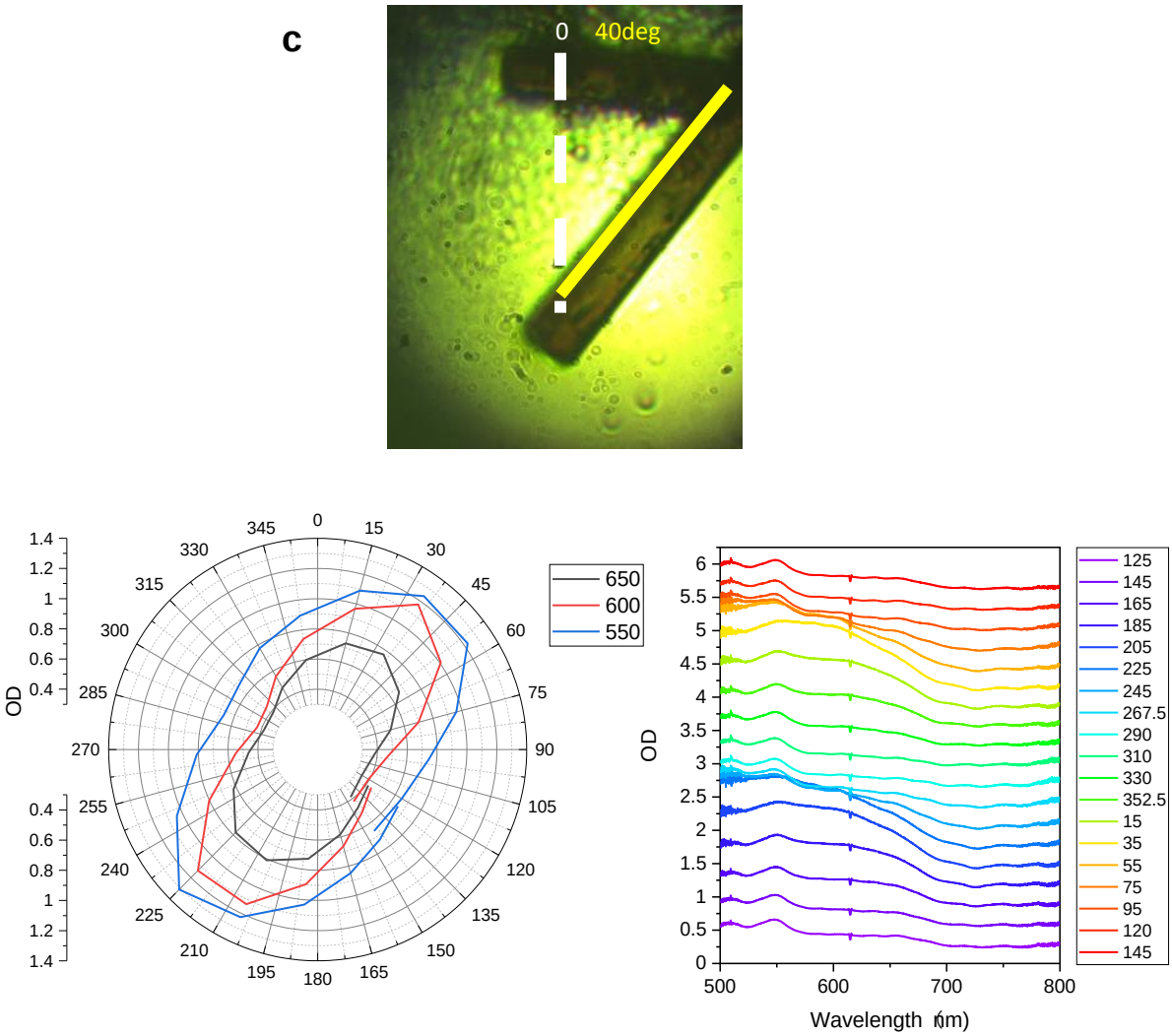


**Figure 4.9.** Pyr-diisoPDI measured with probe at various polarizations.

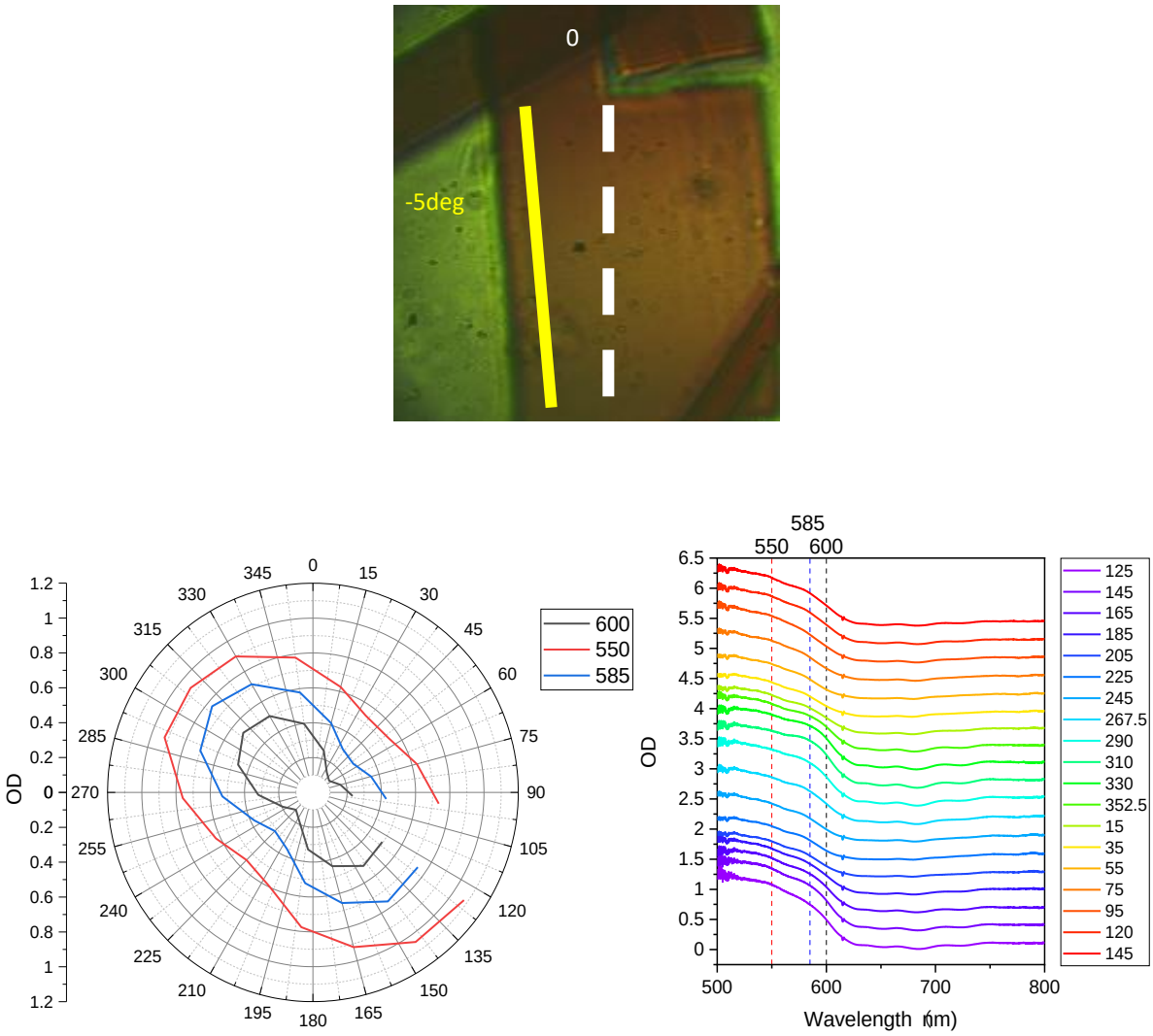


**Figure 4.10.** Pyr-$C_5$PDI measured with probe at various polarizations.

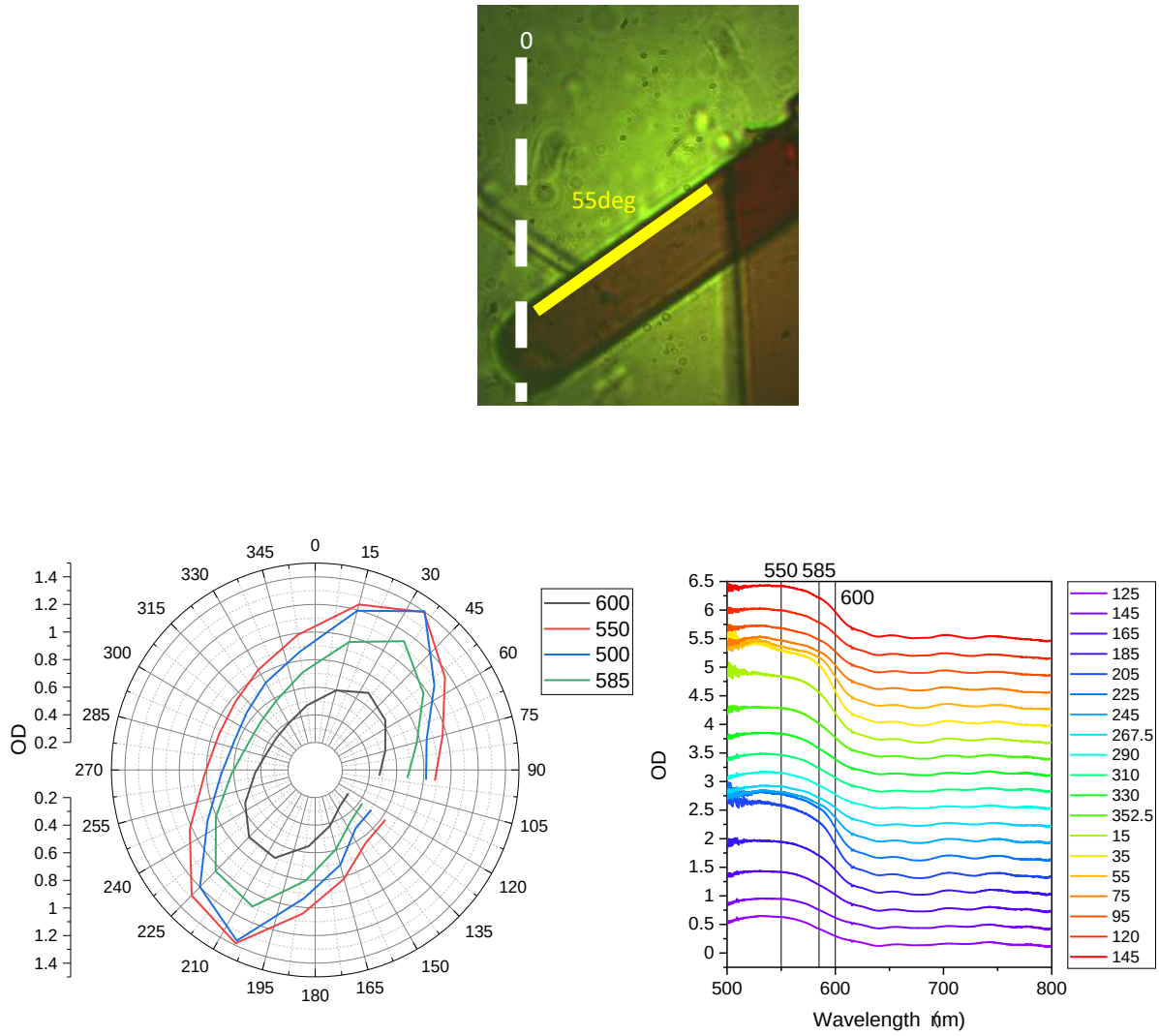


**Figure 4.11.** Pyr-$C_5$PDI measured with probe at various polarizations.

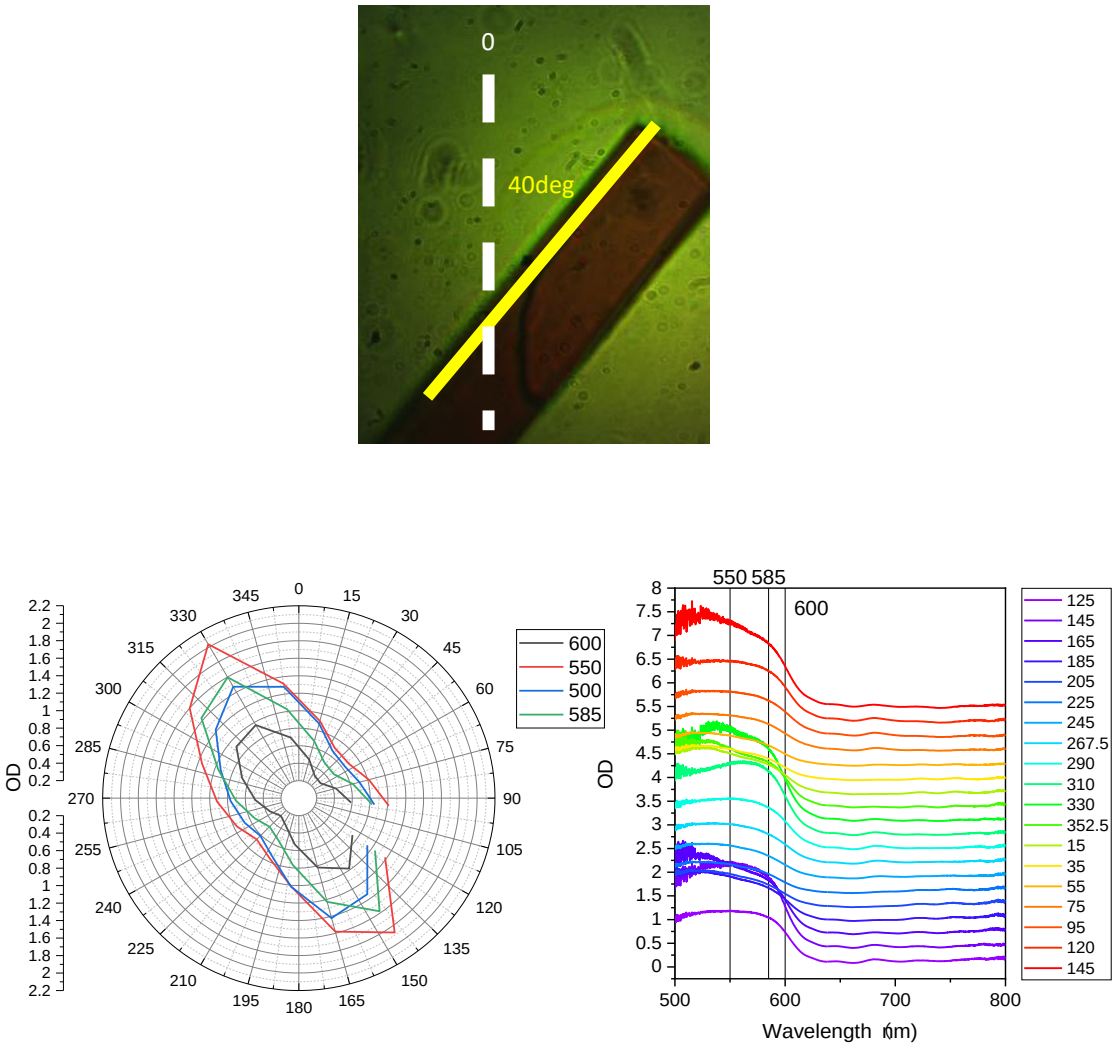


**Figure 4.12.** Pyr-$C_5$PDI measured with probe at various polarizations.

### 4.6.5 Femtosecond Transient Absorption Microscopy

Femtosecond transient absorption microscopy (fsTAM) was performed as follows: The 1040 nm fundamental output (> 8 W, < 400 fs, 200 kHz repetition rate) of a commercial amplified laser system (Spirit One, Spectra-Physics) was down-counted to 100 kHz with the integrated pulse picker, and then divided with a beam splitter (BS) into two beam paths. One beam (probe path) was sent to a double-pass linear delay line, and then focused into a 10 mm thick undoped yttrium aluminum garnet (YAG) crystal for white light continuum generation. The other fraction of the 1040 nm fundamental beam was used to drive a collinear optical parametric amplifier (Spirit-OPA-8, Spectra-Physics), which generated the visible pump pulses. The visible pump pulses were modulated at 50 kHz with an electro-optic amplitude modulator (EOAM-NR-C4, Thorlabs), which was synchronized to the fundamental laser output. The pump was converted to a circularly polarized beam before entering the modulator, and the modulated output pump beam was routed through a linear polarizer. This is followed by dispersion compensation of the modulated pump pulses using a prism compressor consisting of two prisms. The pump and probe beams were co-axially combined using a 50:50 BS and sent into the same microscope setup, spectrometer, and camera used for steady-state absorption measurements described above. The polarizations of the pump and the probe beams were controlled independently using two HWPs. The pump and probe focused spot sizes (FWHM) on the sample were 0.83 μm and 0.93 μm, with Gaussian beam shapes (Figure S5). The total instrument response function (IRF) was 400-600 fs.

### 4.6.6 Pump and probe spot sizes

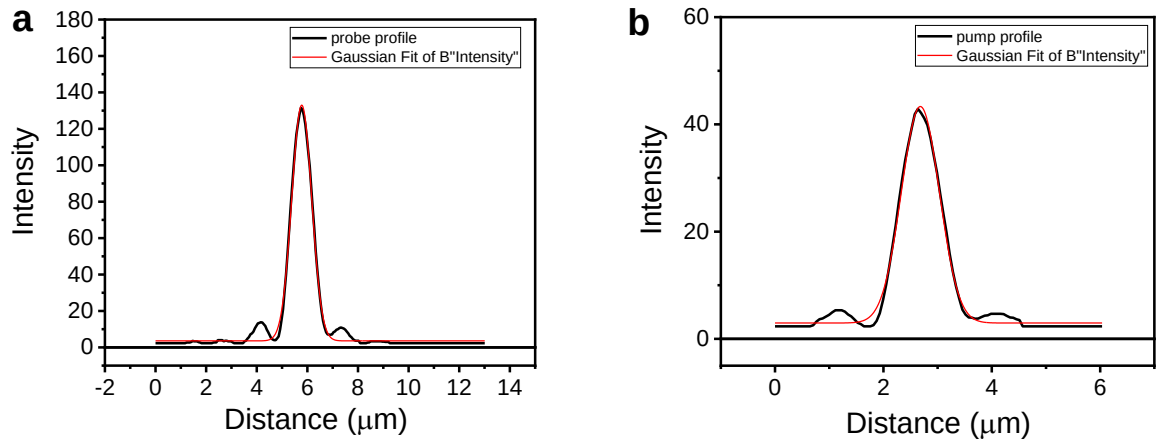


**Figure 4.13. Gaussian fits for (a) probe and (b) pump spot sizes. Objective lens: Nikon (Plan fluor, ELWD, 60X/0.7)**

### 4.6.7 Calculation of excitation density

$$\xi = \frac{N_p}{V} = \frac{\lambda \times P \times (1 - 10^{-A})}{h \times c \times f \times \pi r^2 t}$$

**Table 4.2.** Excitation density parameters.

| $\lambda$ (nm) | $P$ (μW) | $A$ (OD) | $f$ (kHz) | $r$ (μm) | $t$ (μm) |
|---|---|---|---|---|---|
| 540 | 17 | 0.25 | 50 | 0.46 | 2 |

The excitation density is the number of photons ($N_p$) in the excitation volume ($V$) per pulse. The values $\lambda$, $P$, $A$, $f$, $r$, $t$ are the excitation wavelength, pump power, absorbance at the excitation wavelength, pump repetition rate, radius of the probe beam, and thickness of the crystal. Values $h$ and $c$ are Planck's constant and the speed of light in a vacuum. For the experiment at these parameters the excitation density is: $3.04 \times 10^{20}$ cm$^{-3}$.

### 4.6.8 Calculation of diffusion coefficients

To calculate the bimolecular rate constant, the data were fit to either one of the following kinetic models:

1. CT excitons annihilate through one-dimensional diffusion:

$$\frac{d[\mathrm{CT}]}{dt} = k_2[\mathrm{CT}]^2 \qquad \text{(Eqn. 4.6)}$$

Where $[\mathrm{CT}]$ is the concentration of CT excitons and $k_2$is the rate coefficient of diffusion-controlled CT biexciton annihilation. Assuming one-dimensional diffusion of CT excitons and that annihilation is effectively instantaneous upon contact, $k_2$ may be related to the one-dimensional diffusion coefficient $D_{1D}$, annihilation radius $R_{1D}$ of CT excitons, and the average molecular density throughout the system $N_0$ by[117]:

$$k_2 = \frac{1}{R_{1D}N_0}\sqrt{\frac{8D_{1D}}{\pi t}} = \frac{C}{\sqrt{t}}, C = \frac{1}{R_{1D}N_0}\sqrt{\frac{8D_{1D}}{\pi}} \qquad \text{(Eqn. 4.7)}$$

With $N_0$ calculated by:

$$N_0 = \frac{\rho \times N_A}{M_w} \qquad \text{(Eqn. 4.8)}$$

where $\rho$ is the density of the unit cell, $N_A$ is Avogadro's number, $M_w$ is the molecular weight of the unit cell.

Solving the differential equation (4.6) with $k_2$ expressed as (4.7) yields[166]:

$$[\mathrm{CT}] = \left([CT]_0^{-1} + 2C\sqrt{t}\right)^{-1} \qquad \text{(Eqn. 4.9)}$$

$[\mathrm{CT}]_0$ is the initial concentration of CT excitons after excitation.

With TAM spectra, the concentration of CT excitons [CT] at any given time *t* after can be expressed by:

$$[\mathrm{CT}] = \frac{\Delta\mathrm{OD}}{\Delta\mathrm{OD}_0} \times [\mathrm{CT}]_0 \qquad \text{(Eqn. 4.10)}$$

Where $\Delta\mathrm{OD}$ and $\Delta\mathrm{OD}_0$ are the TAM signal at time *t* and at time zero, respectively. Assuming every photon absorbed by the system converts to a CT exciton, $[\mathrm{CT}]_0$ reduces to the excitation density $\xi$. The expression for $\xi$ is:

$$\xi = \frac{N_p}{V} = \frac{\lambda \times P \times (1-10^{-A})}{h \times c \times f \times \pi r^2 t} \qquad \text{(Eqn. 4.11)}$$

$\lambda$ is the excitation wavelength, $P$ the pump power, $f$ the repetition rate, $r$ the spot radius, $t$ the thickness, and $A$ the absorbance at the excitation wavelength and polarization as measured with steady-state absorption microscopy.

Plugging eqns (4.11) and (4.12) into (4.10), the evolution of TAM signal ΔOD can be expressed as:

$$\Delta\mathrm{OD} = (\Delta\mathrm{OD}_0{}^{-1} + \frac{2\xi C}{\Delta\mathrm{OD}_0}\sqrt{t})^{-1} \qquad \text{(Eqn. 4.12)}$$

TAM spectrum at 540 nm was fitted to equation (4.9) to obtain the *C* value, and finally equation (4.7) can be solved for the value of $D_{1D}$:

$$D_{1D} = (N_0 \times R_0 \times C)^2 \times \frac{\pi}{8} \qquad \text{(Eqn. 4.13)}$$

2. CT excitons annihilate through one-dimensional diffusion with a first order decay:

$$\frac{d[\mathrm{CT}]}{dt} = -k_1[\mathrm{CT}] - k_2[\mathrm{CT}]^2 \qquad \text{(Eqn. 4.14)}$$

Where $k_1$ is the unimolecular rate coefficient associated with the first-order CT exciton decay and $k_2$is the rate coefficient of diffusion-controlled CT biexciton annihilation.

Following equation 4.7, the kinetic model is written as:

$$\frac{d[\mathrm{CT}]}{dt} = -k_1[\mathrm{CT}] - \frac{C}{\sqrt{t}}[\mathrm{CT}]^2 \qquad \text{(Eqn. 4.15)}$$

The analytical solution to equation 4.15 is:

$$[\mathrm{CT}] = \frac{\sqrt{A}\times D\times e^{-At}}{\sqrt{A}+CD\sqrt{\pi}-CD\sqrt{\pi}\times erfc(\sqrt{At})} \qquad \text{(Eqn. 4.16)}$$

where $D = [\mathrm{CT}]_0$, $A$=$k_1$ and the evolution of TAM signal is:

$$[\mathrm{OD}] = \frac{\sqrt{A}\times e^{-At}\times[\mathrm{OD}]_0}{\sqrt{A}+C\xi\sqrt{\pi}-C\xi\sqrt{\pi}\times erfc(\sqrt{At})} \qquad \text{(Eqn. 4.17)}$$

The diffusion coefficient was calculated in the same way as in the purely one-dimensional diffusion model from the best-fit parameter *C*, according to eqns 4.10-4.13.

# Chapter 5.

# Exciton Coherence in Assemblies of Rylene Dyes on Anodic Aluminum Oxide Membranes

## 5.1 INTRODUCTION

Photosynthesis provides chemical energy to living organisms on Earth through an initial process that involves energy capture through the absorption of sunlight. In these light-harvesting complexes chromophore aggregates absorb the light, which excites the chromophores from the ground to an electronically excited state. For this excitation to be harvested as energy, it must travel through the chromophores until it reaches a reaction center. It is generally thought that quantum coherence effects play an important role in energy transfer in light-harvesting systems.[13] Since electronic coupling in chromophore assemblies is strong due to the decreased distance between the molecules, delocalized excitations or excitons are often observed in these systems. The electronic excited state is in a superposition of the electronically excited states of more than one molecule, and therefore there is quantum coherence between neighboring chromophores. This has been observed as a delocalized exciton using ultrafast fluorescence upconversion and femtosecond transient absorption spectroscopy in the light-harvesting antenna of purple photosynthetic bacteria.[167-168]

Probing exciton coherence in a chromophore assembly on anodic aluminum oxide (AAO) membranes could increase our fundamental understanding of excitation delocalization, since this delocalization is different between solid state and molecular systems.[13] Chromophores self-assembled on AAO represent the intermediate regime between the solution phase and solid state as noted in Chapter 2, and therefore this structure represents another phase space of interest to explore exciton coherence length.

Spano and coworkers derived a method to estimate exciton coherence lengths and the extent of disorder in both *H* and *J*-aggregates.[109, 169] The *H*-aggregates are thin films of regioregular *poly*(3-hexylthiophene) (P3HT) that are good candidates for solar cells because of their high

charge field effect mobilities. These films are semicrystalline with excellent ordering between the polymers, allowing them to study the effect of interchain interactions on the photophysics.[169] Spano and coworkers were able to extract the exciton coherence length by treating the P3HT films as disordered *H*-aggregates and probing the (0,0) emission peak in these films, which is heavily dependent on the coherence of the emitting exciton. This analysis also relies on the fact that emission vibronic progressions in aggregates are significantly distorted relative to those in isolated chromophores.[170-172] The derivations show that the ratio between the (0,0) and (0,1) peaks in the emission spectrum can be used to estimate the coherence length in aggregates. This is described in the following equation 5.1:

$$N_{coh} \approx \lambda^2 \frac{\langle I^{(0,0)} c \rangle}{\langle I^{(0,1)} c \rangle} \qquad \text{Eqn. 5.1}$$

where $N_{coh}$ is the number of chromophores over which the exciton is coherent, $\lambda^2$ is the Huang-Rhys factor, and $I^{(0,0)}$ and $I^{(0,1)}$ are the line strengths of the (0,0) and (0,1) emission bands.

We have previous demonstrated that the degree of charge transfer (CT) character in the excimer can be modulated by the dielectric environment.[173] Increased CT character in excimers lowers the overall energy of the excimer and shortens its lifetime. Therefore, changing the dielectric environment of the chromophore assemblies that undergo excimer formation on AAO likely impacts the exciton coherence length since higher dielectric environments promote the CT state and its mixing with the Frenkel exciton state. The AAO systems in this study exhibit a range of CT character, ranging from excimer with CT character to symmetry breaking charge transfer (SB-CT) to symmetry breaking charge separation (SB-CS) depicted in Figure 5.1.

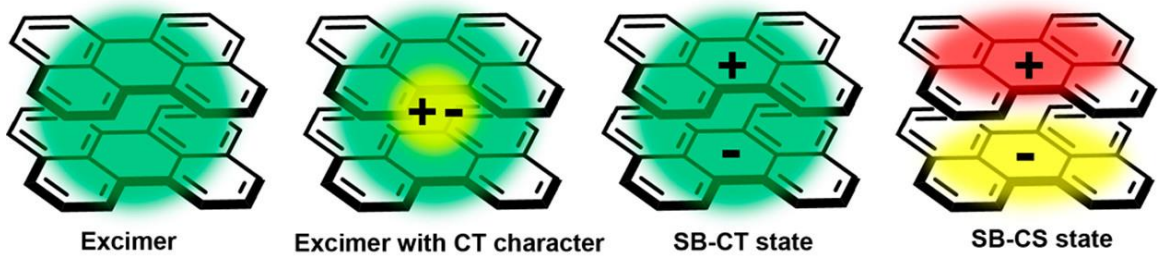


**Figure 5.1.** Depiction of perylene excimer, excimer with CT character, SB-CT, and SB-CS states. Adapted with permission from J. Phys. Chem. C 2021, 27, 14843–14853. Copyright 2021, American Chemical Society.

## 5.2 EXPERIMENTAL

### 5.2.1 Assembly of AAO membrane systems

Free-standing anodic aluminum oxide membranes (80 nm pore diameter, 1 cm diameter, 50 μm thickness) were purchased from InRedox. AAO membranes were sonicated in deionized water and isopropanol for 10 min and then dried in an oven at 100 °C. To covalently attach PDI to the surface of the AAO membrane nanopores, a free-standing AAO membrane with an 80 nm pore diameter was soaked in a 1 mM solution of PDI silatrane in dichloromethane. To intercalate PDI in the AAO nanopores, an AAO membrane was soaked in 1 mM of octadecyltriethoxysilane for 24 hours. This lipid-coated AAO was then soaked in 1 mM solution of symmetric PDI for 24 hours. Both AAO membranes were washed with dichloromethane and methanol and dried prior to making measurements.[173] PEP-Si and C8-tpPDI-Si (Figure 5.2) were synthesized and dissolved in dichloromethane (DCM). AAO membranes were immersed in each of these 1 mM solutions for 12 h to covalently attach PEP-Si to the membrane pores through the reaction between the triethoxysilyl group on PEP-Si and hydroxy groups on AAO membranes to form Si–O bonds; residual PEP-Si was removed by washing the membranes with excess DCM to give PEP-AAO,

which were then dried under vacuum for further characterization. Following the same procedure as for PEP-AAO, tpPDI-AAO was obtained. All four AAO systems were placed in a 1 mm cuvette for time-resolved spectroscopy measurements.

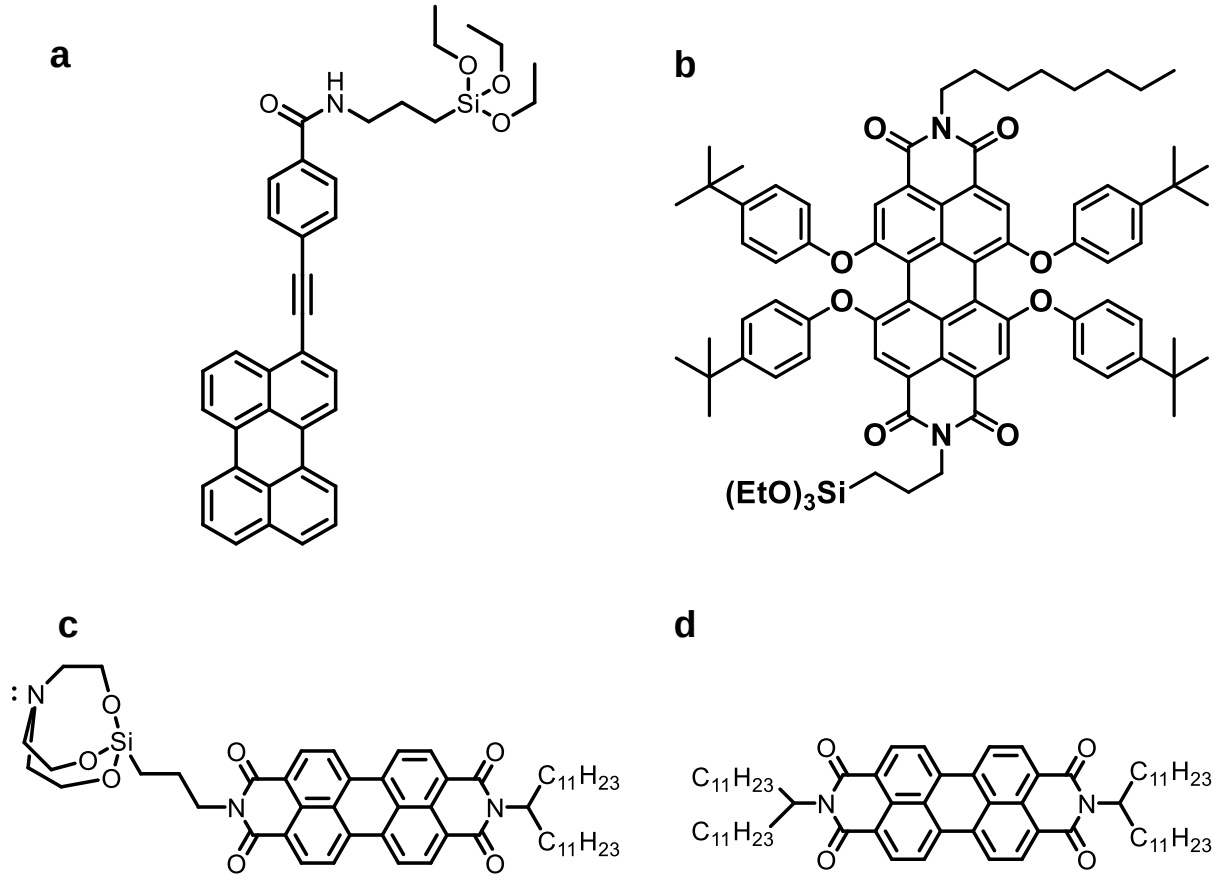


**Figure 5.2.** Chemical structures of (a) 3-(phenylethynyl)perylene (PEP), (b) Tetrakis(4-tert-butylphenoxy)PDI, (c) PDI silatrane, and (d) PDI with C23 tails.

### 5.2.2 Steady state absorption and emission

UV-vis spectra of the PDI derivatives were obtained at ambient temperature on a Shimadzu 1800 UV-vis spectrometer in water, MeCN, THF, DCM, and toluene. Fluorescence measurements were obtained using a HORIBA Fluorolog-3 spectrofluorimeter.

## 5.3 RESULTS

### 5.3.1 Nature of chromophore aggregation (absorption) in different dielectric environments

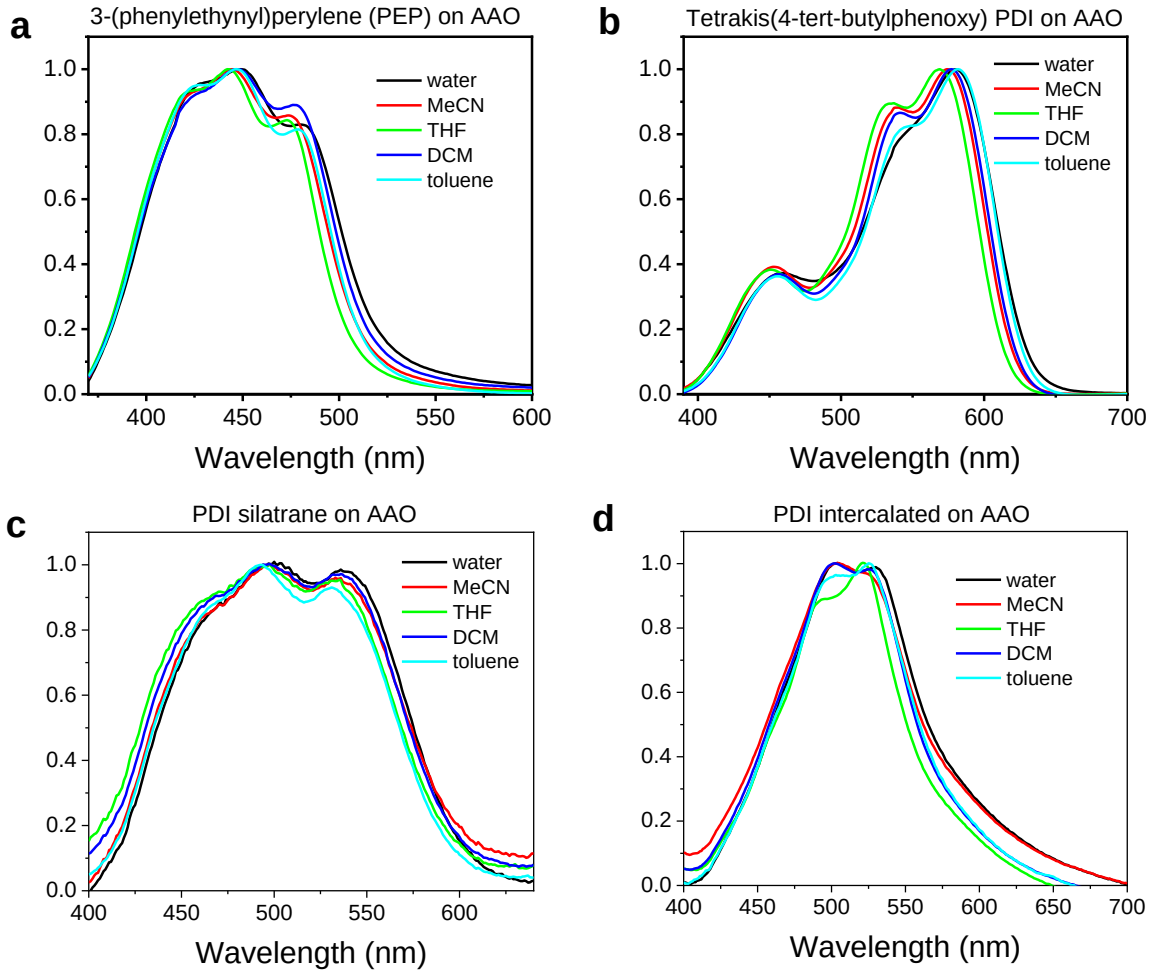


**Figure 5.3.** Absorption spectra of (a) 3-(phenylethynyl)perylene (PEP) on AAO, (b) Tetrakis(4-tert-butylphenoxy)PDI on AAO, (c) PDI silatrane on AAO, and (d) PDI intercalated on AAO in water, MeCN, THF, DCM, and toluene.

Spectral signatures, including the vibronic bands, in the steady state absorption spectrum of organic chromophore assemblies have been used to determine the nature of aggregation in the system. Rylene dyes form both H- and J- aggregates, where H-aggregates stack "side-by-side" and J-aggregates "head-to-tail."[174] The change in the relative oscillator strengths of the (0,0) and (0,*n*)

vibronic bands in the steady state absorption spectra of organic aggregates compared to their monomers indicate the degree of excitonic coupling.

In perylene on AAO, the ratio of the vibronic bands (0,0) and (0,2) at 448 nm and 426 nm, respectively, indicates the strength of excitonic coupling. The steady state absorption spectrum of the 3-(phenylethynyl)perylene (PEP) monomer in dichloromethane yields an $A_{0,0}/A_{0,2}$ value of ~0.92. The values in Table 5.1 show that the degree of excitonic coupling between the PEPs on AAO is significantly stronger than that of the PEP monomers in solution, and the average $A_{0,0}/A_{0,2}$ value is 1.07. The dielectric environment has little effect on the excitonic coupling strength between PEPs on AAO. Tetrakis(4-tert-butylphenoxy)PDI (tp-PDI) on AAO yields $A_{0,0}/A_{0,1}$ values that are lower than the $A_{0,0}/A_{0,1}$ value of 1.53 for the tp-PDI monomer in DCM. The vibronic bands (0,0) and (0,1) are the bands at 577 nm and 540 nm. In our previous studies of tp-PDI on AAO, we demonstrated that tp-PDI does not cluster when incorporated in AAOs.[175] The $A_{0,0}/A_{0,1}$ value is the highest at 1.32 for tp-PDI on AAO in water, which indicates that the excitonic coupling between tp-PDI molecules decreases in water. This is due to the high dielectric constant of water, which likely screens electron-electron and electron-hole interactions in the exciton and disrupts the excitonic coupling.[176]

In PDI silatrane on AAO, the $A_{0,1}/A_{0,0}$ ratios are enhanced compared to that of the monomer, indicating significant excitonic coupling. The (0,0) and (0,1) vibronic bands are observed at 540 nm and 490 nm. As seen in the case of PEP on AAO, the dielectric environment does not strongly influence the absorbance ratio in the PDI silatrane on AAO system and the average $A_{0,1}/A_{0,0}$ value is 1.05. The $A_{0,1}/A_{0,0}$ values for PDI intercalated on AAO in water, MeCN, and DCM are larger than that of the PDI monomer; this indicates aggregation and a higher degree of excitonic coupling between the PDIs. However, the PDI intercalated on AAO system in THF

and toluene have lower $A_{0,1}/A_{0,0}$ values, which indicates more monomeric behavior in these solvents. This could be due to better solvation of PDI or the lipid chains on the AAO, which could induce monomeric absorption due to solvent molecules penetrating between the cores of the PDI molecules or the lipid chains, allowing the lipid molecules to disrupt packing between the PDIs intercalated on the AAO.

Three of the organic chromophore aggregate systems discussed above—PEP on AAO, PDI silatrane on AAO, and PDI intercalated on AAO—exhibit steady state absorption spectra characteristic of *H*-aggregates since the absorption maximum is blue-shifted relative to that of the isolated monomer.[177] The hypsochromic shift of the absorption maximum is absent only in the tp-PDI on AAO system, which undergoes symmetry breaking charge separation (SB-CS).

**Table 5.1**: Steady-state absorption spectral data in various solvents at 298 K.

| | Solvent | $A_{0,0}/A_{0,2}$ transition ratio |
|---|---|---|
| 3-(phenylethynyl)perylene (PEP) on AAO | water | 1.05 |
| | MeCN | 1.08 |
| | THF | 1.07 |
| | DCM | 1.09 |
| | toluene | 1.06 |
| | Solvent | $A_{0,0}/A_{0,1}$ transition ratio |
| Tetrakis(4-tert-butylphenoxy)PDI (tp-PDI) on AAO | water | 1.32 |
| | MeCN | 1.14 |
| | THF | 1.12 |
| | DCM | 1.16 |

| | | |
|---|---|---|
| | toluene | 1.23 |
| PDI silatrane on AAO | Solvent | $A_{0,1}/A_{0,0}$ transition ratio |
| | water | 1.02 |
| | MeCN | 1.04 |
| | THF | 1.05 |
| | DCM | 1.03 |
| | toluene | 1.08 |
| PDI intercalated on AAO | Solvent | $A_{0,1}/A_{0,0}$ transition ratio |
| | water | 1.01 |
| | MeCN | 1.03 |
| | THF | 0.88 |
| | DCM | 1.02 |
| | toluene | 0.95 |

### 5.3.2 Comparing the exciton coherence length

Spano et al. demonstrated that the 0-0 emission peak of J-aggregates and in some cases, H-aggregates, is a probe for the degree of disorder in a system. Specifically, Eq. 5.1 mentioned in introductory section 5.1 can be used to estimate the number of molecules over which the exciton is coherent: $N_{coh} = \lambda^2 \frac{I^{0-0}}{I^{0-1}}$. The Huang-Rhys factor $\lambda^2$ was calculated as shown in 5.5.1.

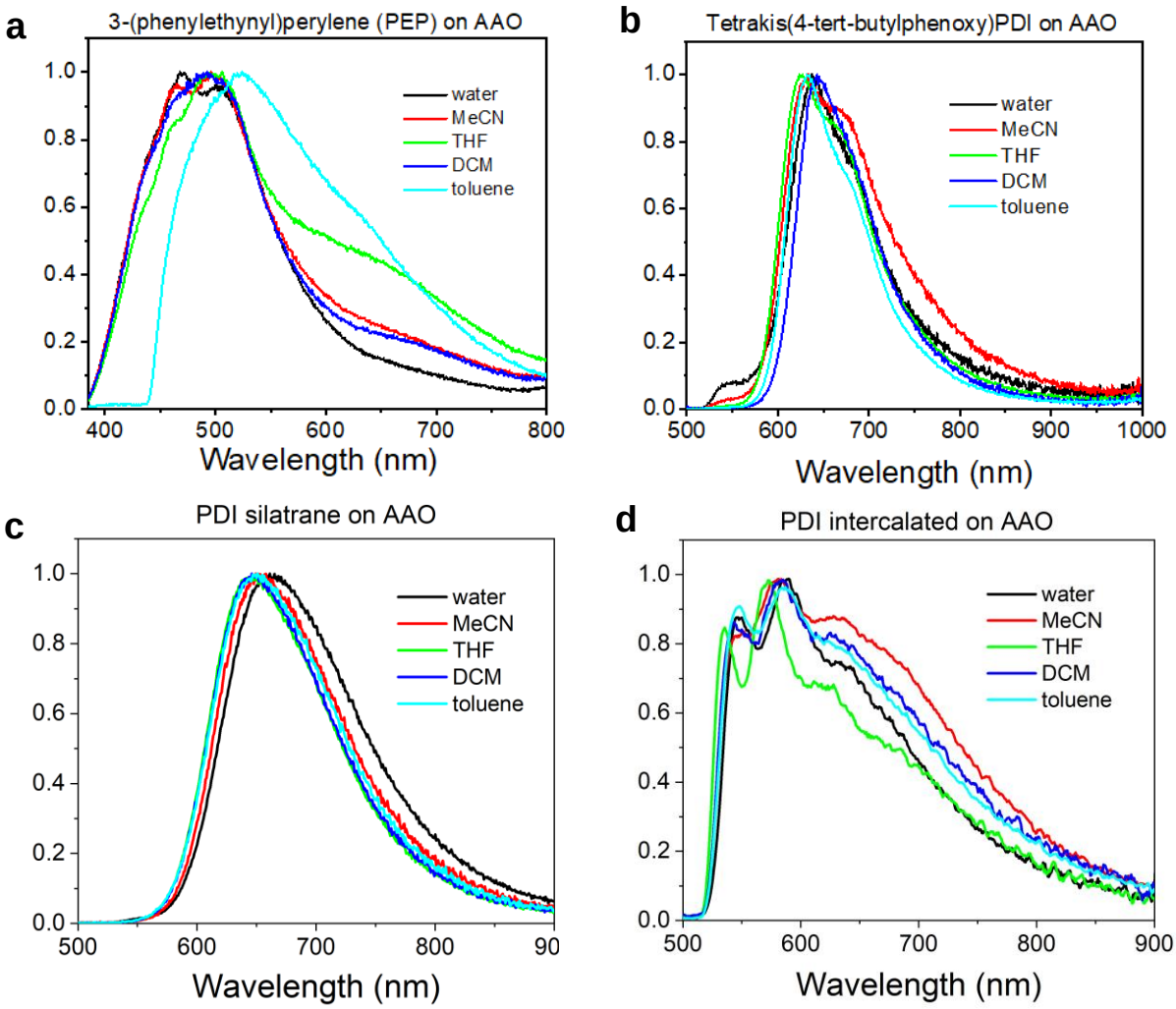


**Figure 5.4.** Emission spectra of (a) 3-(phenylethynyl)perylene (PEP) on AAO, (b) Tetrakis(4-tert-butylphenoxy)PDI on AAO, (c) PDI silatrane on AAO, and (d) PDI intercalated on AAO in water, MeCN, THF, DCM, and toluene.

The emission data of all the AAO systems was fit to a sum of Gaussians, except for PDI silatrane on AAO emission data that lacked a clear vibronic progression for analysis. The emission peak intensity ratio $I^{0\text{-}0}/I^{0\text{-}1}$ for the AAO systems were calculated from the area under the Gaussian curves and are listed in Table 5.2.

**Table 5.2**: Calculated 0-0 to 0-1 peak ratio from the steady state emission spectra.

| | Solvent | $I^{0\text{-}0}/I^{0\text{-}1}$ |
|---|---|---|
| 3-(phenylethynyl)perylene (PEP) on AAO | water | 1.28 |
| | MeCN | 2.23 |
| | THF | 5.94 |
| | DCM | 0.83 |
| | toluene | 0.28 |
| | Solvent | $I^{0\text{-}0}/I^{0\text{-}1}$ |
| Tetrakis(4-tert-butylphenoxy)PDI (tp-PDI) on AAO | water | 0.35 |
| | MeCN | 0.31 |
| | THF | 0.44 |
| | DCM | 0.49 |
| | toluene | 0.60 |
| | Solvent | $I^{0\text{-}0}/I^{0\text{-}1}$ |
| PDI silatrane on AAO | water | - |
| | MeCN | - |
| | THF | - |

| | | |
|---|---|---|
| | DCM | - |
| | toluene | - |
| PDI intercalated on AAO | Solvent | $I^{0-0}/I^{0-1}$ |
| | water | 0.41 |
| | MeCN | 0.29 |
| | THF | 0.39 |
| | DCM | 0.37 |
| | toluene | 0.43 |

All the emission peak intensity ratios are below 1, except for PEP on AAO in more polar solvents (water, MeCN, THF). Using these values and the Huang-Rhys factors, we estimate $N_{coh}$ and the coherence length values are listed in Table 5.3.

**Table 5.3**: Calculated coherence length, $N_{coh}$

| | Solvent | $N_{coh}$ |
|---|---|---|
| 3-(phenylethynyl)perylene (PEP) on AAO | water | 0.81 |
| | MeCN | 1.41 |
| | THF | 3.74 |
| | DCM | 0.52 |
| | toluene | 0.18 |
| Tetrakis(4-tert-butylphenoxy)PDI (tp-PDI) on AAO | Solvent | $N_{coh}$ |
| | water | 0.39 |
| | MeCN | 0.34 |

| | | |
|---|---|---|
| | THF | 0.48 |
| | DCM | 0.54 |
| | toluene | 0.66 |
| PDI silatrane on AAO | Solvent | $N_{coh}$ |
| | water | - |
| | MeCN | - |
| | THF | - |
| | DCM | - |
| | toluene | - |
| PDI intercalated on AAO | Solvent | $N_{coh}$ |
| | water | 0.27 |
| | MeCN | 0.19 |
| | THF | 0.26 |
| | DCM | 0.25 |
| | toluene | 0.29 |

The coherence length values are below 1, except for in PEP on AAO in MeCN and THF. Such values are expected when emission data is not at very early times, as shown by Tempelaar et al. Equation 5.1 holds for both H and J-aggregates at early times in the time-resolved emission data where the exciton is coherent (10s-100s of femtoseconds).[178] At later times, the number of units over which the exciton is coherence decreases to below unity for H-aggregates.

### 5.3.3 Excitation wavelength dependent emission in tpPDI-AAO

When tpPDI on AAO is excited at redder wavelengths, this leads to the appearance of a new emission band in the near infrared region of the steady state emission, centered at 840 nm.

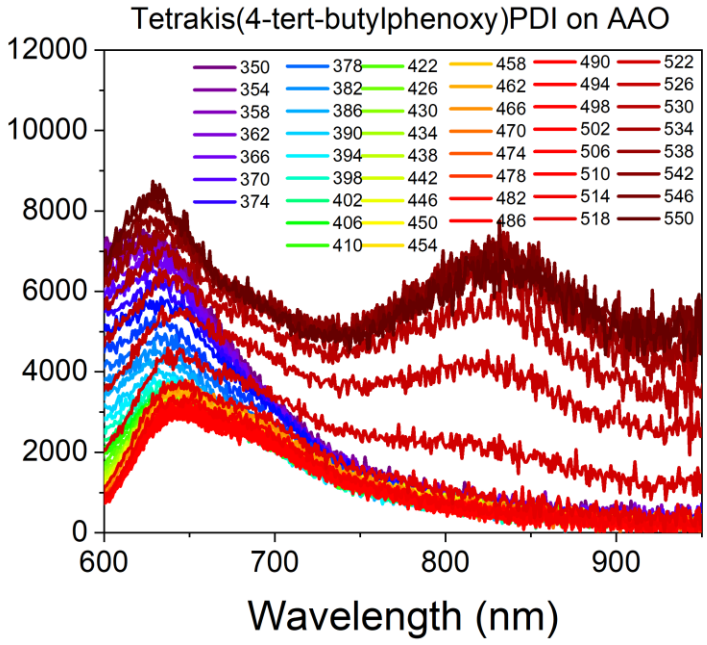


**Figure 5.5.** Excitation wavelength-dependent emission spectra of tetrakis(4-tert-butylphenoxy)PDI on AAO in water.

Excitation-dependent emission spectra are generally not common in idealized systems because of Kasha's rule. Because energy transfer and excimer formation that occur in systems outcompete the fluorescence lifetime, only emission from the lowest excited electronic state is observed. This red-shifted emission band is not observed in PDIs or BPEA on AAO, which indicates the band at 830 nm is not from the bare AAO. Since tpPDI-AAO exhibits complete symmetry breaking charge separation, the origin of the excitation-dependent emission may be due to the fact that out of the four chromophore-AAO systems studied, tpPDI-AAO does not form excimer upon photoexcitation.

## 5.4 CONCLUSIONS

The exciton coherence length has been estimated in H- and J-aggregates from the steady state emission vibronic band ratios and the Huang-Rhys factors in earlier work by Spano and coworkers. We hypothesized that the degree of exciton coherence could be modulated by the solvent environment because the dielectric environment changes the CT character of the excimer in the AAO systems studied. After extracting the $I^{0\text{-}0}/I^{0\text{-}1}$ values and Huang-Rhys factors, $N_{coh}$ was calculated and yielded values mostly below unity. This is consistent with previous studies that show the exciton is coherence only at very early times and that the emission ratio shrinks below the single-chromophore value; steady-state emission of H-aggregates suffers from coherent suppression instead of enhancement. Future work using broadband fluorescence upconversion techniques could track Frenkel exciton dynamics in H-aggregates on AAO.

## 5.5 SUPPORTING INFORMATION

### 5.5.1 Calculation of Huang-Rhys factors

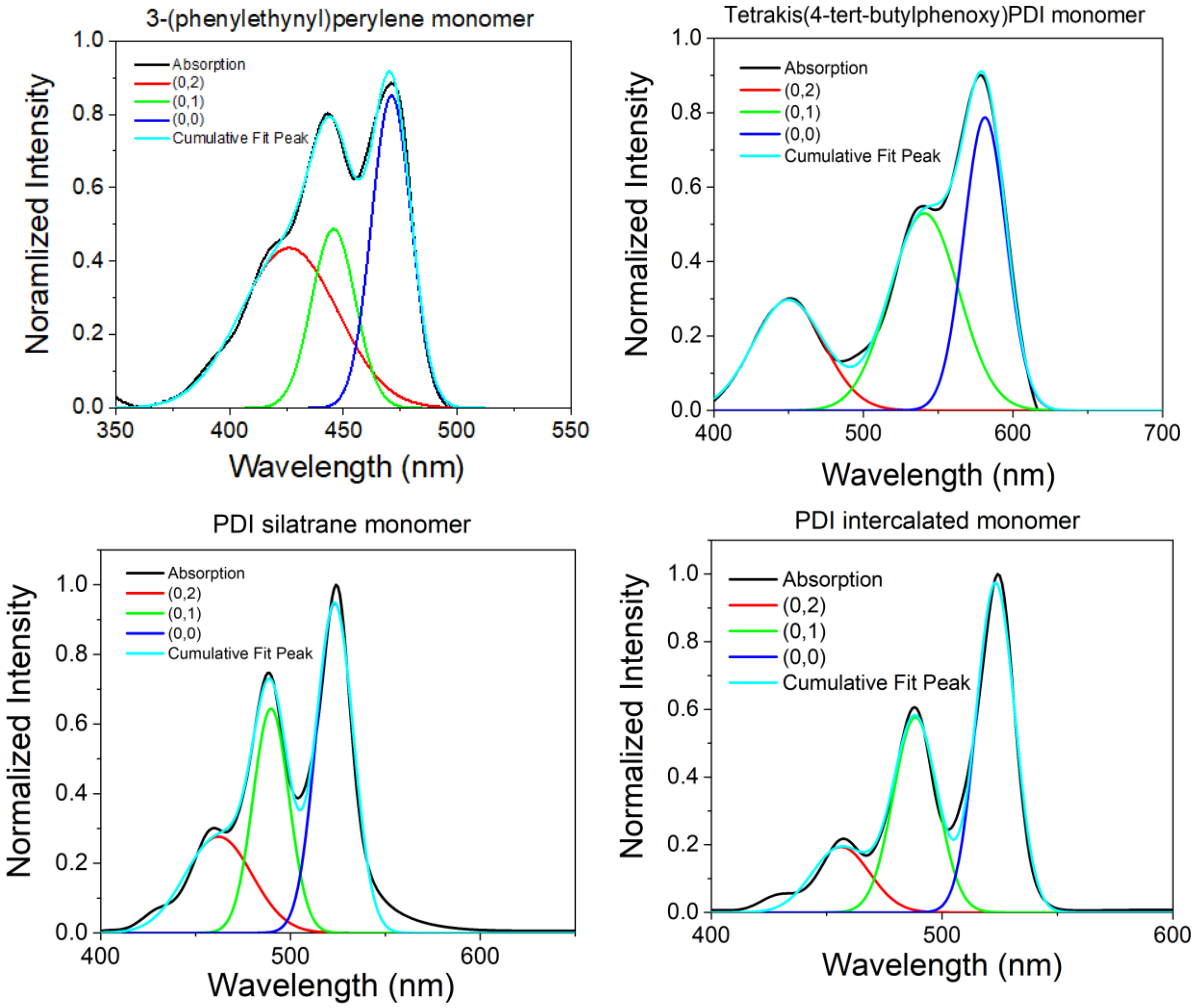


**Figure 5.6.** Gaussian fits to monomer steady state absorption spectra for AAO systems discussed. Huang-Rhys factor is calculated from the ratio of the areas under the Gaussian fits to the 0-1 and 0-0 vibronic bands.

**Table 5.4.** List of Huang-Rhys factors

| | $I_{Gaussian}^{0-1}$ | $I_{Gaussian}^{0-0}$ | $\lambda^2$ |
|---|---|---|---|
| **PEP monomer** | 11.7 | 18.5 | 0.63 |
| **tpPDI monomer** | 30.6 | 27.8 | 1.1 |
| **PDI silatrane monomer** | 15.3 | 23.2 | 0.65 |
| **PDI intercalated monomer** | 13.7 | 20.3 | 0.67 |

### 5.5.2 Gaussian fits of AAO steady state emission spectra

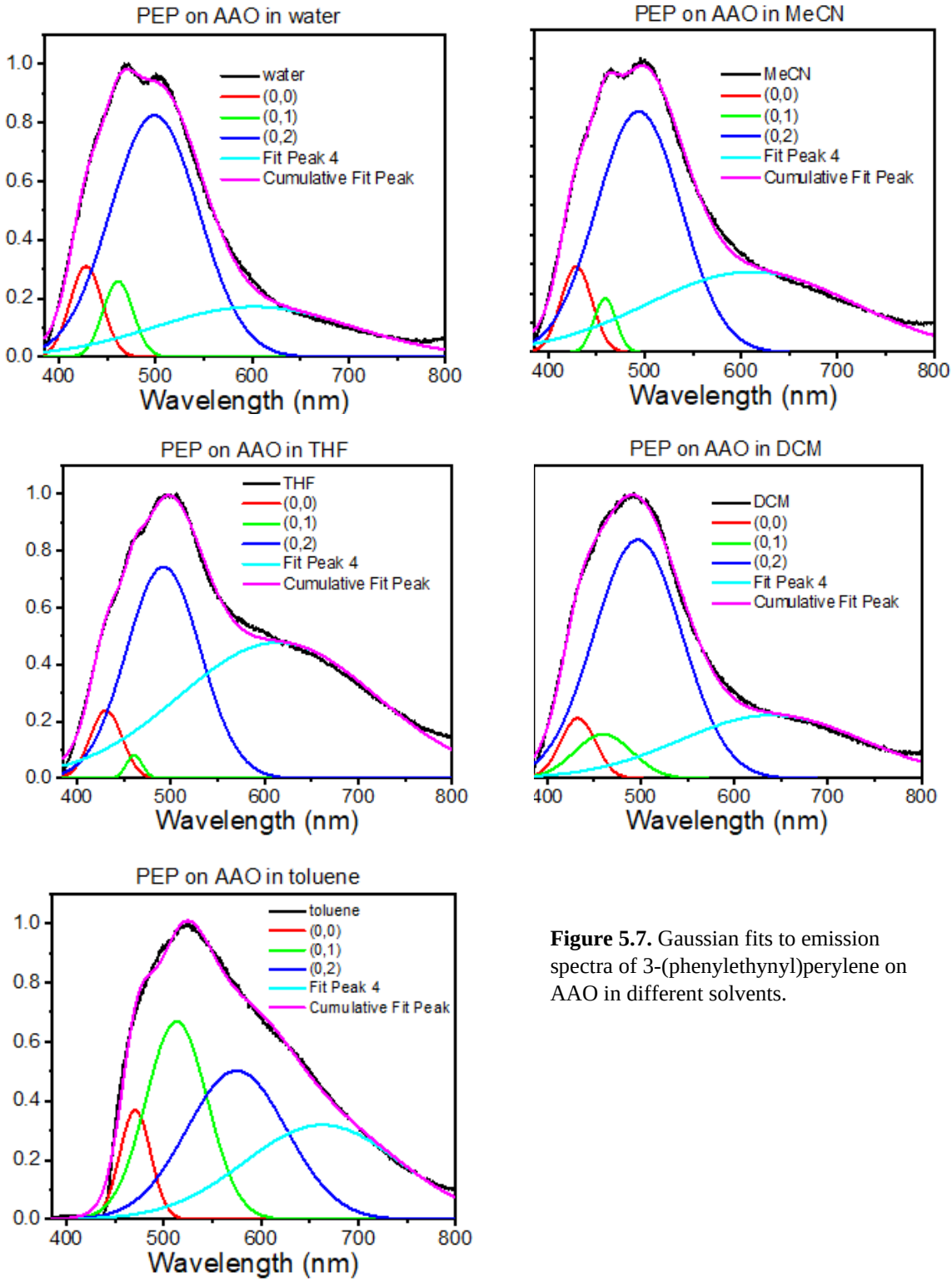


**Figure 5.7.** Gaussian fits to emission spectra of 3-(phenylethynyl)perylene on AAO in different solvents.

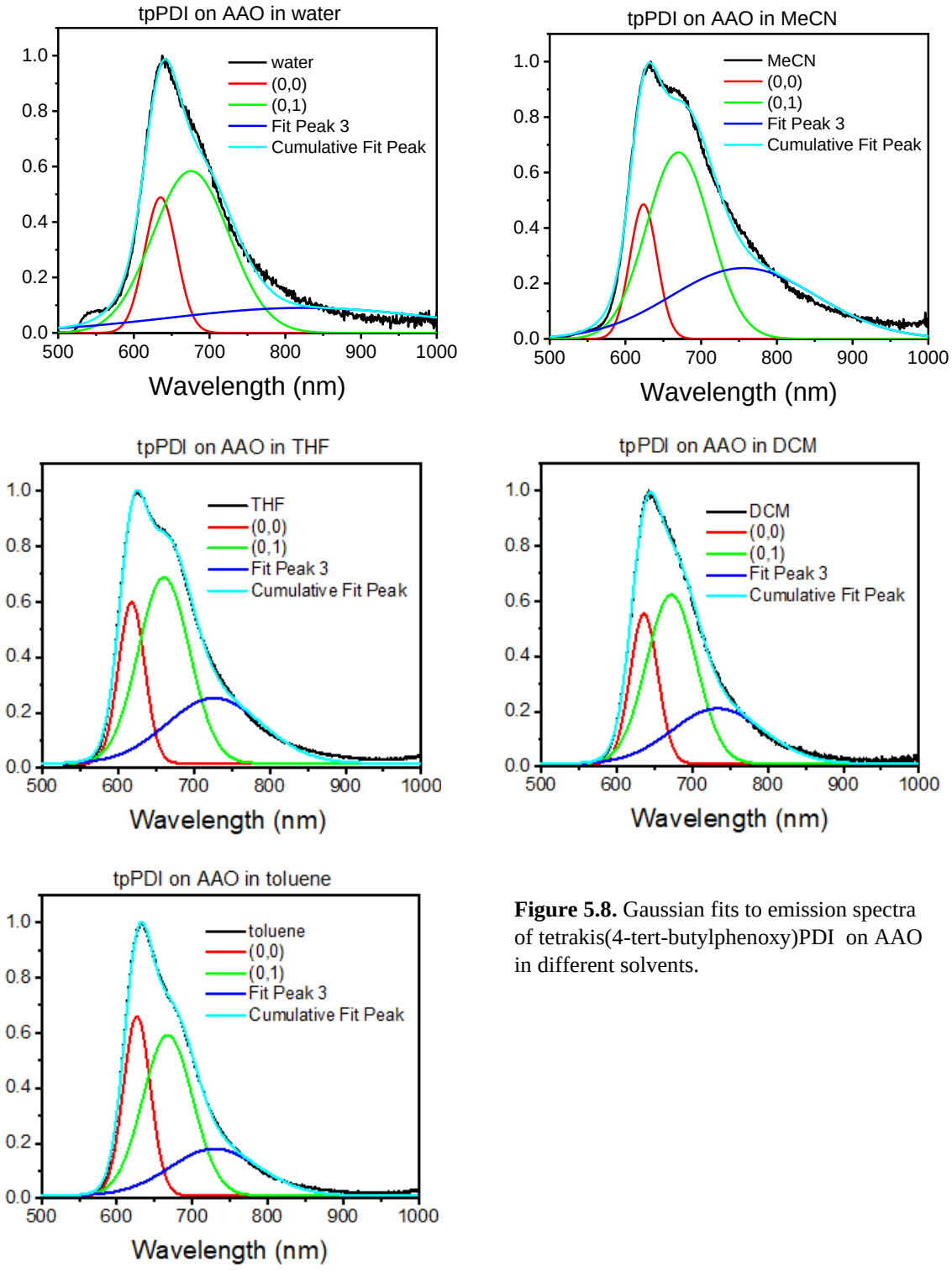


**Figure 5.8.** Gaussian fits to emission spectra of tetrakis(4-tert-butylphenoxy)PDI on AAO in different solvents.

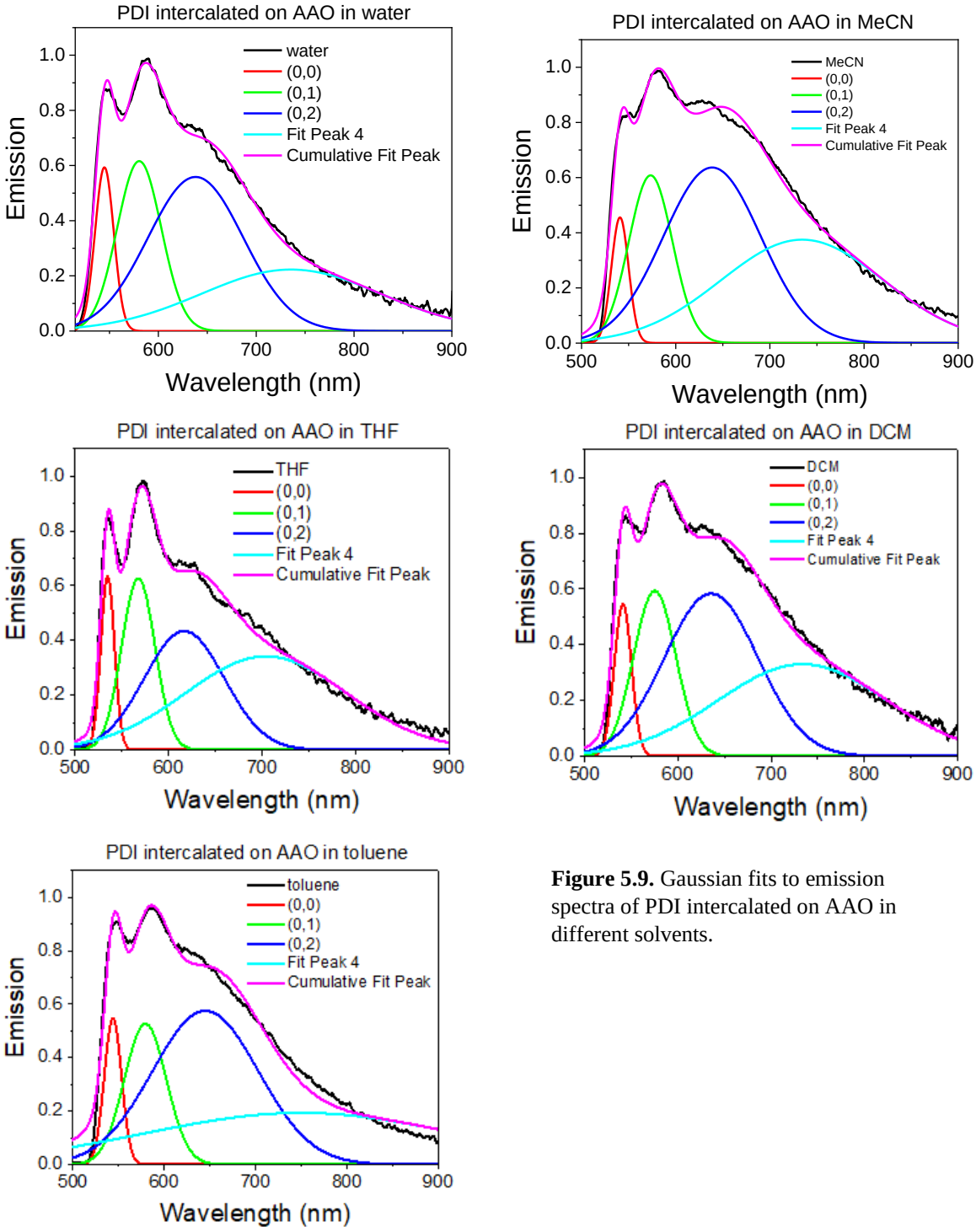


**Figure 5.9.** Gaussian fits to emission spectra of PDI intercalated on AAO in different solvents.

# References


1. Administration., U. S. E. I. International Energy Outlook 2017.

2. Lewis, N. S.; Nocera, D. G., Powering the planet: Chemical challenges in solar energy utilization. *Proceedings of the National Academy of Sciences* **2006,** *103* (43), 15729-15735.

3. Cao, W.; Xue, J., Recent progress in organic photovoltaics: device architecture and optical design. *Energy & Environmental Science* **2014,** *7* (7), 2123-2144.

4. Scholes, G. D.; Fleming, G. R.; Olaya-Castro, A.; van Grondelle, R., Lessons from nature about solar light harvesting. *Nature Chemistry* **2011,** *3* (10), 763-774.

5. van Grondelle, R.; Novoderezhkin, V. I., Energy transfer in photosynthesis: experimental insights and quantitative models. *Physical Chemistry Chemical Physics* **2006,** *8* (7), 793-807.

6. Novoderezhkin, V. I.; van Grondelle, R., Physical origins and models of energy transfer in photosynthetic light-harvesting. *Physical Chemistry Chemical Physics* **2010,** *12* (27), 7352-7365.

7. Renger, T., Theory of excitation energy transfer: from structure to function. *Photosynthesis Research* **2009,** *102* (2), 471-485.

8. Schlau-Cohen, G. S.; Calhoun, T. R.; Ginsberg, N. S.; Read, E. L.; Ballottari, M.; Bassi, R.; van Grondelle, R.; Fleming, G. R., Pathways of Energy Flow in LHCII from Two-Dimensional Electronic Spectroscopy. *The Journal of Physical Chemistry B* **2009,** *113* (46), 15352-15363.

9. Novoderezhkin, V. I.; Doust, A. B.; Curutchet, C.; Scholes, G. D.; van Grondelle, R., Excitation Dynamics in Phycoerythrin 545: Modeling of Steady-State Spectra and Transient Absorption with Modified Redfield Theory. *Biophysical Journal* **2010,** *99* (2), 344-352.

10. Davydov, A. S., THE THEORY OF MOLECULAR EXCITONS. *Soviet Physics Uspekhi* **1964,** *7* (2), 145-178.

11. Kasha, M., Energy Transfer Mechanisms and the Molecular Exciton Model for Molecular Aggregates. *Radiation Research* **1963,** *20* (1), 55-70.

12. Kasha, M.; Rawls, H. R.; Ashraf El-Bayoumi, M., The exciton model in molecular spectroscopy. In *Pure and Applied Chemistry*, 1965; Vol. 11, p 371.

13. Fassioli, F.; Dinshaw, R.; Arpin, P. C.; Scholes, G. D., Photosynthetic light harvesting: excitons and coherence. *Journal of The Royal Society Interface* **2014,** *11* (92), 20130901.

14. Hestand, N. J.; Spano, F. C., Molecular Aggregate Photophysics beyond the Kasha Model: Novel Design Principles for Organic Materials. *Accounts of Chemical Research* **2017,** *50* (2), 341-350.

15. Yamagata, H.; Maxwell, D. S.; Fan, J.; Kittilstved, K. R.; Briseno, A. L.; Barnes, M. D.; Spano, F. C., HJ-Aggregate Behavior of Crystalline 7,8,15,16-Tetraazaterrylene: Introducing a

New Design Paradigm for Organic Materials. *The Journal of Physical Chemistry C* **2014,** *118* (49), 28842-28854.

16. Gregg, B. A.; Kose, M. E., Reversible Switching between Molecular and Charge Transfer Phases in a Liquid Crystalline Organic Semiconductor. *Chemistry of Materials* **2008,** *20* (16), 5235-5239.

17. Hestand, N. J.; Spano, F. C., Expanded Theory of H- and J-Molecular Aggregates: The Effects of Vibronic Coupling and Intermolecular Charge Transfer. *Chemical Reviews* **2018,** *118* (15), 7069-7163.

18. Petelenz, B.; Petelenz, P.; Shurvell, H. F.; Smith, V. H., Reconsideration of the electroabsorption spectra of the tetracene and pentacene crystals. *Chemical Physics* **1988,** *119* (1), 25-39.

19. Katoh, R.; Sinha, S.; Murata, S.; Tachiya, M., Origin of the stabilization energy of perylene excimer as studied by fluorescence and near-IR transient absorption spectroscopy. *Journal of Photochemistry and Photobiology A: Chemistry* **2001,** *145* (1), 23-34.

20. Brown, K. E.; Salamant, W. A.; Shoer, L. E.; Young, R. M.; Wasielewski, M. R., Direct Observation of Ultrafast Excimer Formation in Covalent Perylenediimide Dimers Using Near-Infrared Transient Absorption Spectroscopy. *The Journal of Physical Chemistry Letters* **2014,** *5* (15), 2588-2593.

21. Katoh, R.; Katoh, E.; Nakashima, N.; Yuuki, M.; Kotani, M., Near-IR Absorption Spectrum of Aromatic Excimers. *The Journal of Physical Chemistry A* **1997,** *101* (42), 7725-7728.

22. Leng, W.; Würthner, F.; Kelley, A. M., Resonance Raman Intensity Analysis of Merocyanine Dimers in Solution. *The Journal of Physical Chemistry B* **2004,** *108* (29), 10284-10294.

23. Wu, Y.; Zhou, J.; Phelan, B. T.; Mauck, C. M.; Stoddart, J. F.; Young, R. M.; Wasielewski, M. R., Probing Distance Dependent Charge-Transfer Character in Excimers of Extended Viologen Cyclophanes Using Femtosecond Vibrational Spectroscopy. *Journal of the American Chemical Society* **2017,** *139* (40), 14265-14276.

24. Young, R. M.; Wasielewski, M. R., Mixed Electronic States in Molecular Dimers: Connecting Singlet Fission, Excimer Formation, and Symmetry-Breaking Charge Transfer. *Accounts of Chemical Research* **2020,** *53* (9), 1957-1968.

25. Powers-Riggs, N. E.; Zuo, X.; Young, R. M.; Wasielewski, M. R., Symmetry-Breaking Charge Separation in a Nanoscale Terrylenediimide Guanine-Quadruplex Assembly. *J. Am. Chem. Soc.* **2019,** *141* (44), 17512-17516.

26. Wu, Y.-L.; Brown, K. E.; Wasielewski, M. R., Extending Photoinduced Charge Separation Lifetimes by Using Supramolecular Design: Guanine–Perylenediimide G-Quadruplex. *Journal of the American Chemical Society* **2013,** *135* (36), 13322-13325.

27. Wu, Y.-L.; Horwitz, N. E.; Chen, K.-S.; Gomez-Gualdron, D. A.; Luu, N. S.; Ma, L.; Wang, T. C.; Hersam, M. C.; Hupp, J. T.; Farha, O. K.; Snurr, R. Q.; Wasielewski, M. R., G-quadruplex organic frameworks. *Nat. Chem.* **2017,** *9* (5), 466-472.

28. Driver, M. D.; Williamson, M. J.; Cook, Joanne L.; Hunter, C. A., Functional group interaction profiles: a general treatment of solvent effects on non-covalent interactions. *Chemical Science* **2020,** *11* (17), 4456-4466.

29. Baram, J.; Weissman, H.; Tidhar, Y.; Pinkas, I.; Rybtchinski, B., Hydrophobic Self-Assembly Affords Robust Noncovalent Polymer Isomers. *Angewandte Chemie International Edition* **2014,** *53* (16), 4123-4126.

30. Li, Y.; Zhao, T.; Wang, C.; Lin, Z.; Huang, G.; Sumer, B. D.; Gao, J., Molecular basis of cooperativity in pH-triggered supramolecular self-assembly. *Nature Communications* **2016,** *7* (1), 13214.

31. Huang, X.; Mutlu, H.; Théato, P., The toolbox of porous anodic aluminum oxide–based nanocomposites: from preparation to application. *Colloid and Polymer Science* **2021,** *299* (3), 325-341.

32. Kim, J. S.; Kim, T. G.; Kong, W. H.; Park, T. G.; Nam, Y. S., Thermally controlled wettability of a nanoporous membrane grafted with catechol-tethered poly(N-isopropylacrylamide). *Chemical Communications* **2012,** *48* (74), 9227-9229.

33. Kim, H.; Lee, S.; Shin, T. J.; Korblova, E.; Walba, D. M.; Clark, N. A.; Lee, S. B.; Yoon, D. K., Multistep hierarchical self-assembly of chiral nanopore arrays. *Proceedings of the National Academy of Sciences* **2014,** *111* (40), 14342.

34. Pathak, A.; Bora, A.; Braunschweig, B.; Meltzer, C.; Yan, H.; Lemmens, P.; Daum, W.; Schwartz, J.; Tornow, M., Nanocylindrical confinement imparts highest structural order in molecular self-assembly of organophosphonates on aluminum oxide. *Nanoscale* **2017,** *9* (19), 6291-6295.

35. Haruk, A. M.; Leng, C. Z.; Fernando, P. S.; Smilgies, D.-M.; Loo, Y.-L.; Mativetsky, J. M., Tuning Organic Semiconductor Alignment and Aggregation via Nanoconfinement. *The Journal of Physical Chemistry C* **2020,** *124* (41), 22799-22807.

36. Chen, H.-F.; Gardner, D. M.; Carmieli, R.; Wasielewski, M. R., Controlling the orientation of spin-correlated radical pairs by covalent linkage to nanoporous anodic aluminum oxide membranes. *Chemical Communications* **2013,** *49* (77), 8614-8616.

37. Zhu, W.; Zheng, R.; Fu, X.; Fu, H.; Shi, Q.; Zhen, Y.; Dong, H.; Hu, W., Revealing the Charge-Transfer Interactions in Self-Assembled Organic Cocrystals: Two-Dimensional Photonic Applications. *Angewandte Chemie International Edition* **2015,** *54* (23), 6785-6789.

38. Horiuchi, S.; Ishii, F.; Kumai, R.; Okimoto, Y.; Tachibana, H.; Nagaosa, N.; Tokura, Y., Ferroelectricity near room temperature in co-crystals of nonpolar organic molecules. *Nature Materials* **2005,** *4* (2), 163-166.

39. Lei, Y. L.; Liao, L. S.; Lee, S. T., Selective Growth of Dual-Color-Emitting Heterogeneous Microdumbbells Composed of Organic Charge-Transfer Complexes. *Journal of the American Chemical Society* **2013,** *135* (10), 3744-3747.

40. Ferraris, J.; Cowan, D. O.; Walatka, V.; Perlstein, J. H., Electron transfer in a new highly conducting donor-acceptor complex. *Journal of the American Chemical Society* **1973,** *95* (3), 948-949.

41. Park, S. K.; Varghese, S.; Kim, J. H.; Yoon, S.-J.; Kwon, O. K.; An, B.-K.; Gierschner, J.; Park, S. Y., Tailor-Made Highly Luminescent and Ambipolar Transporting Organic Mixed Stacked Charge-Transfer Crystals: An Isometric Donor–Acceptor Approach. *Journal of the American Chemical Society* **2013,** *135* (12), 4757-4764.

42. Schlesinger, I.; Powers-Riggs, N. E.; Logsdon, J. L.; Qi, Y.; Miller, S. A.; Tempelaar, R.; Young, R. M.; Wasielewski, M. R., Charge-transfer biexciton annihilation in a donor–acceptor co-crystal yields high-energy long-lived charge carriers. *Chemical Science* **2020**.

43. Ding, Z.; Shang, H.; Zhang, S.; Han, W.; Li, B.; Jiang, S., Insight from Molecular Packing: Charge Transfer and Emission Modulation through Cocrystal Strategies. *Crystal Growth & Design* **2020,** *20* (8), 5203-5210.

44. Dong, Y.; Xu, B.; Zhang, J.; Tan, X.; Wang, L.; Chen, J.; Lv, H.; Wen, S.; Li, B.; Ye, L.; Zou, B.; Tian, W., Piezochromic Luminescence Based on the Molecular Aggregation of 9,10-Bis((E)-2-(pyrid-2-yl)vinyl)anthracene. *Angewandte Chemie International Edition* **2012,** *51* (43), 10782-10785.

45. Wang, C.; Li, Z., Molecular conformation and packing: their critical roles in the emission performance of mechanochromic fluorescence materials. *Materials Chemistry Frontiers* **2017,** *1* (11), 2174-2194.

46. Yan, D.; Evans, D. G., Molecular crystalline materials with tunable luminescent properties: from polymorphs to multi-component solids. *Materials Horizons* **2014,** *1* (1), 46-57.

47. Oh, S.; Park, S. K.; Jhun, B. H.; Roldao, J. C.; Kim, J. H.; Choi, M.-W.; Ryoo, C. H.; Jung, S.; Demitri, N.; Fischer, R.; Serdiuk, I. E.; Resel, R.; Gierschner, J.; Park, S. Y., Unraveling the Origin of High-Efficiency Photoluminescence in Mixed-Stack Isostructural Crystals of Organic Charge-Transfer Complex: Fine-Tuning of Isometric Donor–Acceptor Pairs. *The Journal of Physical Chemistry C* **2020,** *124* (37), 20377-20387.

48. Yu, P.; Li, Y.; Zhao, H.; Zhu, L.; Wang, Y.; Xu, W.; Zhen, Y.; Wang, X.; Dong, H.; Zhu, D.; Hu, W., 1D Mixed-Stack Cocrystals Based on Perylene Diimide toward Ambipolar Charge Transport. *Small* **2021,** *n/a* (n/a), 2006574.

49. Vermeulen, D.; Zhu, L. Y.; Goetz, K. P.; Hu, P.; Jiang, H.; Day, C. S.; Jurchescu, O. D.; Coropceanu, V.; Kloc, C.; McNeil, L. E., Charge Transport Properties of Perylene–TCNQ Crystals: The Effect of Stoichiometry. *The Journal of Physical Chemistry C* **2014,** *118* (42), 24688-24696.

50. McHale, J. L., Hierarchal Light-Harvesting Aggregates and Their Potential for Solar Energy Applications. *The Journal of Physical Chemistry Letters* **2012,** *3* (5), 587-597.

51. Kasha, M.; Rawls, H. R.; El-Bayoumi, M. A., Exciton model in molecular spectroscopy. *Pure Appl. Chem.* **1965,** *11* (3-4), 371-92.

52. Khazraji, A. C.; Hotchandani, S.; Das, S.; Kamat, P. V., Controlling Dye (Merocyanine-540) Aggregation on Nanostructured TiO2 Films. An Organized Assembly Approach for Enhancing the Efficiency of Photosensitization. *The Journal of Physical Chemistry B* **1999,** *103* (22), 4693-4700.

53. Mulhern, K. R.; Detty, M. R.; Watson, D. F., Aggregation-Induced Increase of the Quantum Yield of Electron Injection from Chalcogenorhodamine Dyes to TiO2. *The Journal of Physical Chemistry C* **2011,** *115* (13), 6010-6018.

54. Chang, D. W.; Ko, S.-J.; Kim, J. Y.; Park, S.-M.; Lee, H. J.; Dai, L.; Baek, J.-B., Multifunctional Conjugated Polymers with Main-Chain Donors and Side-Chain Acceptors for Dye Sensitized Solar Cells (DSSCs) and Organic Photovoltaic Cells (OPVs). *Macromolecular Rapid Communications* **2011,** *32* (22), 1809-1814.

55. Azumi, T.; Armstrong, A. T.; McGlynn, S. P., Energy of Excimer Luminescence. II. Configuration Interaction between Molecular Exciton States and Charge Resonance States. *J. Chem. Phys.* **1964,** *41* (12), 3839-3852.

56. Birks, J. B.; Lumb, M. D.; Munro, I. H.; Flowers Brian, H., 'Excimer' fluorescence V. Influence of solvent viscosity and temperature. *Proceedings of the Royal Society of London. Series A. Mathematical and Physical Sciences* **1964,** *280* (1381), 289-297.

57. Chandross, E. A.; Ferguson, J., Mixed Excimer Fluorescence; The Importance of Charge-Transfer Interaction. *The Journal of Chemical Physics* **1967,** *47* (8), 2557-2560.

58. Chandross, E. A.; Ferguson, J., Absorption and Excimer Fluorescence Spectra of Sandwich Dimers of Substituted Anthracenes. *The Journal of Chemical Physics* **1966,** *45* (10), 3554-3564.

59. Mauck, C. M.; Hartnett, P. E.; Margulies, E. A.; Ma, L.; Miller, C. E.; Schatz, G. C.; Marks, T. J.; Wasielewski, M. R., Singlet Fission via an Excimer-Like Intermediate in 3,6-Bis(thiophen-2-yl)diketopyrrolopyrrole Derivatives. *Journal of the American Chemical Society* **2016,** *138* (36), 11749-11761.

60. Walker, B. J.; Musser, A. J.; Beljonne, D.; Friend, R. H., Singlet exciton fission in solution. *Nature Chemistry* **2013,** *5*, 1019.

61. Eaton, S. W.; Miller, S. A.; Margulies, E. A.; Shoer, L. E.; Schaller, R. D.; Wasielewski, M. R., Singlet Exciton Fission in Thin Films of tert-Butyl-Substituted Terrylenes. *The Journal of Physical Chemistry A* **2015,** *119* (18), 4151-4161.

62. Miller, C. E.; Wasielewski, M. R.; Schatz, G. C., Modeling Singlet Fission in Rylene and Diketopyrrolopyrrole Derivatives: The Role of the Charge Transfer State in Superexchange and Excimer Formation. *The Journal of Physical Chemistry C* **2017,** *121* (19), 10345-10350.

63. Bullock, J. E.; Vagnini, M. T.; Ramanan, C.; Co, D. T.; Wilson, T. M.; Dicke, J. W.; Marks, T. J.; Wasielewski, M. R., Photophysics and Redox Properties of Rylene Imide and Diimide Dyes Alkylated Ortho to the Imide Groups. *The Journal of Physical Chemistry B* **2010,** *114* (5), 1794-1802.

64. Würthner, F.; Saha-Möller, C. R.; Fimmel, B.; Ogi, S.; Leowanawat, P.; Schmidt, D., Perylene Bisimide Dye Assemblies as Archetype Functional Supramolecular Materials. *Chemical Reviews* **2016,** *116* (3), 962-1052.

65. Chen, Z.; Stepanenko, V.; Dehm, V.; Prins, P.; Siebbeles, L. D. A.; Seibt, J.; Marquetand, P.; Engel, V.; Würthner, F., Photoluminescence and Conductivity of Self-Assembled π–π Stacks of Perylene Bisimide Dyes. *Chemistry – A European Journal 13* (2), 436-449.

66. Fink, R. F.; Seibt, J.; Engel, V.; Renz, M.; Kaupp, M.; Lochbrunner, S.; Zhao, H.-M.; Pfister, J.; Würthner, F.; Engels, B., Exciton Trapping in π-Conjugated Materials: A Quantum-Chemistry-Based Protocol Applied to Perylene Bisimide Dye Aggregates. *Journal of the American Chemical Society* **2008,** *130* (39), 12858-12859.

67. Würthner, F., Perylene bisimide dyes as versatile building blocks for functional supramolecular architectures. *Chemical Communications* **2004,** (14), 1564-1579.

68. Brennan, B. J.; Portolés, M. J. L.; Liddell, P. A.; Moore, T. A.; Moore, A. L.; Gust, D., Comparison of silatrane, phosphonic acid, and carboxylic acid functional groups for attachment of porphyrin sensitizers to TiO2 in photoelectrochemical cells. *Physical Chemistry Chemical Physics* **2013,** *15* (39), 16605-16614.

69. Ahrens, M. J.; Kelley, R. F.; Dance, Z. E. X.; Wasielewski, M. R., Photoinduced charge separation in self-assembled cofacial pentamers of zinc-5,10,15,20-tetrakis(perylenediimide)porphyrin. *Physical Chemistry Chemical Physics* **2007,** *9* (12), 1469-1478.

70. Wicklein, A.; Lang, A.; Muth, M.; Thelakkat, M., Swallow-Tail Substituted Liquid Crystalline Perylene Bisimides: Synthesis and Thermotropic Properties. *Journal of the American Chemical Society* **2009,** *131* (40), 14442-14453.

71. Szpakolski, K.; Latham, K.; Rix, C.; Rani, R. A.; Kalantar-zadeh, K., Silane: A new linker for chromophores in dye-sensitised solar cells. *Polyhedron* **2013,** *52*, 719-732.

72. Margulies, E. A.; Shoer, L. E.; Eaton, S. W.; Wasielewski, M. R., Excimer formation in cofacial and slip-stacked perylene-3,4:9,10-bis(dicarboximide) dimers on a redox-inactive triptycene scaffold. *Physical Chemistry Chemical Physics* **2014,** *16* (43), 23735-23742.

73. Giaimo, J. M.; Lockard, J. V.; Sinks, L. E.; Scott, A. M.; Wilson, T. M.; Wasielewski, M. R., Excited Singlet States of Covalently Bound, Cofacial Dimers and Trimers of Perylene-3,4:9,10-bis(dicarboximide)s. *The Journal of Physical Chemistry A* **2008,** *112* (11), 2322-2330.

74. Kronik, L.; Neaton, J. B., Excited-State Properties of Molecular Solids from First Principles. *Annual Review of Physical Chemistry* **2016,** *67* (1), 587-616.

75. Sharifzadeh, S.; Darancet, P.; Kronik, L.; Neaton, J. B., Low-Energy Charge-Transfer Excitons in Organic Solids from First-Principles: The Case of Pentacene. *The Journal of Physical Chemistry Letters* **2013,** *4* (13), 2197-2201.

76. Kircher, T.; Löhmannsröben, H. G., Photoinduced charge recombination reactions of a perylene dye in acetonitrile. *Physical Chemistry Chemical Physics* **1999,** *1* (17), 3987-3992.

77. Gosztola, D.; Niemczyk, M. P.; Svec, W.; Lukas, A. S.; Wasielewski, M. R., Excited Doublet States of Electrochemically Generated Aromatic Imide and Diimide Radical Anions. *J. Phys. Chem. A* **2000,** *104* (28), 6545-6551.

78. Wu, Y.; Young, R. M.; Frasconi, M.; Schneebeli, S. T.; Spenst, P.; Gardner, D. M.; Brown, K. E.; Würthner, F.; Stoddart, J. F.; Wasielewski, M. R., Ultrafast Photoinduced Symmetry-Breaking Charge Separation and Electron Sharing in Perylenediimide Molecular Triangles. *Journal of the American Chemical Society* **2015,** *137* (41), 13236-13239.

79. Würthner, F.; Sautter, A.; Schmid, D.; Weber, P. J. A., Fluorescent and Electroactive Cyclic Assemblies from Perylene Tetracarboxylic Acid Bisimide Ligands and Metal Phosphane Triflates. *Chemistry – A European Journal* **2001,** *7* (4), 894-902.

80. Pensack, R. D.; Ashmore, R. J.; Paoletta, A. L.; Scholes, G. D., The Nature of Excimer Formation in Crystalline Pyrene Nanoparticles. *The Journal of Physical Chemistry C* **2018,** *122* (36), 21004-21017.

81. Poinern, G. E. J.; Ali, N.; Fawcett, D., Progress in Nano-Engineered Anodic Aluminum Oxide Membrane Development. *Materials* **2011,** *4* (3), 487-526.

82. Materna, K. L.; Jiang, J.; Crabtree, R. H.; Brudvig, G. W., Silatrane Anchors for Metal Oxide Surfaces: Optimization for Potential Photocatalytic and Electrocatalytic Applications. *ACS Applied Materials & Interfaces* **2018**.

83. Tran, H.; Gopinadhan, M.; Majewski, P. W.; Shade, R.; Steffes, V.; Osuji, C. O.; Campos, L. M., Monoliths of Semiconducting Block Copolymers by Magnetic Alignment. *ACS Nano* **2013,** *7* (6), 5514-5521.

84. Young, R. M.; Dyar, S. M.; Barnes, J. C.; Juríček, M.; Stoddart, J. F.; Co, D. T.; Wasielewski, M. R., Ultrafast Conformational Dynamics of Electron Transfer in ExBox4+⊂Perylene. *The Journal of Physical Chemistry A* **2013,** *117* (47), 12438-12448.

85. Eaton, S. W.; Shoer, L. E.; Karlen, S. D.; Dyar, S. M.; Margulies, E. A.; Veldkamp, B. S.; Ramanan, C.; Hartzler, D. A.; Savikhin, S.; Marks, T. J.; Wasielewski, M. R., Singlet Exciton Fission in Polycrystalline Thin Films of a Slip-Stacked Perylenediimide. *Journal of the American Chemical Society* **2013,** *135* (39), 14701-14712.

86. MATLAB, MATLAB. **2018,** *The Mathworks, Inc., Natick, Massachusetts, United States*.

87. Lewis, N. S.; Nocera, D. G., Powering the planet: Chemical challenges in solar energy utilization. *Proceedings of the National Academy of Sciences of the United States of America* **2006,** *103*, 15729-15735.

88. Olaya-Castro, A.; Scholes, G. D., Energy transfer from Förster–Dexter theory to quantum coherent light-harvesting. *International Reviews in Physical Chemistry* **2011,** *30* (1), 49-77.

89. Clegg, R. M., Fluorescence resonance energy transfer. *Current Opinion in Biotechnology* **1995,** *6* (1), 103-110.

90. van Grondelle, R.; Novoderezhkin, V. I., Energy Transfer in photosynthesis: experimental insights and quantitative models. *Phys. Chem. Chem. Phys.* **2006,** *8*, 793-087.

91. Scholes, G. D.; Ghiggino, K. P., Electronic Interactions and Interchromophore Excitation Transfer. *The Journal of Physical Chemistry* **1994,** *98* (17), 4580-4590.

92. Young, R. M.; Wasielewski, M. R., Mixed Electronic States in Molecular Dimers: Connecting Singlet Fission, Excimer Formation, and Symmetry-Breaking Charge Transfer. *Acc. Chem. Res.* **2020,** *53* (9), 1957-1968.

93. Aster, A.; Licari, G.; Zinna, F.; Brun, E.; Kumpulainen, T.; Tajkhorshid, E.; Lacour, J.; Vauthey, E., Tuning symmetry breaking charge separation in perylene bichromophores by conformational control. *Chem. Sci.* **2019,** *10* (45), 10629-10639.

94. Dover, C. B.; Gallaher, J. K.; Frazer, L.; Tapping, P. C.; Petty, A. J.; Crossley, M. J.; Anthony, J. E.; Kee, T. W.; Schmidt, T. W., Endothermic singlet fission is hindered by excimer formation. *Nature Chemistry* **2018,** *10* (3), 305-310.

95. Vedernikov, A. I.; Lobova, N. A.; Kuz'mina, L. G.; Fomina, M. V.; Strelenko, Y. A.; Howard, J. A. K.; Gromov, S. P., Self-assembly of cucurbiturils and cyclodextrins to supramolecular millstones with naphthalene derivatives capable of translocations in the host cavities. *New Journal of Chemistry* **2019,** *43* (9), 3673-3689.

96. Bae, Y. J.; Shimizu, D.; Schultz, J. D.; Kang, G.; Zhou, J.; Schatz, G. C.; Osuka, A.; Wasielewski, M. R., Balancing Charge Transfer and Frenkel Exciton Coupling Leads to Excimer

Formation in Molecular Dimers: Implications for Singlet Fission. *J. Phys. Chem. A* **2020,** *124* (41), 8478-8487.

97. Samanta, S.; Ray, S. K.; Deolka, S.; Saha, S.; K. R, P.; Bhowal, R.; Ghosh, N.; Chaudhuri, D., Safeguarding long-lived excitons from excimer traps in H-aggregated dye-assemblies. *Chemical Science* **2020,** *11* (22), 5710-5715.

98. Birks, J. B.; Kazzaz, A. A.; King, T. A.; Flowers, B. H., 'Excimer' fluorescence - IX. Lifetime studies of pyrene crystals. *Proceedings of the Royal Society of London. Series A. Mathematical and Physical Sciences* **1966,** *291* (1427), 556-569.

99. Duan, L.; Qiao, J.; Sun, Y.; Zhang, D.; Dong, G.; Wang, L.; Qiu, Y., Ambipolar Transporting 1,2-Benzanthracene Derivative with Efficient Green Excimer Emission for Single-Layer Organic Light-Emitting Diodes. *Advanced Optical Materials* **2013,** *1* (2), 167-172.

100. Kim, T.-I.; Jin, H.; Bae, J.; Kim, Y., Excimer Emission-Based Fluorescent Probe Targeting Caspase-3. *Analytical Chemistry* **2017,** *89* (19), 10565-10569.

101. Seyfang, R.; Port, H.; Fischer, P.; Wolf, H. C., Picosecond study on excimer formation in pyrene crystals: Part III: Complete analysis of the high temperature phase between 5 and 300 K. *Journal of Luminescence* **1992,** *51* (4), 197-208.

102. Mauck, C. M.; Young, R. M.; Wasielewski, M. R., Characterization of Excimer Relaxation via Femtosecond Shortwave- and Mid-Infrared Spectroscopy. *J. Phys. Chem. A* **2017,** *121* (4), 784-792.

103. Lim, J. M.; Kim, P.; Yoon, M.-C.; Sung, J.; Dehm, V.; Chen, Z.; Würthner, F.; Kim, D., Exciton delocalization and dynamics in helical π-stacks of self-assembled perylene bisimides. *Chemical Science* **2012,** *4* (1), 388-397.

104. Takahashi, Y.; Kitamura, T.; Uchida, K.; Tomura, M., Migration of excimers in pyrene crystals. *Journal of Luminescence* **1981,** *22* (3), 267-271.

105. Tomura, M.; Takahashi, Y., Migration of excimer energy in pyrene crystal. *J. Phys. Soc. Jap.* **1971,** *31* (3), 797-801.

106. Lebovitz, Z.; Mansour, S.; Weinreb, A., Exciton migration and energy transfer in crystalline pyrene. *The Journal of Chemical Physics* **1978,** *69* (2), 647-660.

107. Petelenz, P.; Pac, B., Is Dipole Moment a Valid Descriptor of Excited State's Charge-Transfer Character? *Journal of the American Chemical Society* **2013,** *135* (46), 17379-17386.

108. Van Schenck, J. D. B.; Mayonado, G.; Anthony, J. E.; Graham, M. W.; Ostroverkhova, O., Molecular packing-dependent exciton dynamics in functionalized anthradithiophene derivatives: From solutions to crystals. *The Journal of Chemical Physics* **2020,** *153* (16), 164715.

109. Hestand, N. J.; Spano, F. C., Determining the spatial coherence of excitons from the photoluminescence spectrum in charge-transfer J-aggregates. *Chemical Physics* **2016,** *481*, 262-271.

110. Förster, T., Excimers. *Angewandte Chemie International Edition in English* **1969,** *8* (5), 333-343.

111. Bae, Y. J.; Kang, G.; Malliakas, C. D.; Nelson, J. N.; Zhou, J.; Young, R. M.; Wu, Y.-L.; Van Duyne, R. P.; Schatz, G. C.; Wasielewski, M. R., Singlet Fission in 9,10-Bis(phenylethynyl)anthracene Thin Films. *J. Am. Chem. Soc.* **2018,** *140* (45), 15140-15144.

112. Myong, M. S.; Zhou, J.; Young, R. M.; Wasielewski, M. R., Charge-transfer character in excimers of perylenediimides self-assembled on anodic aluminum oxide membrane walls. *J. Phys. Chem. C* **2020,** *124* (8), 4369-4377.

113. Chandrabose, S.; Chen, K.; Barker, A. J.; Sutton, J. J.; Prasad, S. K. K.; Zhu, J.; Zhou, J.; Gordon, K. C.; Xie, Z.; Zhan, X.; Hodgkiss, J. M., High Exciton Diffusion Coefficients in Fused Ring Electron Acceptor Films. *Journal of the American Chemical Society* **2019,** *141* (17), 6922-6929.

114. Sagara, Y.; Simon, Y. C.; Tamaoki, N.; Weder, C., A mechano- and thermoresponsive luminescent cyclophane. *Chemical Communications* **2016,** *52* (33), 5694-5697.

115. Walker, B.; Port, H.; Wolf, H. C., The two-step excimer formation in perylene crystals. *Chemical Physics* **1985,** *92* (2), 177-185.

116. Margulies, E. A.; Shoer, L. E.; Eaton, S. W.; Wasielewski, M. R., Excimer formation in cofacial and slip-stacked perylene-3,4:9,10-bis(dicarboximide) dimers on a redox-inactive triptycene scaffold. *Phys. Chem. Chem. Phys.* **2014,** *16* (43), 23735-23742.

117. Hudson, R. J.; Huang, D. M.; Kee, T. W., Anisotropic Triplet Exciton Diffusion in Crystalline Functionalized Pentacene. *The Journal of Physical Chemistry C* **2020,** *124* (43), 23541-23550.

118. Markovitsi, D.; Lecuyer, I.; Simon, J., One-dimensional triplet energy migration in columnar liquid crystals of octasubstituted phthalocyanines. *J. Phys. Chem.* **1991,** *95* (9), 3620-6.

119. Flanders, N. C.; Kirschner, M. S.; Kim, P.; Fauvell, T. J.; Evans, A. M.; Helweh, W.; Spencer, A. P.; Schaller, R. D.; Dichtel, W. R.; Chen, L. X., Large Exciton Diffusion Coefficients in Two Dimensional Covalent Or-ganic Frameworks with Different Domain Sizes Revealed by Ultrafast Exciton Dynamics. *Journal of the American Chemical Society* **2020**.

120. Sajjad, M. T.; Zhang, Y.; Geraghty, P. B.; Mitchell, V. D.; Ruseckas, A.; Blaszczyk, O.; Jones, D. J.; Samuel, I. D. W., Tailoring exciton diffusion and domain size in photovoltaic small molecules by annealing. *Journal of Materials Chemistry C* **2019,** *7* (26), 7922-7928.

121. Anikovsky, M.; Dale, L.; Ferguson, S.; Petersen, N., Resonance Energy Transfer in Cells: A New Look at Fixation Effect and Receptor Aggregation on Cell Membrane. *Biophysical Journal* **2008,** *95* (3), 1349-1359.

122. Cohen, M. D.; Haberkorn, R.; Huler, E.; Ludmer, Z.; Michel-Beyerle, M. E.; Rabinovich, D.; Sharon, R.; Warshel, A.; Yakhot, V., Pair-states in α-perylene crystal. A theoretical study. *Chem. Phys.* **1978,** *27* (2), 211-16.

123. Cohen, M. D.; Yakhot, V., The absorption and fluorescence properties of pyrene crystal: a theoretical approach. II. relaxation processes. *Chemical Physics* **1974,** *5* (1), 27-33.

124. Feng, K.; Peng, M.-L.; Wang, D.-H.; Zhang, L.-P.; Tung, C.-H.; Wu, L.-Z., Silica - and polymer -supported platinum(II) polypyridyl complexes: synthesis and application in photosensitized oxidation of alkenes. *Dalton Transactions* **2009,** *0* (44), 9794-9799.

125. Firdaus, Y.; Le Corre, V. M.; Karuthedath, S.; Liu, W.; Markina, A.; Huang, W.; Chattopadhyay, S.; Nahid, M. M.; Nugraha, M. I.; Lin, Y.; Seitkhan, A.; Basu, A.; Zhang, W.; McCulloch, I.; Ade, H.; Labram, J.; Laquai, F.; Andrienko, D.; Koster, L. J. A.; Anthopoulos, T. D., Long-range exciton diffusion in molecular non-fullerene acceptors. *Nature Communications* **2020,** *11* (1), 5220.

126. Zhu, W.; Zhu, L.; Zou, Y.; Wu, Y.; Zhen, Y.; Dong, H.; Fu, H.; Wei, Z.; Shi, Q.; Hu, W., Deepening Insights of Charge Transfer and Photophysics in a Novel Donor–Acceptor Cocrystal for Waveguide Couplers and Photonic Logic Computation. *Adv. Mater.* **2016,** *28* (28), 5954-5962.

127. Wykes, M.; Park, S. K.; Bhattacharyya, S.; Varghese, S.; Kwon, J. E.; Whang, D. R.; Cho, I.; Wannemacher, R.; Luer, L.; Park, S. Y.; Gierschner, J., Excited State Features and Dynamics in a Distyrylbenzene-Based Mixed Stack Donor-Acceptor Cocrystal with Luminescent Charge Transfer Characteristics. *J. Phys. Chem. Lett.* **2015,** *6* (18), 3682-3687.

128. Kumar, M.; Venkata Rao, K.; George, S. J., Supramolecular charge transfer nanostructures. *Physical Chemistry Chemical Physics* **2014,** *16* (4), 1300-1313.

129. Chiang, C. L.; Tseng, S. M.; Chen, C. T.; Hsu, C. P.; Shu, C. F., Influence of Molecular Dipoles on the Photoluminescence and Electroluminescence of Dipolar Spirobifluorenes. *Advanced Functional Materials* **2008,** *18* (2), 248-257.

130. Wang, H.; Li, F.; Gao, B.; Xie, Z.; Liu, S.; Wang, C.; Hu, D.; Shen, F.; Xu, Y.; Shang, H.; Chen, Q.; Ma, Y.; Sun, H., Doped Organic Crystals with High Efficiency, Color-Tunable Emission toward Laser Application. *Crystal Growth & Design* **2009,** *9* (11), 4945-4950.

131. Zang, L.; Che, Y.; Moore, J. S., One-Dimensional Self-Assembly of Planar π-Conjugated Molecules: Adaptable Building Blocks for Organic Nanodevices. *Accounts of Chemical Research* **2008,** *41* (12), 1596-1608.

132. Ning, Z.; Chen, Z.; Zhang, Q.; Yan, Y.; Qian, S.; Cao, Y.; Tian, H., Aggregation-induced Emission (AIE)-active Starburst Triarylamine Fluorophores as Potential Non-doped Red Emitters

for Organic Light-emitting Diodes and Cl2 Gas Chemodosimeter. *Advanced Functional Materials* **2007,** *17* (18), 3799-3807.

133. Friend, R. H.; Gymer, R. W.; Holmes, A. B.; Burroughes, J. H.; Marks, R. N.; Taliani, C.; Bradley, D. D. C.; Santos, D. A. D.; Brédas, J. L.; Lögdlund, M.; Salaneck, W. R., Electroluminescence in conjugated polymers. *Nature* **1999,** *397* (6715), 121-128.

134. Lee, J. H.; Yuan, Y. Y.; Kang, Y. J.; Jia, W. L.; Lu, Z. H.; Wang, S. N., 2,5-Functionalized Spiro-Bisiloles as Highly Efficient Yellow-Light Emitters in Electroluminescent Devices. *Advanced Functional Materials* **2006,** *16* (5), 681-686.

135. Tremblay, N. J.; Gorodetsky, A. A.; Cox, M. P.; Schiros, T.; Kim, B.; Steiner, R.; Bullard, Z.; Sattler, A.; So, W.-Y.; Itoh, Y.; Toney, M. F.; Ogasawara, H.; Ramirez, A. P.; Kymissis, I.; Steigerwald, M. L.; Nuckolls, C., Photovoltaic Universal Joints: Ball-and-Socket Interfaces in Molecular Photovoltaic Cells. *ChemPhysChem* **2010,** *11* (4), 799-803.

136. Kang, S. J.; Ahn, S.; Kim, J. B.; Schenck, C.; Hiszpanski, A. M.; Oh, S.; Schiros, T.; Loo, Y.-L.; Nuckolls, C., Using Self-Organization To Control Morphology in Molecular Photovoltaics. *Journal of the American Chemical Society* **2013,** *135* (6), 2207-2212.

137. Park, S. K.; Varghese, S.; Kim, J. H.; Yoon, S. J.; Kwon, O. K.; An, B. K.; Gierschner, J.; Park, S. Y., Tailor-Made Highly Luminescent and Ambipolar Transporting Organic Mixed Stacked Charge-Transfer Crystals: An Isometric Donor-Acceptor Approach. *J. Am. Chem. Soc.* **2013,** *135* (12), 4757-4764.

138. Sun, Y. Q.; Lei, Y. L.; Sun, X. H.; Lee, S. T.; Liao, L. S., Charge-Transfer Emission of Mixed Organic Cocrystal Microtubes over the Whole Composition Range. *Chem. Mater.* **2015,** *27* (4), 1157-1163.

139. Wang, C.; Wang, J.; Wu, N.; Xu, M.; Yang, X.; Lu, Y.; Zang, L., Donor–acceptor single cocrystal of coronene and perylene diimide: molecular self-assembly and charge-transfer photoluminescence. *RSC Advances* **2017,** *7* (4), 2382-2387.

140. Zhu, W. G.; Zhu, L. Y.; Zou, Y.; Wu, Y. S.; Zhen, Y. G.; Dong, H. L.; Fu, H. B.; Wei, Z. X.; Shi, Q.; Hu, W. P., Deepening Insights of Charge Transfer and Photophysics in a Novel Donor-Acceptor Cocrystal for Waveguide Couplers and Photonic Logic Computation (vol 28, pg 5954, 2016). *Adv. Mater.* **2016,** *28* (35), 7563-7563.

141. Zhu, W. G.; Zheng, R. H.; Fu, X. L.; Fu, H. B.; Shi, Q.; Zhen, Y. G.; Dong, H. L.; Hu, W. P., Revealing the Charge-Transfer Interactions in Self-Assembled Organic Cocrystals: Two-Dimensional Photonic Applications. *Angew. Chem., Int. Ed.* **2015,** *54* (23), 6785-6789.

142. Geng, H.; Zheng, X. Y.; Shuai, Z. G.; Zhu, L. Y.; Yi, Y. P., Understanding the Charge Transport and Polarities in Organic Donor-Acceptor Mixed-Stack Crystals: Molecular Insights from the Super-Exchange Couplings. *Adv. Mater.* **2015,** *27* (8), 1443-1449.

143. Wan, Y.; Guo, Z.; Zhu, T.; Yan, S.; Johnson, J.; Huang, L., Cooperative singlet and triplet exciton transport in tetracene crystals visualized by ultrafast microscopy. *Nat. Chem.* **2015,** *7* (10), 785-792.

144. Zhu, T.; Wan, Y.; Guo, Z.; Johnson, J.; Huang, L., Two Birds with One Stone: Tailoring Singlet Fission for Both Triplet Yield and Exciton Diffusion Length. *Adv. Mater.* **2016,** *28*, 7939-7947.

145. Folie, B. D.; Haber, J. B.; Refaely-Abramson, S.; Neaton, J. B.; Ginsberg, N. S., Long-Lived Correlated Triplet Pairs in a π-Stacked Crystalline Pentacene Derivative. *J. Am. Chem. Soc.* **2018,** *140* (6), 2326-2335.

146. Sun, D.; Deng, G.-H.; Xu, B.; Xu, E.; Li, X.; Wu, Y.; Qian, Y.; Zhong, Y.; Nuckolls, C.; Harutyunyan, A. R.; Dai, H.-L.; Chen, G.; Chen, H.; Rao, Y., Anisotropic Singlet Fission in Single Crystalline Hexacene. *iScience* **2019,** *19*, 1079-1089.

147. Dillon, R. J.; Bardeen, C. J., The Effects of Photochemical and Mechanical Damage on the Excited State Dynamics of Charge-Transfer Molecular Crystals Composed of Tetracyanobenzene and Aromatic Donor Molecules. *J. Phys. Chem. A* **2011,** *115* (9), 1627-1633.

148. Dillon, R. J.; Bardeen, C. J., Time-Resolved Studies of Charge Recombination in the Pyrene/TCNQ Charge-Transfer Crystal: Evidence for Tunneling. *J. Phys. Chem. A* **2012,** *116* (21), 5145-5150.

149. Sun, S.; Pang, J.; Ni, S.; Zhang, G.; Xu, L.; Dang, L.; Li, M.-D., Insight into Intermolecular Charge Transfer Determined by Two Packing Mode Cocrystals. *J. Phys. Chem. C* **2020,** *124*, 17744–17751.

150. Hartschuh, A.; Port, H.; Wolf, H. C., Polarized fs transient absorption of CT states in An-PMDA crystals-Excitonic strings? *J. Lumin.* **2001,** *94&95*, 441-445.

151. Port, H.; Hartschuh, A., Fs-dynamics of charge-transfer excited states in anthracene-PMDA single crystals. *J. Lumin.* **2004,** *110* (4), 315-324.

152. Schlesinger, I.; Powers-Riggs, N. E.; Logsdon, J. L.; Qi, Y.; Miller, S. A.; Tempelaar, R.; Young, R. M.; Wasielewski, M. R., Charge-transfer biexciton annihilation in a donor-acceptor co-crystal yields high-energy long-lived charge carriers. *Chem. Sci.* **2020,** *11* (35), 9532-9541.

153. Shida, T.; Iwata, S., Electronic spectra of ion radicals and their molecular orbital interpretation. III. Aromatic hydrocarbons. *J. Am. Chem. Soc.* **1973,** *95* (11), 3473-3483.

154. Borowicz, P.; Nickel, B., Application of high-accuracy time-resolved laser spectroscopy to the study of diffusion-controlled triplet-triplet annihilation. *Optoelectronics Review* **2004,** *12*, 22. 325-332.

155. Chen, J.; Li, S.; Gong, F.; Yang, Z.; Wang, S.; Xu, H.; Li, Y.; Ma, J. S.; Yang, G., Photophysics and Triplet−Triplet Annihilation Analysis for Axially Substituted Gallium

Phthalocyanine Doped in Solid Matrix. *The Journal of Physical Chemistry C* **2009,** *113* (27), 11943-11951.

156. Yost, S. R.; Hontz, E.; Yeganeh, S.; Van Voorhis, T., Triplet vs Singlet Energy Transfer in Organic Semiconductors: The Tortoise and the Hare. *The Journal of Physical Chemistry C* **2012,** *116* (33), 17369-17377.

157. Haarer, D.; Philpott, M. R.; Morawitz, H., Field induced charge-transfer exciton transitions. *The Journal of Chemical Physics* **1975,** *63* (12), 5238-5245.

158. Zhang, J.; Geng, H.; Virk, T. S.; Zhao, Y.; Tan, J.; Di, C.-a.; Xu, W.; Singh, K.; Hu, W.; Shuai, Z.; Liu, Y.; Zhu, D., Sulfur-Bridged Annulene-TCNQ Co-Crystal: A Self-Assembled ‘‘Molecular Level Heterojunction’’ with Air Stable Ambipolar Charge Transport Behavior. *Advanced Materials* **2012,** *24* (19), 2603-2607.

159. Qin, Y.; Cheng, C.; Geng, H.; Wang, C.; Hu, W.; Xu, W.; Shuai, Z.; Zhu, D., Efficient ambipolar transport properties in alternate stacking donor–acceptor complexes: from experiment to theory. *Physical Chemistry Chemical Physics* **2016,** *18* (20), 14094-14103.

160. Fonari, A.; Sutton, C.; Brédas, J.-L.; Coropceanu, V., Impact of exact exchange in the description of the electronic structure of organic charge-transfer molecular crystals. *Physical Review B* **2014,** *90* (16), 165205.

161. Wilson, T. M.; Tauber, M. J.; Wasielewski, M. R., Toward an n-Type Molecular Wire: Electron Hopping within Linearly Linked Perylenediimide Oligomers. *J. Am. Chem. Soc.* **2009,** *131* (25), 8952-8957.

162. Zhang, G.; Chen, X.-K.; Xiao, J.; Chow, P. C. Y.; Ren, M.; Kupgan, G.; Jiao, X.; Chan, C. C. S.; Du, X.; Xia, R.; Chen, Z.; Yuan, J.; Zhang, Y.; Zhang, S.; Liu, Y.; Zou, Y.; Yan, H.; Wong, K. S.; Coropceanu, V.; Li, N.; Brabec, C. J.; Bredas, J.-L.; Yip, H.-L.; Cao, Y., Delocalization of exciton and electron wavefunction in non-fullerene acceptor molecules enables efficient organic solar cells. *Nature Communications* **2020,** *11* (1), 3943.

163. Sheldrick, G. M., Crystal structure refinement with SHELXT. *Acta Crystallogr A Struct Chem* **2015,** *71* (Pt 1), 3-8.

164. Dolomanov, O. V.; Bourhis, L. J.; Gildea, R. J.; Howard, J. A. K.; Puschmann, H., OLEX2: a complete structure solution, refinement and analysis program. *J. Appl. Crystallogr.* **2009,** *42* (2), 339-341.

165. Sheldrick, G. M., A short history of SHELX. *Acta Crystallographica Section A* **2008,** *64*, 112-122.

166. Markovitsi, D.; Lecuyer, I.; Simon, J., One-dimensional triplet energy migration in columnar liquid crystals of octasubstituted phthalocyanines. *The Journal of Physical Chemistry* **1991,** *95* (9), 3620-3626.

167. Jimenez, R.; Dikshit, S. N.; Bradforth, S. E.; Fleming, G. R., Electronic Excitation Transfer in the LH2 Complex of Rhodobacter sphaeroides. *The Journal of Physical Chemistry* **1996,** *100* (16), 6825-6834.

168. Pullerits, T.; Chachisvilis, M.; Sundström, V., Exciton Delocalization Length in the B850 Antenna of Rhodobacter sphaeroides. *The Journal of Physical Chemistry* **1996,** *100* (25), 10787-10792.

169. Spano, F. C.; Clark, J.; Silva, C.; Friend, R. H., Determining exciton coherence from the photoluminescence spectral line shape in poly(3-hexylthiophene) thin films. *The Journal of Chemical Physics* **2009,** *130* (7), 074904.

170. Clark, J.; Silva, C.; Friend, R. H.; Spano, F. C., Role of Intermolecular Coupling in the Photophysics of Disordered Organic Semiconductors: Aggregate Emission in Regioregular Polythiophene. *Physical Review Letters* **2007,** *98* (20), 206406.

171. Spano, F. C., Modeling disorder in polymer aggregates: The optical spectroscopy of regioregular poly(3-hexylthiophene) thin films. *The Journal of Chemical Physics* **2005,** *122* (23), 234701.

172. Spano, F. C., Absorption in regio-regular poly(3-hexyl)thiophene thin films: Fermi resonances, interband coupling and disorder. *Chemical Physics* **2006,** *325* (1), 22-35.

173. Myong, M. S.; Zhou, J.; Young, R. M.; Wasielewski, M. R., Charge-Transfer Character in Excimers of Perylenediimides Self-Assembled on Anodic Aluminum Oxide Membrane Walls. *The Journal of Physical Chemistry C* **2020,** *124* (8), 4369-4377.

174. Ghosh, S.; Li, X.-Q.; Stepanenko, V.; Würthner, F., Control of H- and J-Type π Stacking by Peripheral Alkyl Chains and Self-Sorting Phenomena in Perylene Bisimide Homo- and Heteroaggregates. *Chemistry – A European Journal* **2008,** *14* (36), 11343-11357.

175. Chen, S.; Zhou, J.; Young, R. M.; Wasielewski, M. R., Excited-State Dynamics of Perylene-Based Chromophore Assemblies on Nanoporous Anodic Aluminum Oxide Membranes. *The Journal of Physical Chemistry C* **2021,** *125* (27), 14843-14853.

176. Yadav, P.; Srivastava, P. K.; Ghosh, S., Dielectric screening of excitons in monolayer graphene. *Nanoscale* **2015,** *7* (43), 18015-18019.

177. Spano, F. C.; Silva, C., H- and J-Aggregate Behavior in Polymeric Semiconductors. *Annual Review of Physical Chemistry* **2014,** *65* (1), 477-500.

178. Tempelaar, R.; Spano, F. C.; Knoester, J.; Jansen, T. L. C., Mapping the Evolution of Spatial Exciton Coherence through Time-Resolved Fluorescence. *The Journal of Physical Chemistry Letters* **2014,** *5* (9), 1505-1510.